2021

The synthesis and characterization of advanced functional properties of well-defined nanoscale building blocks

Patrick Campbell
camp7320@mylaurier.ca

The synthesis and characterization of advanced functional properties of well-defined nanoscale building blocks

by

Patrick Campbell

BSc, Wilfrid Laurier University, 2021

Thesis

Submitted to the Department of Chemistry and Biochemistry

in partial fulfilment of the requirements for

Master of Science in Chemistry

Wilfrid Laurier University

Table of Contents

List of abbreviations

NPs…Nanoparticles

SPR…Surface plasmon resonance

LSPR…Localized surface plasmon resonance

AgDeNPs…Silver decahedral nanoparticles

AgPRNPs…Silver pentagonal rod nanoparticles

SPRI…. Surface plasmon resonance imaging

Au@AgDeNPs...Gold plated silver decahedral nanoparticles

IrO_{2-x}…Iridium oxyhydroxide

γ-Fe_2O_3…Maghemite

α-Fe_2O_3…Hematite

β-FeOOH…Akageneite

PEC…Photoelectrochemical

IrO_{2-x}@AgDeNPs...Iridium oxyhydroxide encapsulated silver decahedral nanoparticles

DLS…Dynamic light scattering

PDI…Polydispersity index

AgNPs…Silver nanoparticles

PNP… Plasmonic nanoparticles

S…Reference to a hematite **seed** sample

R …Reference to a hematite **regrowth** sample

PVP… Polyvinylpyrrolidone

PSS… Poly(styrene-4-sulfonate)

PDDA…Polydiallyldimethylammonium chloride

CA… Reference to citric acid used in hematite NP synthesis

AA… Reference to aspartic acid used in hematite NP synthesis

OA… Reference to oxalic acid used in hematite NP synthesis

MH… Reference to a multi-step heating protocol

MH*… Reference to a modified multi-step heating protocol

Z-Avg… Average nanoparticle size obtained via dynamic light scattering

1.1 Introduction

Nanotechnology is the science and engineering conducted at dimensions of 1–100 nanometers, where unique phenomena enable novel applications.[1.1-1.6] In the last decade, engineered nanoparticles have become an important class of new materials with several properties that make them very attractive for commercial development.[1.1-1.6]

Silver decahedral nanoparticles (AgDeNPs)

Surface plasmon resonance (SPR) is one of the interesting and functionally important nanoscale properties of noble metal nanoparticles (NPs). SPR is a coherent oscillation of surface conduction electrons upon excitation by electromagnetic radiation at the interface between metal and dielectric media.[1.7] Localized surface plasmon resonance (LSPR) is when the SPR is restricted to smaller volumes, such as in nanoparticles, which are comparable or less in size to the wavelength of incident light.[1.7] Figure 1.1 demonstrates the collective oscillation of electrons excited by an electric field (E_o) associated with the light. At a certain excitation frequency, this oscillation will be in resonance with the incident light, creating a strong oscillation of surface electrons known as localized surface plasmon resonance.[1.8]

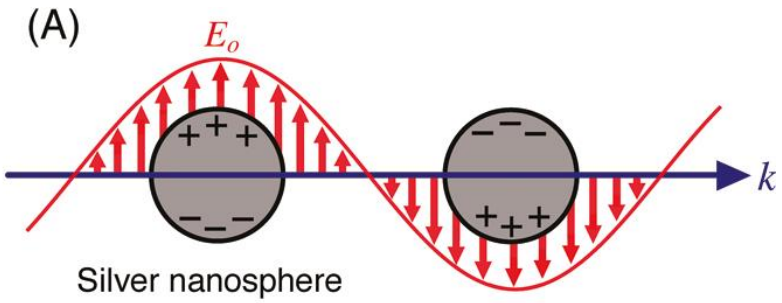

Figure 1.1. Schematic illustration of two silver nanospheres excited by the electric field (E_o) of incident light with wavevector (k). Localized surface plasmon resonance (LSPR) is the phenomenon that occurs if the nanostructure is smaller than the wavelength of incident light where, the free electrons can be displaced from the lattice of positive ions allowing the free electrons to collectively oscillate in resonance with the light.[1.8]

Metal NPs that exhibit LSPR are silver, gold, aluminum, copper, palladium and platinum. These specific metal NPs exhibit LSPR due to having the ideal electronic *d-sp* transition of an electron. Metal nanoparticles (NPs) have been extensively studied to utilize their plasmonic properties in research areas such as sensing, photocatalysis, electronics, and biomedicine.[1.7] Silver and gold NPs are the most important materials for LSPR applications due to their spectrum spanning the visible and near infrared regions.[1.8]

Iridium oxide core shells

Metal NPs can be enhanced either further when combined with a protective shell around its surface. The resulting structures are called core-shells. Core-shell structures can be defined as a combination of a core (inner material) and a shell (outer layer material).[1.9]

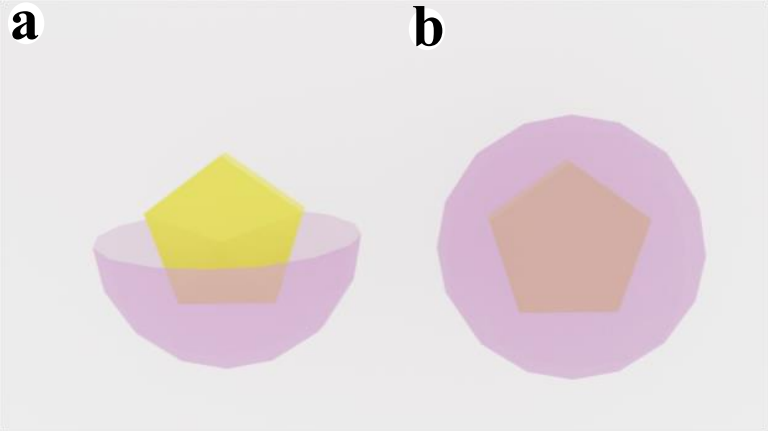

Figure 1.2. Schematic showing encapsulation of Au@AgDeNPs. a) Cross section of encapsulated Au@AgDeNPs. b) Fully encapsulated Au@AgDeNPs.

The combination of different inner and outer materials in the core-shell nanostructure imparts advantageous chemical and physical properties, allowing core-shells to be used in optics, biomedicine, energy conversion and storage.[1.9] The main advantages of core-shell structures are the following: 1) protecting the core from the effect of environmental changes and aggregating

into large particles; 2) enhancing or giving rise to new chemical or physical capabilities and 3) limiting volume expansion and maintain structural integrity.[1.9] Core-shell morphologies that have been reported include nanoparticles (NPs), spheres, nanowires, nanorods, nanotubes, nanobelts, nanofibers, nanoplates, nanosheets, cubes and flowers.[1.9]

Shape and design of hematite NPs

Iron oxides also have unique properties at the nanoscale useful for targeted applications. For example, iron oxides are a common choice for photoanode material mainly due to their semiconducting nature, chemical stability in aqueous solutions and low cost.[1.4] The natural forms of iron oxides are magnetite (Fe_3O_4), maghemite (γ-Fe_2O_3), hematite (α-Fe_2O_3), akageneite (β-FeOOH) and ε-Fe_2O_3.[1.10] Hematite is an inexpensive metal oxide with good stability, non-toxic and environmentally friendly.[1.10] Hematite NPs are used in diverse practical applications consisting of, biomedical[1.11, 1.12] catalysis[1.13], pseudocapacitors[1.14] environmental protection[1.15] and water splitting.[1.4,1.5,1.10]

Optical properties of hematite NPs

Hematite's functionality does not end with its photoelectrochemical capabilities. Hematite also has unique optical properties that have been utilized in pigment and paint applications. Since the 17th century Japan has been exporting colourful polychrome porcelain pottery to Europe captivating everyone with the artistic skill. Polychrome pottery is prepared as a paint from a lead-contained oxide powder and metal oxide colouring agent.[1.16] However these paints contain toxic lead, the lead release from the polychrome porcelain leads to health problems.[1.16] As such, development has progressed for a lead-free oxide glass powder or frit with high artisan quality to be incorporated in the process of akae production. "Akae" is a term used

for red overglaze enamels in porcelain creation.[1.16] These akae are used to decorate various styles of polychrome porcelain.[1.16] To create akae, pigments are required to establish the desired colours. For example, hematite nanoparticles have high thermal stability with respect to their colour. This is important for akae production due to difficulties in controlling red colours.[1.16] Current iron oxide pigments used in industry are synthetic Pigment Red 101 and the natural Pigment Red 102.[1.17, 1.18]

Summary

The synthesis of uniform high-quality silver decahedral[1.19] nanoparticles (AgDeNPs), silver pentagonal rod nanoparticles (AgPRNPs) and silver platelets is described in Chapter 2. In this chapter AgDeNPs were synthesized with LSPR peaks spanning 415 nm to 559 nm. The synthesis of AgDeNPs with a range of LSPR peaks is significant because it enables the tunability of plasmonic nanoparticles for specific applications.[1.20] For example, tunability of PNPs could be demonstrated by binding thiols to AgDeNP surface. These thiol-anchored affinity agents then could be tuned to target specific molecules. For example, Jia et al. describe an efficient method for aptamer screening using silver decahedra nanoparticles to enhance the surface plasmon resonance imaging (SPRI), providing real time evaluation of binding properties for the selected aptamer.[1.2]

The synthesis of uniform IrO_{2-x} core shells using AgDeNPs, Au@AgDeNPs and gold platelets as the core material is described in Chapter 3. These IrO_{2-x} core-shells self-assemble into uniform thin films. This IrO_{2-x} coating over the various core materials is significant because it can potentially improve their catalytic ability. This catalytic ability can be utilized in applications, such as catalyzing the hydrogen evolution reaction (HER) and oxygen evolution reaction (OER) processes, respectively, in acidic electrolytes.[1.3,1.21]

In Chapter 4 uniform 1-D and 3-D hematite NPs are investigated for photoelectrochemical and pigment applications. This project begins with 3-D hematite NPs transformed by seeded regrowth, into a 1-D spear like hematite morphology with controllable lengths. These hematite morphologies are important because their unique 1-D structure has promise as a photoelectrochemical cell (PEC) in water splitting applications. For example, hematite is one of the most promising photoanode materials for photoelectrochemical (PEC) water oxidation due to its favorable bandgap of 2.1 eV.[1.22,1.23, 1.24, 1.25]However the performance of the hematite photoanode for water oxidation is restricted by its poor electrical conductivity, poor charge separation and transfer efficiency.[1.23] These limitations can be solved with element doping, morphology engineering and surface modification.[1.23,1.26]

The synthesis of hematite thin films by using well-defined hematite NPs is discussed in Chapter 5. These hematite films display their natural red/orange colour as well as additional colours when observed via the transmission and reflection of light. These additional colours are the result of strong structural order of the hematite NPs in the film. The sizes of the hematite NPs that were synthesized range from 50 nm to 500 nm where the hematite films upon the interaction of light have a wavelength range from 465 nm to 650 nm. A unique reflective red film is obtained by the aggregation of smaller hematite NPs into larger hematite aggregates (see Figure 5.1 and Figure 5.2). Changing the morphology from 3-D to 1-D hematite growths creates a multi-coloured pigment film. These hematite thin films are important because they can be used in paint[1.18], as patterned colloidal photonic crystals[1.27], in ceramic, food, and construction industries[1.28].

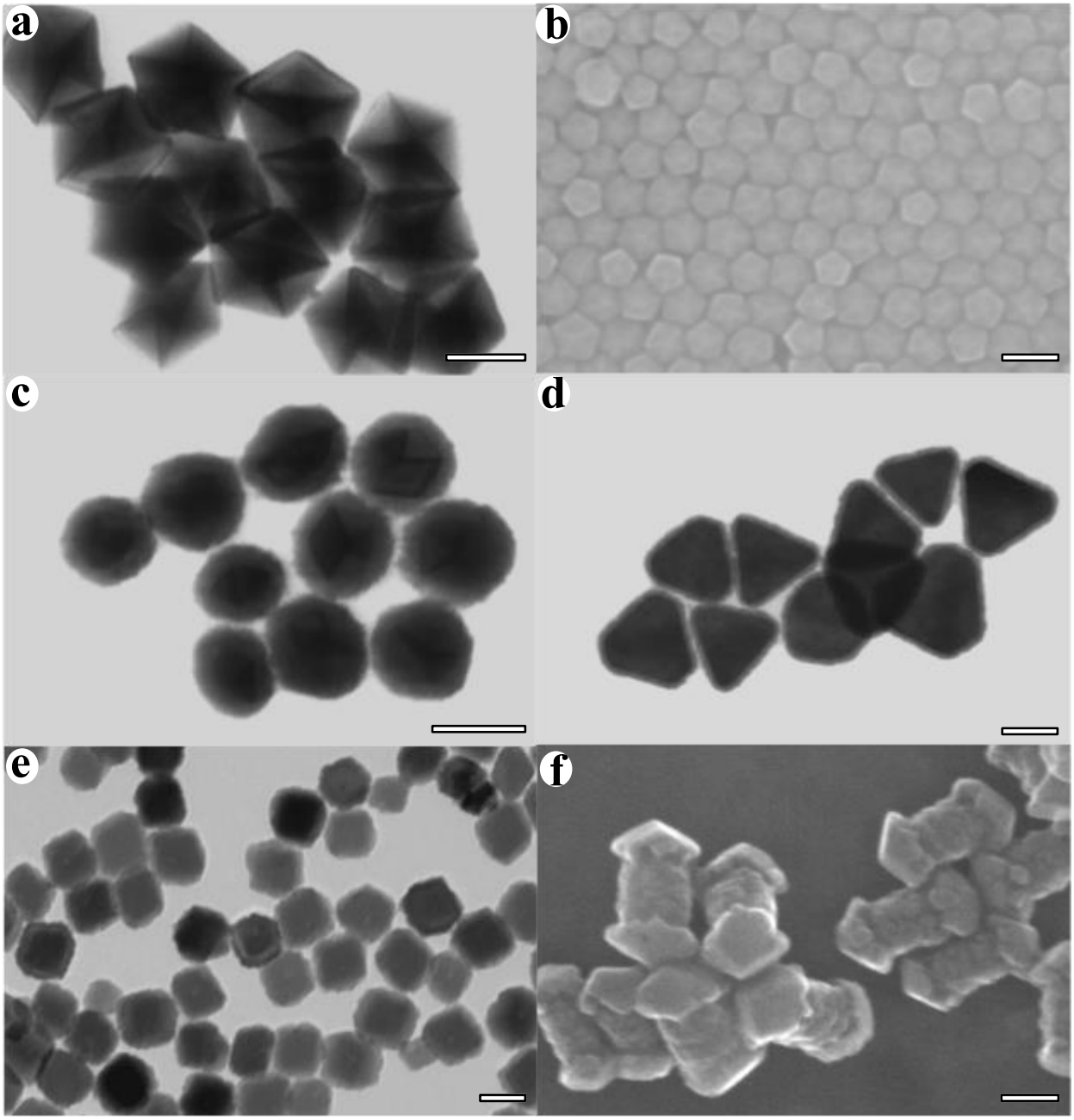

Figure 1.3. Electron microscopy (EM) images depicting AgNPs, IrO_{2-x} encapsulated NPs and hematite NPs. a) 2:1 R AgDeNPs. b) AgPRNPs. c) IrO_{2-x}@AgDeNPs. d) IrO_{2-x}@gold platelets. e) 2:1 R hematite rhombohedral NPs (1% H_2WO_4). f) Hematite 'spears' 2:1 R (400:1 citric acid (CA) :Fe). All scale bars are 50 nm. See Table 1.1 for more information.

Table 1.1: Summary of AgDeNPs, AgPRNPs, IrO_{2-x} core shells and hematite NPs developed/prepared/produced in MSc thesis work

Figure Name	Sample Name	Description	LSPR (nm)	EM Size (nm)	Z-avg (nm)	PDI
1.3a	PH 599	AgDeNPs regrown with 200% AgDeNP precursor on 505 nm LED	524	70 ± 2	N/A	N/A
1.3b	PE 632	AgPRNPs	716	Length 102 ± 3 Width 33 ± 1	N/A	N/A
1.3c	PF 386	300% IrO_{2-x} @AgDeNPs	530	N/A	N/A	N/A
1.3d	PF 227	200% IrO_{2-x} of gold platelets	910	N/A	N/A	N/A
1.3e	PH 575	2:1 R (1% H_2WO_4)	N/A	N/A	67± 2	0.082
1.3f	PE 820	2:1 R (1:400 CA:Fe) heated 9 days	N/A	N/A	91 ± 3	0.070

Therefore, this MSc research successfully accomplished the synthesis of uniform AgDeNPs, IrO_{2-x} core shells[1.29], 3-D hematite NPs, 1-D hematite NPs and subsequent creation of thin films of hematite NPs. These nanostructures were investigated for potential applications that included sensing[1.20], catalysis[1.21], water splitting[1.10] and construction of pigments[1.26]. This was accomplished by synthesizing uniform NPs of defined shape and structure and size. Control over these characteristics is crucial for the NPs at the nanoscale to function efficiently for their intended applications. Figure 1.3 shows a snapshot of the NPs discussed in this MSc thesis.

In Chapter 2 the synthesis of AgDeNPs of increasing sizes is demonstrated with LSPR peaks spanning from 415 nm to 559 nm. An example of AgDeNPs displaying a size of 70 ± 2 nm with a LSPR of 531 nm is displayed in Figure 1.3a. AgPRNPs are grown from AgDeNPs via thermal treatment and have self assembled into an array demonstrated in Figure 1.3b. When AgPRNPs self assemble, it is an indicator that the AgDeNPs used are of high quality.

The synthesis of uniform IrO_{2-x} core shells using AgDeNPs, Au@AgDeNPs and gold platelets as the core material are exhibited in Chapter 3. These IrO_{2-x} core-shells self-assemble into uniform thin films. Figure 1.3c illustrates an iridium oxide shell with silver decahedral NPs

as its core (IrO_{2-x}@AgDeNPs). These iridium oxide shells' thickness can be tuned based on the amount of $IrCl_3$ used, resulting in control over the size of the shell. The control over the IrO_{2-x} shell results in uniform IrO_{2-x}@AgDeNPs, leading to the formation of uniform arrays. Figure 1.3d displays iridium oxide coatings of gold platelets, demonstrating the versatility of this coating being applied on different morphologies.

Chapter 4 discusses the synthesis of 3-D and 1-D hematite NPs and how the 3-D hematite NPs are used as starting seeds to create the 1-D hematite NPs of controllable lengths. An example of the 3-D rhombohedral hematite NPs is displayed in Figure 1.3e. These rhombohedral hematite NPs are the starting morphology for the development of 1-D hematite NPs of various lengths and large 3-D hematite NPs used for preparation of thin films (see Chapter 5). Figure 1.3f illustrates a new 1-D hematite morphology named "spears". These 1-D hematite structures grow along the C_3 axis of the rhombohedral hematite NP. The ends of the 1-D hematite structure are caps with a corner slice of the rhombohedral hematite NP. The length of these 1-D hematite structures can be controlled based on the number of additives used in synthesis.

Chapter 5 discuss the synthesis of hematite thin films by using the well-defined hematite NPs discussed in Chapter 4. These hematite films display a full spectrum of structural colours when observed via the transmission and reflection of light.

1.2 References

[1.1]Medina, C.; Santos-Martinez, M. J.; Radomski, a; Corrigan, O. I.; Radomski, M. W. *Br. J. Pharmacol.* **2009**, *150*, 552–558.

[1.2]Jia, W.; Li, H.; Wilkop, T.; Liu, X.; Yu, X.; Cheng, Q.; Xu, D.; Chen, H. Y. *Biosens. Bioelectron.* **2018**, *109*, 206–213.

[1.3]Alia, S. M.; Rasimick, B.; Ngo, C.; Neyerlin, K. C.; Kocha, S. S.; Pylypenko, S.; Xu, H.; Pivovar, B. S. *J. Electrochem. Soc.* **2016**, *163*, F3105–F3112.

[1.4]Gurudayal; Bassi, P. S.; Sritharan, T.; Wong, L. H. *J. Phys. D. Appl. Phys.* **2018**, *51*, 1-28.

[1.5]Tee, S. Y.; Win, K. Y.; Teo, W. S.; Koh, L. D.; Liu, S.; Teng, C. P.; Han, M. Y. *Adv. Sci.* **2017**, *4*, 1-24.

[1.6]Carneiro, J.; Tobaldi, D. M.; Hajjaji, W.; Capela, M. N.; Novais, R. M.; Seabra, M. P.; Labrincha, J. A. *Ceram. Int.* **2018**, *44*, 4211–4219.

[1.7]Kang, H.; Buchman, J. T.; Rodriguez, R. S.; Ring, H. L.; He, J.; Bantz, K. C.; Haynes, C. L. *Chem. Rev.* **2019**, *119*, 664–699.

[1.8]Rycenga, M.; Cobley, C. M.; Zeng, J.; Li, W.; Moran, C. H.; Zhang, Q.; Qin, D.; Xia, Y. *Chem. Rev.* **2011**, *111*, 3669–3712.

[1.9]Lu, W.; Guo, X.; Luo, Y.; Li, Q.; Zhu, R.; Pang, H. *Chem. Eng. J.* **2019**, *355*, 208–237.

[1.10]Trpkov, D.; Panjan, M.; Kopanja, L.; Tadić, M. *Appl. Surf. Sci.* **2018**, *457*, 427–438.

[1.11]El Sayed, A. M.; Mohamad, A. D. M. *J. Polym. Res.* **2018**, *25*, 175-189.

[1.12]Zákutná, D.; Falke, Y.; Dresen, D.; Prévost, S.; Bender, P.; Honecker, D.; Disch, S. *Nanoscale* **2019**, *11*, 7149–7156.

[1.13]Puthirath Balan, A.; Radhakrishnan, S.; Woellner, C. F.; Sinha, S. K.; Deng, L.; Reyes, C. D. L.; Rao, B. M.; Paulose, M.; Neupane, R.; Apte, A.; et al. *Nat. Nanotechnol.* **2018**, *13*, 602–609.

[1.14]Sun, S.; Zhai, T.; Liang, C.; Savilov, S. V.; Xia, H. *Nano Energy* **2018**, *45*, 390–397.

[1.15]Lei, C.; Sun, Y.; Tsang, D. C. W.; Lin, D. *Environ. Pollut.* **2018**, *232*, 10–30.

[1.16]Inada, H.; Okazaki, Y.; Yokoyama, T.; Takaishi, T.; Fujii, T.; Takada, J.; Asoh, H.; Hashimoto, H. *J. Am. Ceram. Soc.* **2018**, *101*, 4538–4548.

[1.17]Mariani, F. Q.; Borth, K. W.; Müller, M.; Dalpasquale, M.; Anaissi, F. J. *Dye. Pigment.* **2017**, *137*, 403–409.

[1.18]Fiuza, T. E. R.; Borges, J. F. M.; Cunha, J. B. M. da; Antunes, S. R. M.; Andrade, A. V. C. de; Antunes, A. C.; Souza, É. C. F. de. *Dye. Pigment.* **2018**, *148*, 319–328.

[1.19]Zhou, S.; Zhao, M.; Yang, T. H.; Xia, Y. *Mater. Today* **2019**, *22*, 108–131.

[1.20]Li, Q.; Wang, F.; Bai, Y.; Xu, L.; Yang, Y.; Yan, L.; Hu, S.; Zhang, B.; Dai, S.; Tan, Z. *Org. Electron.* **2017**, *43*, 33–40.

[1.21]Jin, H.; Joo, J.; Chaudhari, N. K.; Choi, S. Il; Lee, K. *ChemElectroChem* **2019**, *6*, 3244–3253.

[1.22]Li, C.; Luo, Z.; Wang, T.; Gong, J. *Adv. Mater.* **2018**, *30*, 1–23.

[1.23]Li, M.; Yang, Y.; Ling, Y.; Qiu, W.; Wang, F.; Liu, T.; Song, Y.; Liu, X.; Fang, P.; Tong, Y.; et al. *Nano Lett.* **2017**, *17*, 2490-2495.

[1.24]Jiang, C.; Moniz, S. J. A.; Wang, A.; Zhang, T.; Tang, J. *Chem. Soc. Rev.* **2017**, *46*, 4645-4660.

[1.25]Liu, G.; Zhao, Y.; Yao, R.; Li, N.; Wang, M.; Ren, H.; Li, J.; Zhao, C. *Chem. Eng. J.* **2019**, *355*, 49–57.

[1.26]Kment, S.; Riboni, F.; Pausova, S.; Wang, L.; Wang, L.; Han, H.; Hubicka, Z.; Krysa, J.; Schmuki, P.; Zboril, R. *Chem. Soc. Rev.* **2017**, *46*, 3716–3769.

[1.27]Hou, J.; Li, M.; Song, Y. *Angew. Chemie - Int. Ed.* **2018**, *57*, 2544–2553.

[1.28]Ryan, M. J.; Kney, A. D.; Carley, T. L. *Appl. Geochemistry* **2017**, *79*, 27–35.

[1.29]Cathcart, N.; Murshid, N.; Campbell, P.; Kitaev, V. *ACS Appl. Nano Mater.* **2018**, *1*, 6514–6524.

Chapter 2: Synthesis and characterization of silver decahedral nanoparticles (AgDeNPs)

2.1 Introduction

Nanotechnology is the use of matter on an atomic, molecular and supramolecular scale for industrial purposes.[2.1] In the field of nanotechnology, nanoparticles (NPs) exhibit special properties from bulk materials due to their size, shape and composition. The size range for NPs occurs from 1 nm to 100 nm. Nanomaterials that are less than 1 nm in size are considered clusters, exhibiting molecular behavior. Nanomaterials that are bigger than 100 nm in size are in the bulk region, displaying bulk characteristics. When the NP size is between ca. 5 nm and 100 nm unique optical, sensing and catalytic properties may be exhibited.

For example, in this size range plasmonic metal NPs (PNPs) exhibit a unique property called localized surface plasmon resonance (LSPR). LSPR can be defined as electromagnetic excitation of electron density. The resulting excitation energy is coupled to the free charges of a conductive medium[2.2] and is determined by the size of metal NPs, their shape, composition, and local dielectric environment.[1.8, 2.3] Metals like Pd, Pt, and Al have LSPR peaks that occur in the UV region but for the LSPR property to be used in practical applications silver, gold and copper metals are used, due to their LSPR peaks occurring in the visible and NIR regions.[2.1] This area of research is important due to numerous applications that include surface enhanced Raman spectroscopy (SERS),[2.4] plasmon-enhanced fluorescence,[2.5] light harvesting,[2.6] photocatalysis,[2.7, 2.8] as well as chemical and biological sensing.[2.9]

A variety of different NP morphologies have been synthesized which would include quasi-spherical,[2.10–2.12] rods,[2.13–2.17] triangles,[2.18] cubes,[2.19,2.20] stars,[2.21] and prisms.[2.22] Depending on the shape of the PNPs they can have multiple plasmonic resonances. For example, spherical

NPs have a single resonance, while anisotropic structures like silver pentagonal rod nanoparticles (AgPRNPs) display two plasmon resonances.[1.8, 2.23] The transverse peak is the resonance that occurs along the width of the AgPRNP. The longitudinal peak is the other resonance that occurs down the length of the AgPRNP.[1.8]

In this chapter the synthesis of high-quality uniform silver decahedral nanoparticles (AgDeNPs), silver pentagonal rods (AgPRNPs) and silver platelets is demonstrated. Uniform AgDeNPs with a specific size exhibit LSPR peaks at a certain wavelength. The ability to consistently produce uniform AgDeNPs of various sizes results in LSPR peaks that span the visible region. This is powerful for biological sensing applications because AgDeNPs can be tuned to display specific LSPR peaks. These LSPR peaks shift when a target molecule binds to AgDeNP surface, allowing for detection.

2.2 Experimental: AgDeNP synthesis protocol

Reagents

Silver nitrate (99.9%), hydrogen peroxide (30-32 wt% solution in water) (ca.10.4 M), L-arginine (TLC, 98%), sodium citrate tribasic dihydrate (99+%) and sodium borohydride (99%) were supplied by Aldrich and used as received. Poly(styrene-4-sulfonate), (PSS, M_w=70 K) was supplied by Aldrich but was purified via three dissolution and precipitation cycles with isopropanol, as a non-solvent. Polyvinylpyrrolidone (PVP) M_w=40 K) was supplied by Caledon. High-purity deionized water (>18.4 M Ω cm) was produced using Millipore A10 Milli-Q.

Procedure

Method 1 Synthesis of one-stage AgDeNPs with LSPR peaks in the range of 467-470 nm

To a 20 mL vial containing 14 mL of high–purity deionized water the following solutions were added in the listed order: 0.520 mL of 5.00 x 10^{-2} M sodium tricitrate, 0.023 mL of 5.00 x 10^{-2} M PSS, 0.025 mL of 5.00 x 10^{-3} M L-arginine, 0.400 mL of 5.00 x 10^{-3} M silver nitrate and freshly prepared 0.200 mL 0.1 M sodium borohydride. The content of the vial was stirred with a magnetic stir bar. After 30 minutes, a slight colour change from bright yellow to dark yellow is observed, where 0.300 mL hydrogen peroxide was added. Subsequently, the vial was then placed on a 449 nm LED for 14 hours. AgDeNPs were characterized via EM and UV-vis spectroscopy. Masses of all reagents were measured using an analytical balance. Concentrations of stock solutions created are expected to have an error of ca. 1.5%.

Method 2 Synthesis of precursor AgDeNP seeds

To a 20 mL vial containing 14 mL of high–purity deionized water the following solutions were added in the listed order: 0.520 mL of 5.00 x 10^{-2} M sodium tricitrate, 0.023 mL of 5.00 x 10^{-2} M PSS, 0.025 mL of 5.00 x 10^{-3} M L-arginine, 0.400 mL of 5.00 x 10^{-3} M silver nitrate and freshly prepared 0.200 mL 0.1 M sodium borohydride. The content of the vial was stirred with a magnetic stir bar. After 30 minutes, a slight colour change from bright yellow to dark yellow is observed. AgDeNPs were characterized via EM and UV-vis spectroscopy.

Method 3 Synthesis of AgDeNPs with LSPR peaks at 415 nm

To a 20 mL vial the following solutions were added in the listed order: 5.165 mL of AgDeNPs and 134 μL of 1.00 x 10^{-2} M KBr. 5.165 mL of AgDeNPs were added in 6 increments

of 860 μL. This solution was placed on a hot plate at 95°C for one hour. AgDeNPs were characterized via EM and UV-vis spectroscopy.

Method 4 Synthesis of AgDeNPs with LSPR peaks at 450 nm

To a 20 mL vial the following solutions were added in the listed order: 5.165 mL of AgDeNPs and 16 μL of 2.48 x 10^{-2} M KCl. 5.165 mL of AgDeNPs were added in 6 increments of 860 μL. This solution was placed on a hot plate at 95°C for one hour. AgDeNPs were characterized via EM and UV-vis spectroscopy.

Method 5 Synthesis of AgDeNP regrowth with LSPR peaks in the range of 485 - 495 nm

For the synthesis of AgDeNPs with LSPR peaks from 485 nm - 495nm, 5 mL of 470 nm AgDeNP seeds were added to a 20 mL vial. Then 6.25 mL of AgDeNP precursor was added to the 20 mL vial. 6.25 mL of AgDeNPs were added in 7 increments of 892 μL. The solution was mixed. The vial is placed on 474 nm light for 14 hours. See Table 2.1 for more details. AgDeNPs were characterized via EM and UV-vis spectroscopy.

Method 6 Synthesis of AgDeNP regrowth with LSPR peaks in the range of 495 - 525 nm

For the synthesis of AgDeNPs with LSPR peaks from 495 nm - 525 nm, 5 mL of 495 nm AgDeNP seeds were added to a 20 mL vial. Then 10 mL of AgDeNP precursor was added to the 20 mL vial. 10 mL of AgDeNPs were added in 11 increments of 909 μL. The vial is placed on 505 nm light for 14 hours. See Table 2.1 for more details. AgDeNPs were characterized via EM and UV-vis spectroscopy.

Method 7 Synthesis of AgDeNP regrowth with LSPR peaks in the range of 530 - 565 nm

For the synthesis of AgDeNPs with LSPR peaks from 530 nm - 565 nm, 3 mL of 514 nm AgDeNP seeds were added to a 20 mL vial. Then 1.350 mL of AgDeNP precursor was added to the 20 mL vial. 1.350 mL of AgDeNPs were added in 2 increments of 675 μL. The vial is placed on 505 nm light for 14 hours. See Table 2.1 for more details. AgDeNPs were characterized via EM and UV-vis spectroscopy.

Method 8 Synthesis of silver platelets with LSPR peaks in the range of 565 - 590 nm

For the synthesis of silver platelets with LSPR peaks from 565 nm - 590 nm, 1 mL of 555 nm AgDeNP seeds were added to a 20 mL vial. Then 4 mL of AgDeNP precursor was added to the 20 mL vial. 4 mL of AgDeNPs were added in 5 increments of 800 μL. The vial is placed on 525 nm light for 14 hours. See Table 2.1 for more details Silver platelets were characterized via EM and UV-vis spectroscopy.

Table 2.1: Summary of AgDeNP regrowths: LSPR peak, reagents and exposure time.

Growth (nm)	Method #	Sample LSPR (nm)	AgDeNP Seed (mL)	Decahedra Precursor (mL)	Time (hours)	LED Used (nm)
485 - 495	Method 5	496	5	6.25	14	474
495 - 525	Method 6	514	5	10	14	505
530 - 565	Method 7	557	3	1.35	14	505
565 - 590	Method 8	584	1	4	14	525

Instrumentation

UV-vis spectra were recorded using an Ocean Optics QE65000 fiber-optic UV-vis spectrometer. Electron microscopy (EM) imaging was performed with a Hitachi S-5200 using a copper grid with a formvar/carbon film (FCF-200 Electron Microscopy Science). AgDeNPs were centrifuged using a Thermo scientific Legend Micro 21 centrifuge and Medifuge centrifuge.

2.3 Results and discussion

The LSPR peaks of AgDeNPs in the range of 415 nm to 559 nm are displayed in Figure 2.1. The inset in Figure 2.1 shows the colour change of the AgDeNPs as their NP size increases. Sample **1** and Sample **2** were synthesized using method 3 and method 4. Sample **1** and Sample **2** are rounded AgDeNPs with 415 nm and 450 nm LSPR peaks. The AgDeNPs are rounded by using KBr and KCl. As the AgDeNPs are rounded their size decreases (see Figure 2.2). The reduction in NP size for AgDeNPs leads to their LSPR peaks blue shift since LSPR is dependent on size. AgDeNPs with LSPR peaks in the range of 460 nm to 470 nm are used as precursors for AgDeNP rounding and seeded regrowth. Sample **3** is an example of AgDeNP starting seeds using method 1 and method 2. Sample **4** to Sample **6** were synthesized with method 5 to method 7 respectively. Sample **4** to Sample **6** are AgDeNPs that have been regrown using AgDeNPs with LSPR peaks in the range of 467 nm to 470 nm (Sample **3**). When these AgDeNPs are regrown the resulting LSPR is redshifted in comparison to the initial LSPR of AgDeNPs. These LSPR peaks range from 494 nm to 559 nm. For instance, to synthesize AgDeNPs with a LSPR in the range of 485 nm to 495 nm a portion of AgDeNPs with a LSPR peak of 467 nm (Sample **3**) is added to undeveloped AgDeNP precursor. This sample is then exposed to 470 nm LED light, promoting the growth of larger AgDeNPs. This seeded regrowth can be consecutively performed until an excitation

wavelength of ca. 505 nm is reached (see Figure 2.3). If method 8 is performed where AgDeNPs are grown at an excitation wavelength greater than 505 nm the morphology changes from AgDeNPs to silver platelets (Sample **7**), which is shown in Figure 2.4. Therefore, by using LEDs with a wavelength greater than 500 nm[2.13] the excited AgDeNP seeds are dissolved, leaving only silver platelets. Thus, Figure 2.1 shows AgDeNPs of various sizes that were synthesized with a LSPR peaks in a range from 415 nm to 559 nm. Figure 2.2 and Figure 2.3 displays EM images of AgDeNPs, showing their size increase together with their size distribution.

AgDeNP formation process

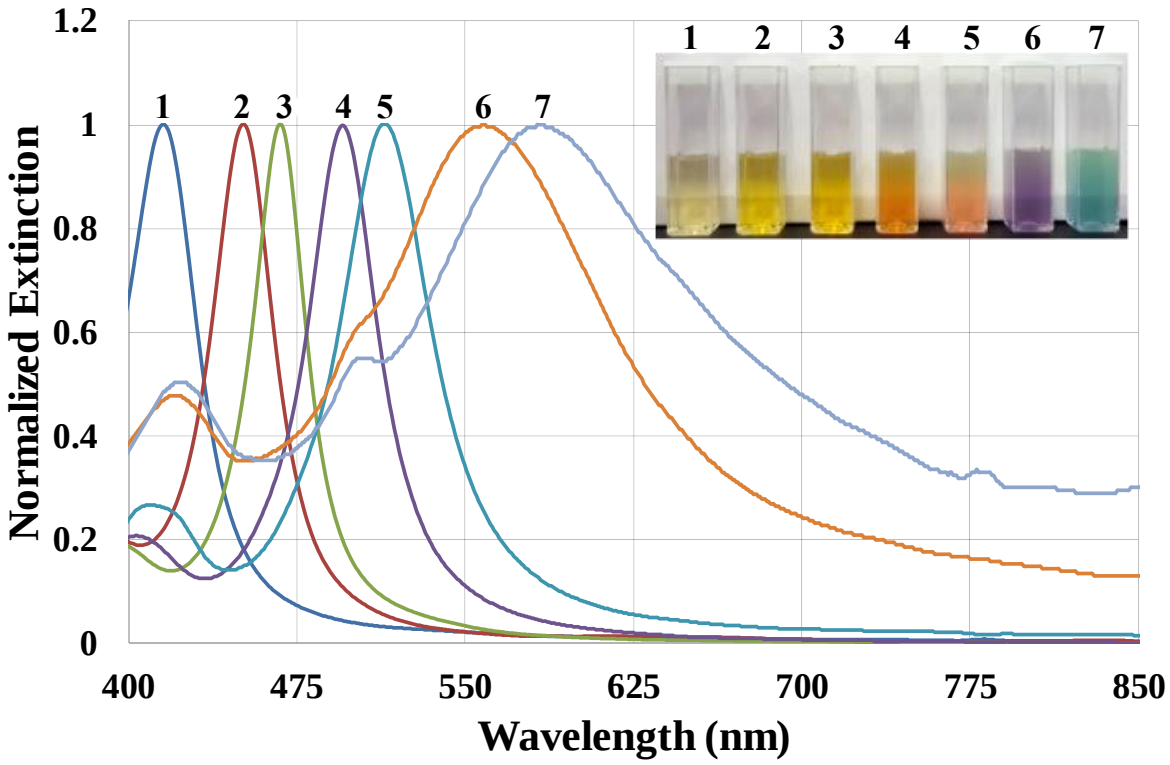

Figure 2.1. Normalized UV-vis spectra of AgDeNPs and silver platelets of increasing wavelength. 1) AgDeNPs rounded with KBr, LSPR peak of 415 nm (Method 3). 2) AgDeNPs rounded with KCl, LSPR peak of 450 nm (Method 4). 3) AgDeNPs grown on 449 nm LEDs, LSPR peak of 467 nm (Method 1 and Method 2). 4) AgDeNPs regrown with 165% of 0.005 M $AgNO_3$ on 470 nm LEDs, LSPR peak of 494 nm (Method 5). 5) AgDeNPs regrown with 200% AgDeNP precursor on 505 nm LEDs, LSPR peak of 513 nm (Method 6). 6) AgDeNPs regrown with 125% AgDeNP precursor on 505 nm LEDs, LSPR peak of 559 nm (Method 7). 7) Silver platelets, regrown with 400% AgDeNP precursor on 527 nm LEDs, LSPR peak of 585 nm (Method 8). Inset contains optical photograph of color variation of increasing AgDeNP size. See Table 2.2 for more information.

Table 2.2: Summary of AgDeNP: sample description, LSPR peaks and size from EM imaging.

Figure Number	Sample Name	Description	LSPR (nm)	EM size (nm)
Fig. 2.1(1)	PH 197	AgDeNPs (rounded with KBr).	415	N/A
Fig. 2.1(2)	PB 592	AgDeNPs (rounded with KCl).	450	N/A
Fig. 2.1(3)	PH 237	AgDeNPs (grown on 449 nm LEDs).	467	N/A
Fig. 2.1(4)	PB 667	AgDeNPs (regrown with 165% $AgNO_3$ on 470 nm LEDs).	494	56 ± 2
Fig. 2.1(5)	PH 242	AgDeNPs (regrown with 200% AgDeNP precursor on 505 nm LEDs).	513	N/A
Fig. 2.1(6)	PH 264	AgDeNPs (regrown with 125% AgDeNP precursor on 505 nm LEDs).	559	N/A
Fig. 2.1(7)	PH 266	Silver platelets (regrown with 400% AgDeNP precursor on 527 nm LEDs).	585	73 ± 2
Fig. 2.2a	PH 124	AgDeNPs rounded with KBr	425	35 ± 1
Fig. 2.2b	PB 722A	AgDeNPs rounded with KCl	450	36 ± 1
Fig. 2.3a	PE 452	AgDeNPs exposed to 449 nm LED's	470	36 ± 1
Fig. 2.3b	PB 667	AgDeNPs regrown with 165% of 0.005 M $AgNO_3$ on 470 nm LED	494	56 ± 2
Fig. 2.3c	PH 599	AgDeNPs regrown with 200% AgDeNP precursor on 505 nm LED	524	70 ± 2
Fig. 2.3d	PH 811	AgDeNPs regrown with 50% AgDeNP precursor on 505 nm LED	538	N/A

Fig. 2.4a	PH 266	Silver platelets regrown with 400% AgDeNP precursor on 527 nm LED	585	73 ± 2
Fig. 2.5a	PE 632	AgPRNPs	716	Length 102 ±3 Width 33 ± 1
Fig. 2.6(1)	PC 145	AgPRNPs (4.5:1 Ag $AgNO_3$:sample Ag)	555	N/A
Fig. 2.6(2)	PC 146	AgPRNPs (5.5:1 Ag $AgNO_3$:sample Ag).	590	N/A
Fig. 2.6(3)	PC 147	AgPRNPs (6:1 Ag $AgNO_3$:sample Ag.	630	N/A

The knowledge gap that this chapter addresses is the ability to produce a range of uniform AgDeNPs in size and shape. Uniform AgDeNPs with a specific size and shape exhibit LSPR peaks at a certain wavelength. The ability to consistently produce uniform AgDeNPs of various sizes results in multiple LSPR peaks that span the visible region. This is powerful for biological sensing applications because AgDeNPs can be tuned to display a certain LSPR peak when a target molecule binds to its surface, allowing for detection.

Figure 2.2 shows rounded AgDeNPs when KBr and KCl are added to AgDeNPs and heated. Figure 2.2a and Figure 2.2b show the rounding effect on edges of the decahedral structure, manipulating the shape, giving LSPR peaks in the range of 425 nm to 450 nm.

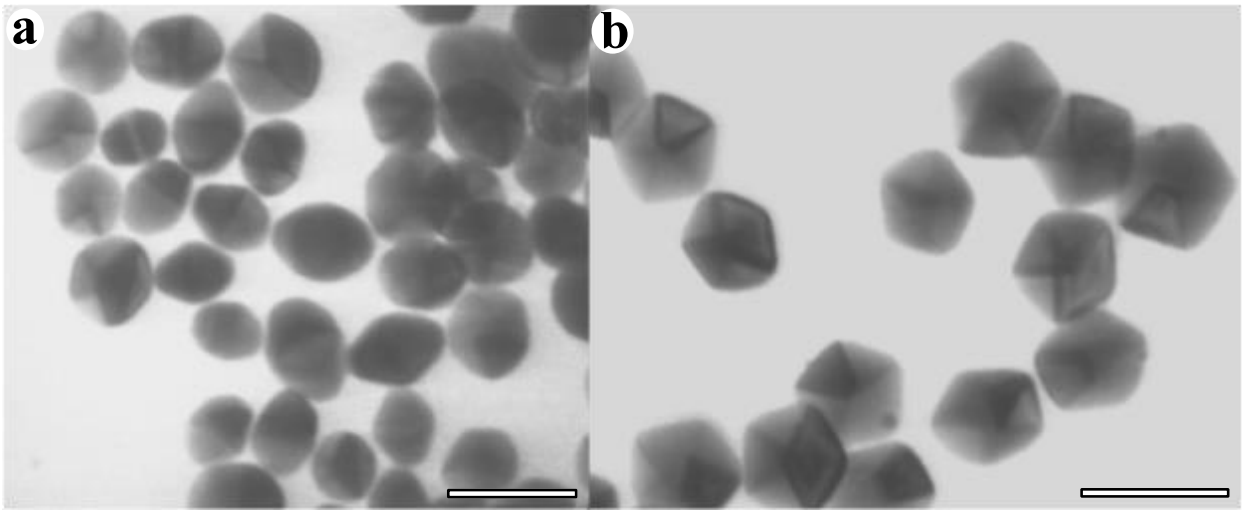

Figure 2.2. EM images of rounded AgDeNPs. a) AgDeNPs rounded with KBr, LSPR peak of 425 nm (Method 3). b) AgDeNPs rounded with KCl, LSPR peak of 450 nm (Method 4). All scale bars are 50 nm. See Table 2.2 for more information.

Figure 2.3 exhibits AgDeNP regrowths synthesized from AgDeNP seeds that have a LSPR peak of 467 nm. Figure 2.3a displays the AgDeNP seeds used to synthesize the AgDeNPs illustrated in Figure 2.3b, when exposed to 470 nm LED light. The AgDeNP seeds are used as a starting point in combination with $AgNO_3$, AgDeNP precursor and LED light to regrow the AgDeNPs larger, yielding LSPR peaks in the range of 494 nm to 538 nm, as shown in Figure 2.3b to Figure 2.3d. The AgDeNP seeds that have a LSPR peak of 494 nm are exposed to 505 nm LED light yielding the AgDeNPs with a LSPR peak of 524 nm, exhibited in Figure 2.3c. The AgDeNP seeds from Figure 2.3c are exposed to 505 nm LED light leading to AgDeNPs illustrated in Figure 2.3d. Exposing AgDeNP seeds to 527 nm LED light changes the LSPR selection resulting in formation of silver platelets (Figure 2.4).

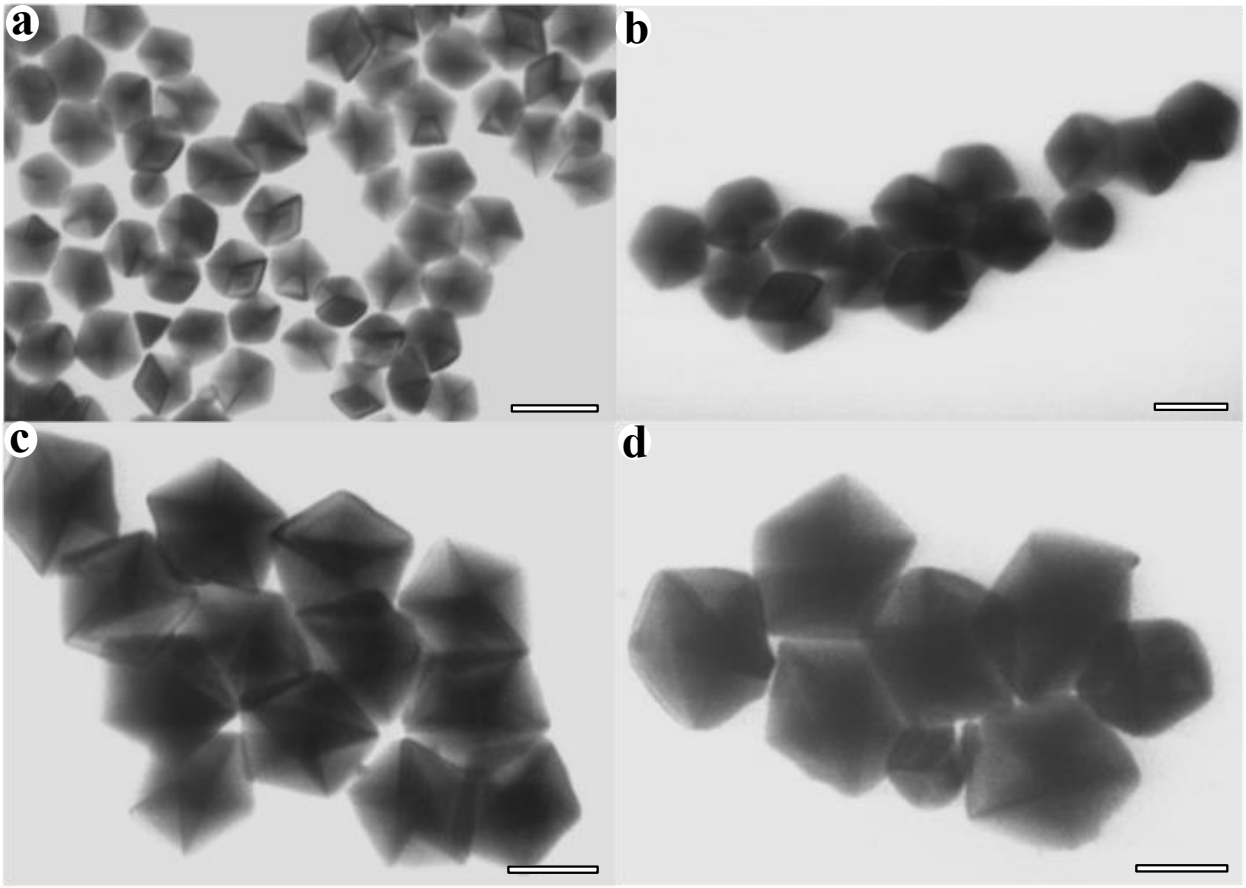

Figure 2.3. EM images of standard AgDeNPs and AgDeNP regrowths. a) AgDeNPs exposed to 449 nm LEDs, LSPR peak of 470 nm. b) AgDeNPs regrown with 165% of 0.005 M $AgNO_3$ on 470 nm LEDs, LSPR peak of 494 nm. c) AgDeNPs regrown with 200% AgDeNP precursor on 505 nm LEDs, LSPR peak of 524 nm. d) AgDeNPs regrown with 50% AgDeNP precursor on 505 nm LEDs, LSPR peak of 538 nm. All scale bars are 50 nm. See Table 2.2 for more information.

Figure 2.4a shows silver platelets synthesized by seeded regrowth using AgDeNP seeds with a LSPR peak of 538 nm, exposed to LED light with the wavelength of 527 nm. This change in NP morphology occurs because at an excitation wavelength above 500 nm the AgNP seeds are dissolved and only silver platelets are formed.[2.13] Therefore, Figure 2.4 and Figure 2.5 show that AgPRNPs and silver platelets were synthesized, offering different morphologies with variable LSPR peaks for biological sensing applications.

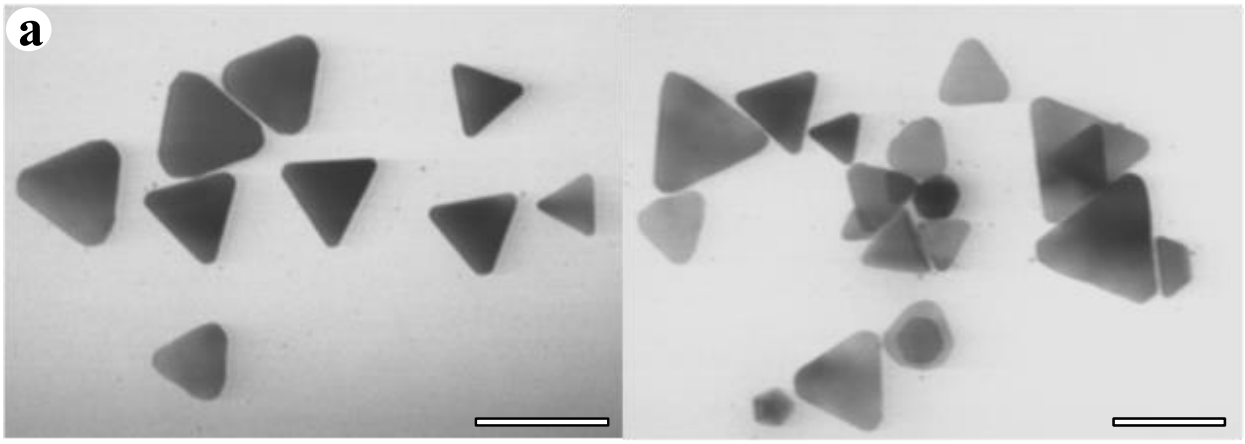

Figure 2.4. EM images of silver platelets. a) Silver platelets with 400% AgDeNP precursor on 527 nm LEDs, LSPR peak of 585 nm. All scale bars are 100 nm. See Table 2.2 for more information.

To test the quality of AgDeNPs, AgPRNPs were synthesized. When the AgDeNP quality is sufficiently high, the silver rods will form with good size dispersity and can self-assemble into hexagonal lattices (see Figure 2.5). AgPRNPs are formed by thermally transforming AgDeNPs though the growth initiated at the pentagonal twinned defect. This growth process results in five new (100) side facets while retaining ten original (111) capping facets of the decahedral seeds.[2.13] By the nature of their elongated morphology, AgPRNPs feature two distinct LSPR modes, transverse mode (short axis) and longitudinal (along the long axis).[1.8] These LSPR modes are displayed in Figure 2.6, where the transverse mode for Sample **1** has a LSPR peak at 410 nm. Sample **1** has a longitudinal LSPR peak at 555 nm. As the AgPRNPs increase in length, the longitudinal LSPR peak redshifts. As a result, Sample **2** and Sample **3** have longitudinal LSPR peaks of 590 nm and 630 nm respectively.

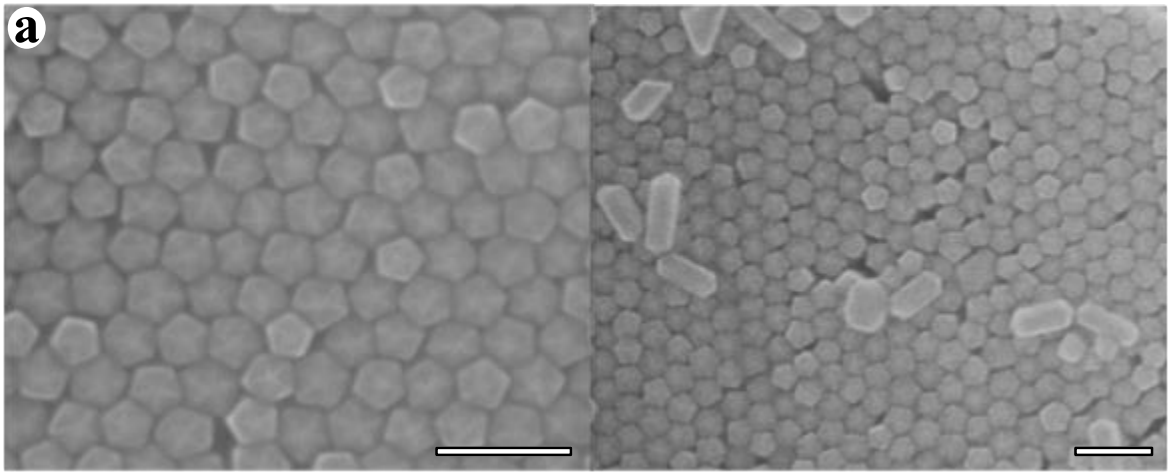

Figure 2.5. EM images of the silver pentagonal rod nanoparticles (AgPRNPs). a) Length 102 ± 3 nm and width 33 ± 1 nm, LSPR peak of 716 nm. All scale bars are 100 nm. See Table 2.2 for more information.

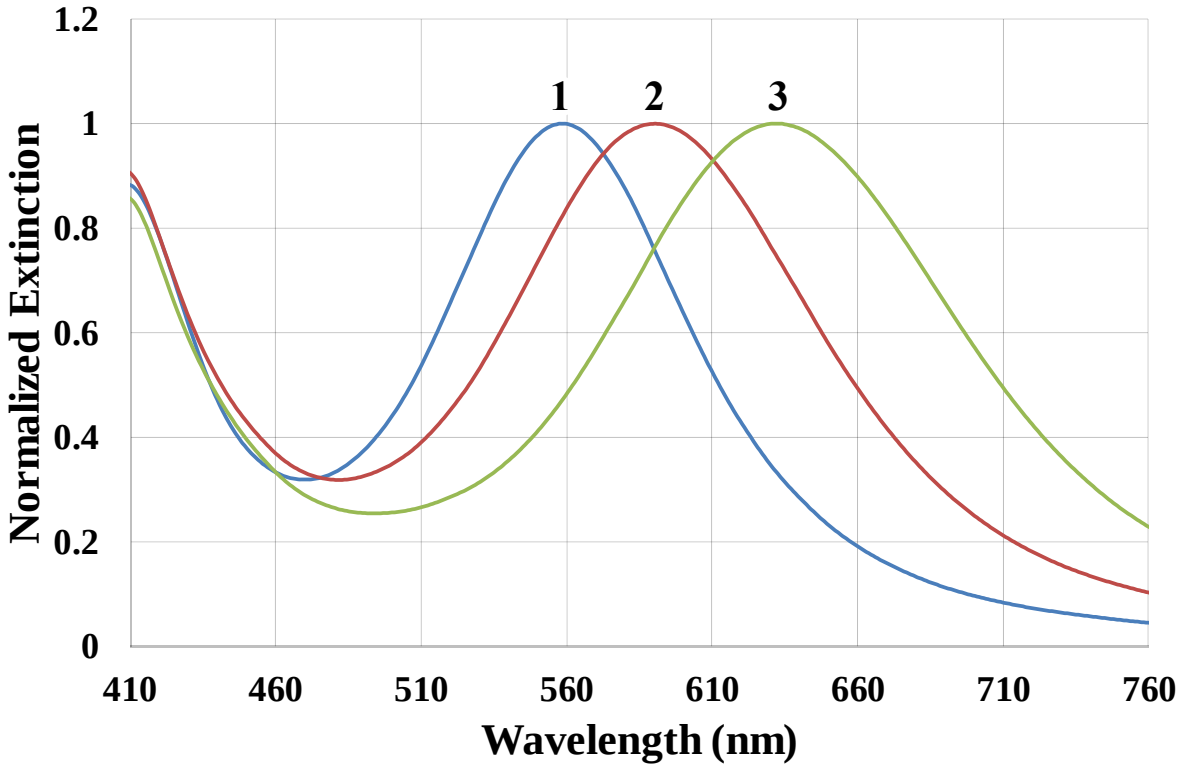

Figure 2.6. Normalized UV-vis spectra of AgPRNPs. 1) AgPRNPs with LSPR peak of 555 nm, 4.5:1 Ag addition relative Ag in seeds. 2) AgPRNPs with LSPR peak of 590 nm, 5.5:1 Ag addition to relative Ag in seeds. 3) AgPRNPs with LSPR peak of 630 nm, 6:1 Ag addition to Ag in seeds. See Table 2.2 for more information.

2.4 Conclusion

In summary, AgDeNPs were synthesized with LSPR peaks in the range of 415 nm to 559 nm and NPs sizes of 35 nm to 70 nm. This range of diverse LSPR peaks shows that the size, shape and dispersity of the AgDeNPs can be highly controlled. Other AgNPs that were synthesized are silver platelets and AgPRNPs. AgPRNPs were synthesized into self-assembled arrays and a range of LSPR responses in the range of 555 nm to 630 nm. These high quality AgDeNPs are important for specific biological sensing and catalytic applications. Chapter 3 discusses the encapsulation of these AgDeNPs with $IrCl_3$ creating a core shell structure that could be utilized in catalytic applications.

2.5 References

[2.1]Langer, J.; Novikov, S. M.; Liz-Marzán, L. M. *Nanotechnology* **2015,** *26,* 322001.

[2.2]Moskovits, M. *Near-field optics and surface plasmon polaritons*; S. Kawata ed.; Springer: Berlin, **2001**.

[2.3]Klinkova, A.; Choueiri, R. M.; Kumacheva, E. *Chem. Soc. Rev.* **2014,** *43,* 3976-3991.

[2.4]Moskovits, M. *J. Raman Spectrosc*. **2005,** *36,* 485–496.

[2.5]Lakowicz, J. R.; Ray, K.; Chowdhury, M.; Szmacinski, H.; Fu, Y.; Zhang, J.; Nowaczyk, K. *Analyst* **2008,** *133,* 1308–1346.

[2.6]Pillai, S.; Catchpole, K. R.; Trupke, T.; Green, M. A. *J. Appl. Phys*. **2007,** *101,* 093105.

[2.7]Hou,W.; Cronin, S. B. *Adv. Funct. Mater*. **2013,** *23,* 1612–1619.

[2.8]Jin, R. *Nanoscale* **2010,** *2,* 343−362.

[2.9]Stewart, M. E.; Anderton, C. R.; Thompson, L. B.; Maria, J.; Gray, S. K.; Rogers, J. A.; Nuzzo, R. G. *Chem. Rev*. **2008,** *108,* 494–521.

[2.10]Jana, N. R.; Gearheart, L.; Murphy, C. J. *Langmuir* **2001,** *17,* 6782–6786.

[2.11]Turkevich, J.; Stevenson, P. C.; Hillier, J. Discuss. *Faraday Soc*. **1951,** *11,* 55–75.

[2.12]Brust, M.; Walker, M.; Bethell, D.; Schiffrin, D. J.; Whyman, R. *J. Chem. Soc., Chem. Commun*. **1994,** *7,* 801–802.

[2.13]Murshid, N.; Keogh, D.; Kitaev, V. *Particle & Particle Systems Characterization* **2014,** *31,* 178–189.

[2.14]Nikoobakht, B.; El-Sayed, M. A. *Chem. Mater*. **2003,** *15,* 1957–1962.

[2.15]Jana, N. R.; Gearheart, L.; Murphy, C. J. *J. Phys. Chem. B,* **2001,** *105,* 4065–4067.

[2.16]Xiong, Y.; Cai, H.; Wiley, B. J.; Wang, J.; Kim, M. J. Xia, Y. *J. Am. Chem. Soc*. **2007,** *129,* 3665–3675.

[2.17]Pietrobon, B.; McEachran, M.; Kitaev, V. *ACS Nano* **2009,** *3,* 21–26.

[2.18]Sun, Y.; Mayers, B.; Xia, Y. *Nano Lett*. **2003,** *3,* 675–679.

[2.19]Sun , Y.; Xia, Y. *Science* **2002,** *298,* 2176–2179.

[2.20]Ahmadi, T. S.; Wang, Z. L.; Green, T. C.; Henglein, A.; El-Sayed, M. A. *Science* **1996,** *272,* 1924–1926.

[2.21]Nehl, C. L.; Liao, H.; Hafner, J. H. *Nano Lett*. **2006,** *6,* 683–688.

[2.22]Jin, R.; Cao, Y.; Mirkin, C. A.; Kelly, K. L.; Schatz, G. C.; Zheng, J. G. *Science* **2001,** *294,* 1901–1903.

[2.23]Chen, H.; Shao, L.; Li, Q.; Wang, J. *Chem. Soc. Rev*. **2013,** *42,* 2679–2724.

Chapter 3: Synthesis and characterization of iridium coated silver decahedral nanoparticles (IrO_{2-x}@AgDeNPs)

3.1 Introduction

Chapter 2 described plasmonic nanoparticles as attractive materials due to their tunable LSPR responses for applications that include surface enhanced Raman spectroscopy, photocatalysis and biological sensing. However, for continued development of new applications, improved performance of plasmonic nanoparticle properties is required.[3.1] One approach to accomplish this is to create core-shells, with plasmonic nanoparticles as the core.[3.1] Core-shell structures can be defined as a combination of a core (inner material) and a shell (outer layer material).[1.9, 3.2] This combination of different materials in a structure allows for new chemical reactivity, thermal stability and enhanced electronic properties for photocatalytic and photoelectrochemical applications.[1.21, 3.1-3.4]

In this chapter the synthesis of uniform IrO_{2-x}@AgDeNPs, IrO_{2-x}@Au@AgDeNPs, IrO_{2-x}@AgDeNP arrays and gold platelets coated with iridium oxide are discussed. IrO_{2-x} notation is used because the oxidation state of the iridium is not known while the original Ir(III) precursor is at least partially oxidizes to Ir(IV). These core-shells were synthesized by the hydrolysis of $IrCl_3$ [3.5] in the presence of AgDeNPs, Au@AgDeNPs and gold platelets. The change of LSPR response is discussed as the IrO_{2-x} shell thickness is increased.

3.2 Experimental IrO_{2-x}@AgDeNP synthesis protocol

Reagents

Premade AgDeNPs as stated in Chapter 2 synthesis protocol and 99.8% pure iridium (III) chloride was used to create IrO_{2-x}@AgDeNPs. Iridium (III) chloride was supplied by Sigma-Aldrich.

Procedure

Synthesis of 100% IrO_{2-x}@AgDeNPs

5 mL of previously prepared AgDeNPs was added to a 20 mL vial. 64 μL of 1.00×10^{-2} M $IrCl_3$ was then added to the same 20 mL vial. The vial was then heated for 30 minutes at 95 ^{o}C. The colour of the sample changed from yellow to orange in the synthesis.

Synthesis of 200% IrO_{2-x}@AgDeNPs

5 mL of previously prepared AgDeNPs was added to a 20 mL vial. 128 μL of 1.00×10^{-2} M $IrCl_3$ was then added to the same 20 mL vial. The vial was then heated for 30 minutes at 95 ^{o}C. The colour of the sample changed from yellow to dark orange/red in the synthesis.

Synthesis of 400% IrO_{2-x}@AgDeNPs

5 mL of previously prepared AgDeNPs was added to a 20 mL vial. 129 μL of 2.00×10^{-2} M $IrCl_3$ was then added to the same 20 mL vial. The vial was then heated for 30 minutes at 95 ^{o}C. The colour of the sample changed from yellow to dark violet in the synthesis.

Instrumentation

UV-vis spectra were recorded using an Ocean Optics QE65000 fiber-optic UV-vis spectrometer. Electron microscopy (EM) imaging was performed with a Hitachi S-5200 using a copper grid with a formvar/carbon film (FCF-200 Electron Microscopy Science). IrO_{2-x}@AgDeNPs were centrifuged using a Thermo scientific Legend Micro 21 centrifuge.

3.3 Results and discussion

IrO_{2-x}@AgDeNP formation process

Figure 3.1 illustrates the LSPR peaks obtainable by increasing the amount of iridium oxide shells formed around AgDeNPs. The size of these IrO_{2-x}@AgDeNPs span from 40 nm to 60 nm (see Table 3.1). Figure 3.1 demonstrates the range of LSPR peaks spanning from 476 nm to 541 nm. The inset in Figure 3.1 is an optical photograph displaying the colour change as the particle size increases from the iridium oxide coating. Therefore, by varying the thickness of the IrO_{2-x} shell a range of accessible LSPR peaks along the visible region are obtained.

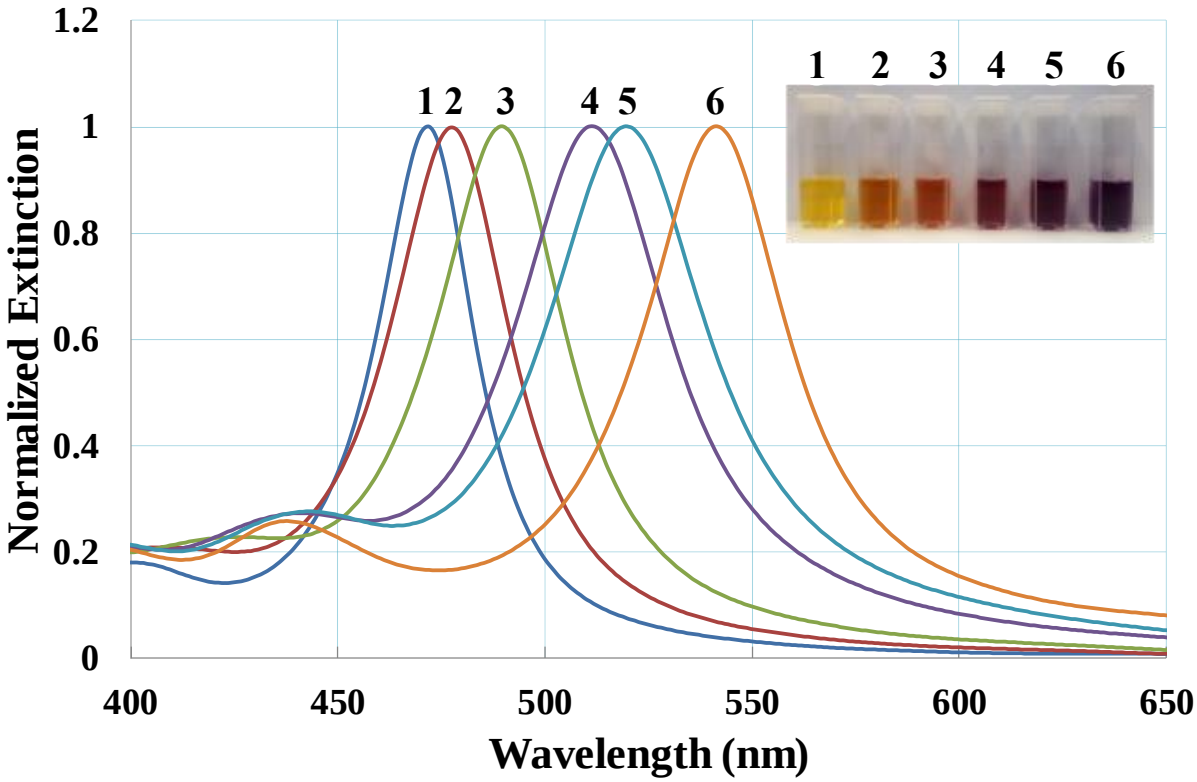

Figure 3.1. Normalized UV-vis spectra of IrO_{2-x}@AgDeNPs with increasing amounts of IrO_{2-x} coating. 1) AgDeNPs, LSPR peak of 471 nm. 2) 1.5:1 $IrCl_3$:AgDeNPs, LSPR peak of 476 nm. 3) 2:1 $IrCl_3$:AgDeNPs, LSPR peak of 489 nm. 4) 2.65:1 $IrCl_3$:AgDeNPs, LSPR peak of 510 nm. 5) 3:1 $IrCl_3$:AgDeNPs, LSPR peak of 520 nm. 6) 9:1 $IrCl_3$:AgDeNPs, LSPR peak of 541 nm. Inset is an optical photograph showing the change in colour as the size of the iridium oxide shell is increased. See Table 3.1 for more information.

The goal of this chapter is to discuss the synthesis of IrO_{2-x} core shells made of AgDeNPs, Au@AgDeNP and gold platelets. The oxidation state of the iridium used in the IrO_{2-x} was not determined. The IrO_{2-x} core shell changes the core materials characteristics, such as NP size. The change in NP size redshifts the LSPR peaks of the AgDeNPs providing a range that spans from 476 nm to 541 nm. Additionally, these IrO_{2-x} core shells are synthesized uniformly, where the IrO_{2-x} core shells self-assembly into arrays (see Figure 3.4).

Figure 3.2 shows the formation of iridium oxide shell by increasing the amount of $IrCl_3$ added to the Au@AgDeNP seeds. 10% Au@AgDeNPs with no iridium oxide coating is

displayed in Figure 3.2a. The 10% for the Au@AgDeNPs is the percentage of gold coating around the AgDeNPs. Figure 3.2b demonstrates a sample with no visible iridium oxide coating despite having a 1:1 molar ratio of $IrCl_3$:Au@AgDeNPs. Figure 3.2c displays a small iridium oxide shell around the Au@AgDeNP core when the molar ratio of $IrCl_3$:Au@AgDeNPs is 2:1. (see Table 3.1). Figure 3.2d exhibits a 14 nm iridium oxide shell around the Au@AgDeNP core when the molar ratio of $IrCl_3$:Au@AgDeNPs is 3:1. (see Table 3.1).

Table 3.1: Summary of the key properties of IrO_{2-x}@AgDeNPs, IrO_{2-x}@Au@AgDeNPs and coated gold platelets: sample description, sample LSPR, and EM size.

Figure Number	Sample	Reaction Time (min)	Description	LSPR (nm)	EM Size (nm)
Fig. 3.1 (1)	PB 272	N/A	AgDeNPs	471	40 ± 1
Fig. 3.1 (2)	PB 744	N/A	1.5:1 $IrCl_3$:AgDeNPs	476	30 ± 1
Fig. 3.1 (3)	PB 746	N/A	2:1 $IrCl_3$:AgDeNPs	489	N/A
Fig. 3.1 (4)	PB 748	N/A	2.65:1 $IrCl_3$:AgDeNPs	510	N/A
Fig. 3.1 (5)	PB 749	13	3:1 $IrCl_3$:AgDeNPs	520	50 ± 2
Fig. 3.1 (6)	PH 364	20	9:1 $IrCl_3$:AgDeNPs	541	60 ± 2
Fig. 3.2a	PB 461	N/A	10% Au@AgDeNPs 10% gold plated AgDeNPs	482	40 ± 1
Fig. 3.2b	PF 247	3	1:1 $IrCl_3$:Au@AgDeNPs	496	40 ± 1
Fig. 3.2c	PF 248	3	2:1 $IrCl_3$:Au@AgDeNPs	520	40 ± 1
Fig. 3.2d	PF 249	20	3:1 $IrCl_3$:Au@AgDeNPs	556	60 ± 2
Fig. 3.4a	PB 280	25	8:1 $IrCl_3$:AgDeNPs	540	65 ± 2
Fig. 3.4b	PB 279	20	4:1 $IrCl_3$:AgDeNPs	538	60 ± 2
Fig. 3.4c	PB 328	20	4:1 $IrCl_3$:AgDeNPs	542	60 ± 2
Fig. 3.4d	PF 249	20	4:1 $IrCl_3$:Au@AgDeNPs	556	60 ± 2
Fig. 3.5a	PB 280	25	8:1 $IrCl_3$:AgDeNPs	540	65 ± 2
Fig. 3.5b	PB 280	25	8:1 $IrCl_3$:AgDeNPs	540	65 ± 2
Fig. 3.6 (1)	ST 483	N/A	Gold platelets	818	N/A
Fig. 3.6 (2)	PF 227	30	2:1 $IrCl_3$:gold platelets	903	100 ± 3
Fig. 3.7a	PF 227	30	2:1 $IrCl_3$:gold platelets	903	100 ± 3
Fig. 3.7b	PH 767	30	4:1 $IrCl_3$:gold platelets	995	80 ± 2

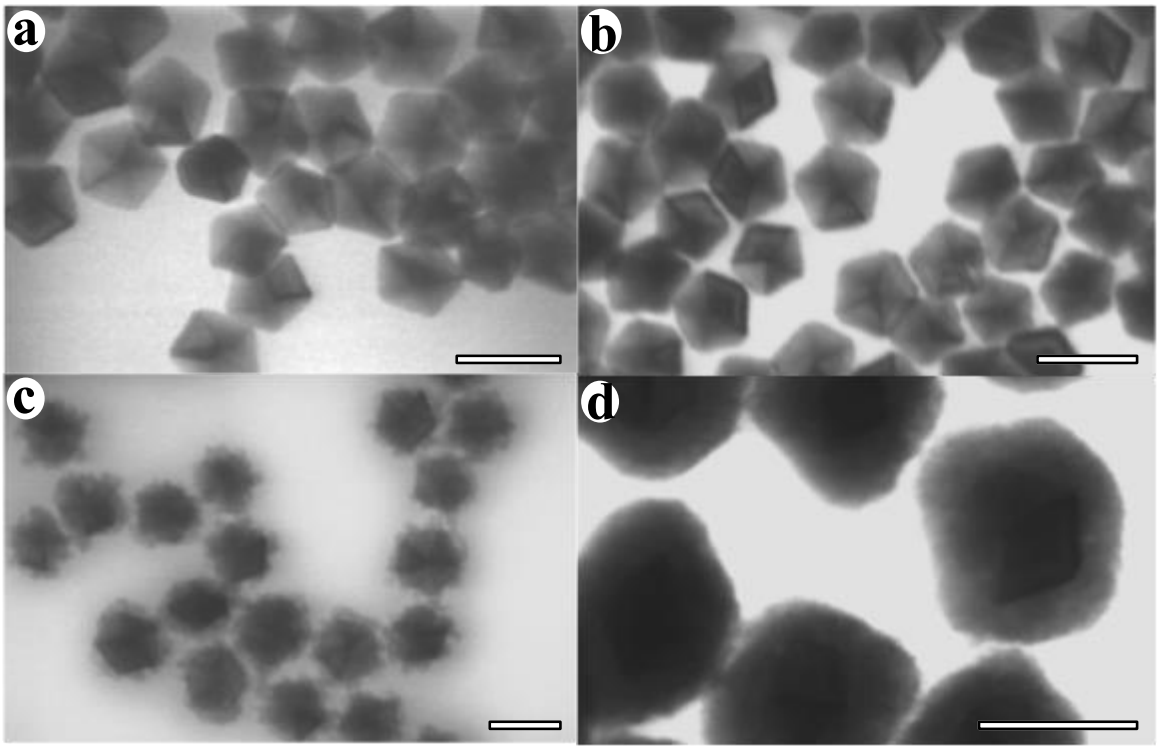

Figure 3.2. TEM images of Au@AgDeNPs and IrO_{2-x}@Au@AgDeNPs showing iridium oxide shell formation. a) 10% Au@AgDeNPs, LSPR peak of 482 nm. b) 1:1 $IrCl_3$:Au@AgDeNPs, LSPR peak of 496 nm. c) 2:1 $IrCl_3$:Au@AgDeNPs, LSPR peak of 520 nm. d) 3:1 $IrCl_3$:Au@AgDeNPs, LSPR peak of 556 nm. All scale bars are 50 nm. See Table 3.1 for more information.

Figure 3.3 demonstrates the increase in particle size as the IrO_{2-x}@AgDeNPs are formed and grow. The diameter of these IrO_{2-x}@AgDeNPs was determined by their respective EM images. Figure 3.3 illustrates that the minimum amount of time needed to form an iridium oxide coating around the AgDeNP precursor is 25 minutes. The results of Figure 3.3 can be used for the interpolation of a specific time, to form iridium oxide coatings with controlled thickness.

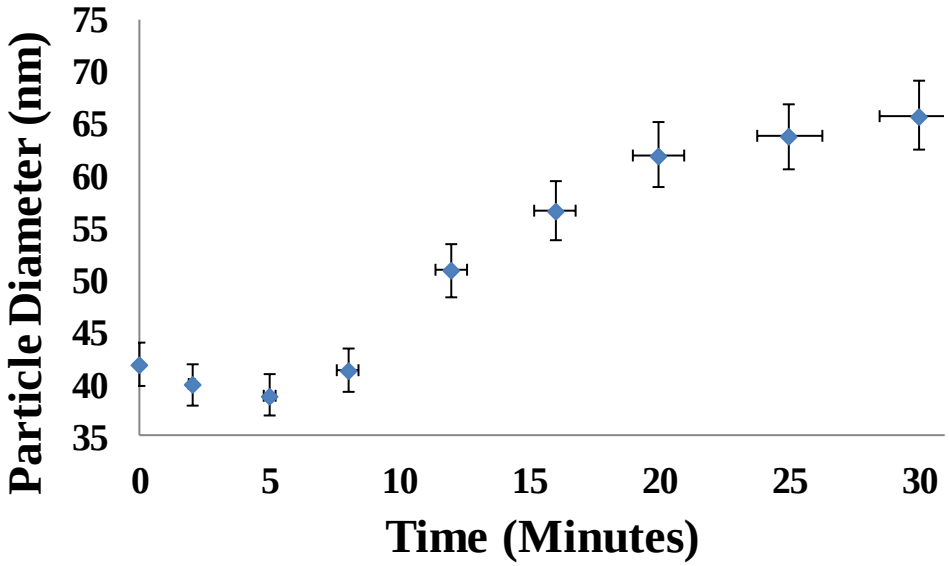

Figure 3.3. Change in IrO_{2-x}@AgDeNP diameter as a function of the reaction time during the formation of iridium oxide shell.

Figure 3.4 demonstrates the packing of IrO_{2-x}@AgDeNPs and IrO_{2-x}@Au@AgDeNPs into uniform arrays. Figure 3.4a to Figure 3.4c illustrates the self-assembly of IrO_{2-x}@AgDeNPs. The self-assembly of IrO_{2-x}@Au@AgDeNPs is shown in Figure 3.4d. This close packing requires the AgDeNPs to be uniform in size but also a uniform coating of iridium oxide across all AgDeNPs.

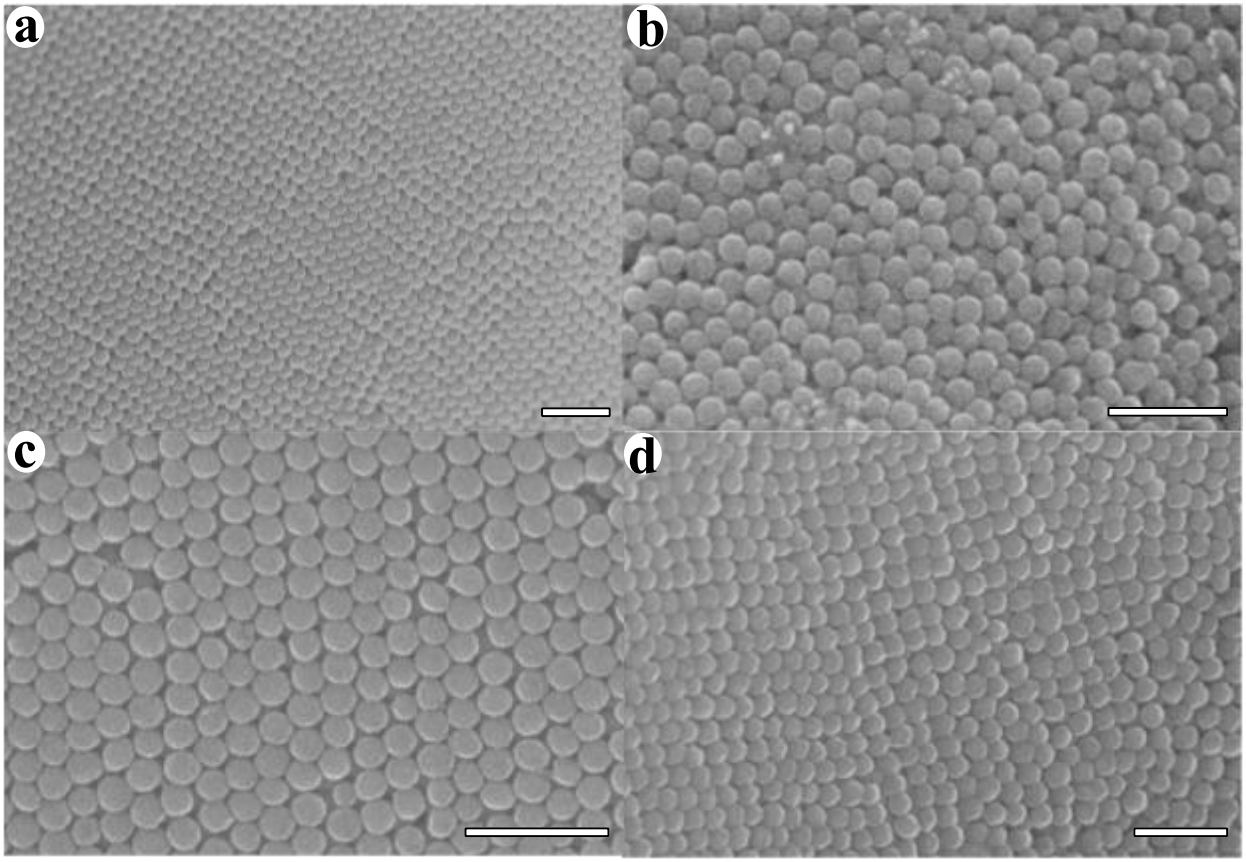

Figure 3.4. SEM images showing the self-assembly of IrO_{2-x}@AgDeNPs and IrO_{2-x}@Au@AgDeNPs. a) 8:1 $IrCl_3$: AgDeNPs, LSPR peak of 540 nm. b) 4:1 $IrCl_3$:AgDeNPs, LSPR peak of 538 nm. c) 4:1 $IrCl_3$:AgDeNPs, LSPR peak of 542 nm. d) 4:1 $IrCl_3$:Au@AgDeNPs, LSPR peak of 556 nm. All scale bars are 300 nm. See Table 3.1 for more information.

Figure 3.5 demonstrates the interaction of light with IrO_{2-x}@AgDeNPs in a form of thin films. Figure 3.5a illustrates the transmission of light through the IrO_{2-x}@AgDeNP thin film. Figure 3.5b displays the reflection of light on the IrO_{2-x}@AgDeNP thin film. Figure 3.5 highlights the structural colour displayed when light reflects from the ordered IrO_{2-x}@AgDeNPs.

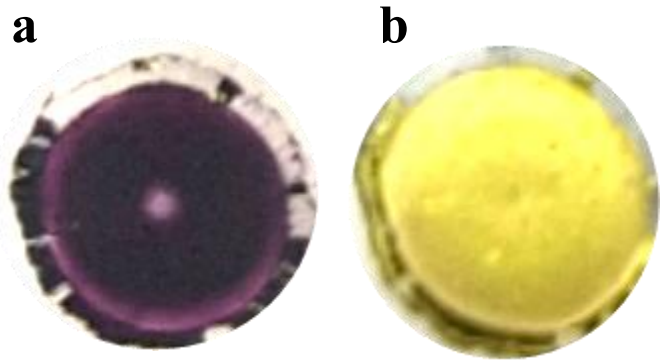

Figure 3.5. Optical photographs showing the reflection of light on IrO_{2-x}@AgDeNP thin films. a) Transmission of light through IrO_{2-x}@AgDeNP thin film. b) Reflection of light through IrO_{2-x}@AgDeNP thin film. See Table 3.1 for more information.

The iridium oxide coating can be applied to other NP morphologies. The UV-vis spectra in Figure 3.6 shows iridium oxide coating of gold platelets in a 2:1 $IrCl_3$:gold platelets molar ratio. The iridium oxide coating redshifts the LSPR peaks from 818 nm to 903 nm.

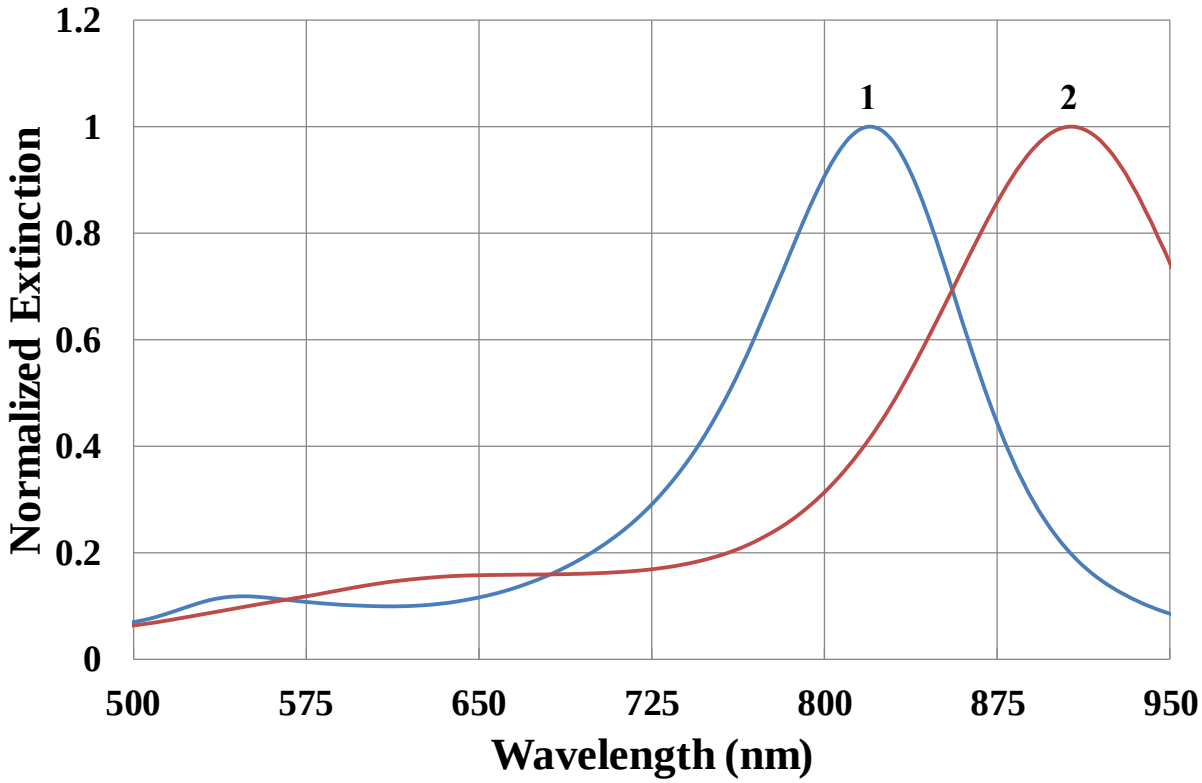

Figure 3.6. Normalized UV-vis spectra of IrO_{2-x} coated gold platelets. 1) Gold platelets, LSPR peak of 818 nm. 2) 2:1 $IrCl_3$:gold platelets, LSPR peak of 903 nm. See Table 3.1 for more information.

Figure 3.7 expands on the UV-vis graph in Figure 3.6 by showing EM images of different iridium oxide coatings prepared for gold platelets. Figure 3.7a displays iridium coated gold platelets made with a 2:1 $IrCl_3$:gold platelets molar ratio, red shifting the LSPR peak from 818 nm to 903 nm (see Figure 3.6). Figure 3.7b demonstrates iridium coated gold platelets made with a 4:1 $IrCl_3$:gold platelets molar ratio, resulting in the LSPR peak red shifting to 995 nm. Therefore, by modifying the molar ratio of $IrCl_3$:gold platelets the LSPR peaks can be specifically tuned. Furthermore, it shows that the iridium coating is versatile because it can provide uniform coatings for to different NP morphologies AgDeNPs and gold platelets.

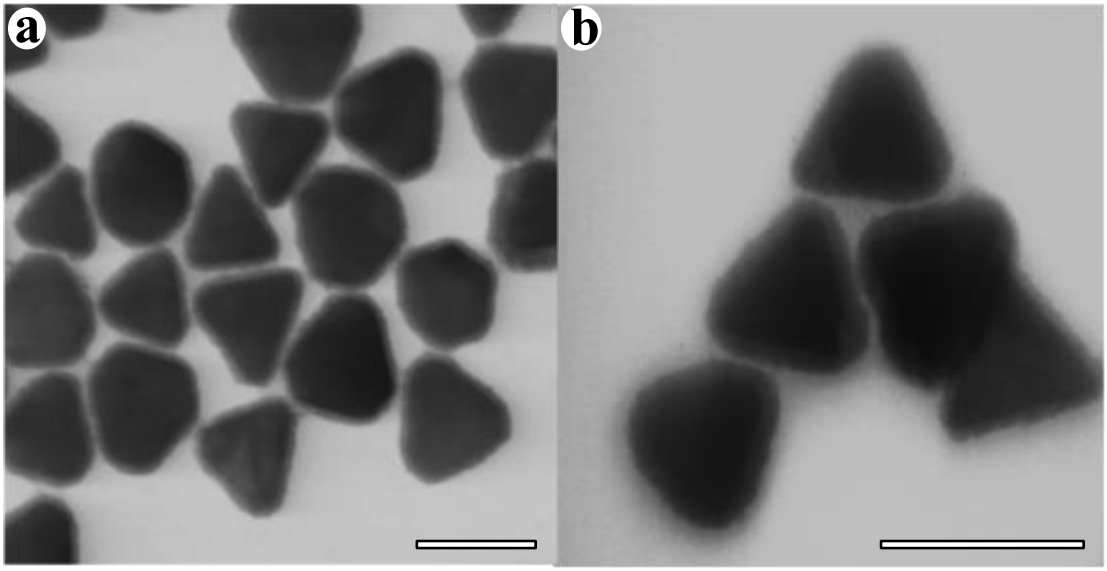

Figure 3.7. EM images of IrO_{2-x} coatings of gold platelets. a) 2:1 $IrCl_3$:gold platelets, LSPR peak of 903 nm. b) 4:1 $IrCl_3$:gold platelets, LSPR peak of 995 nm. All scale bars are 100 nm. See Table 3.1 for more information.

3.4 Conclusion

The iridium oxide coating of AgDeNPs creates core-shell structures that are tuned by their shell thickness, giving LSPR peaks from 476 nm to 541 nm. When IrO_{2-x}@AgDeNPs are formed with a uniform iridium oxide coating and size controlled AgDeNPs, IrO_{2-x}@AgDeNPs self-assemble into highly ordered arrays. The highly ordered arrays can be made into thin films that upon the reflection of light, display the complementary colour. The iridium oxide coating

can be applied to Au@AgDeNPs and gold platelets creating addition functionality as a multi-layered core shell design. These iridium oxide core shells can then be utilized in applications, such as surface enhanced Raman scattering (SERS),[1.29] surface plasmon resonance (SPR) sensing[1.29] and catalysis.[1.3,1.21]

3.5 References

The results from this chapter were published.

[1.29]Cathcart, N.; Murshid, N.; Campbell, P.; Kitaev, V. *ACS Appl. Nano Mater.* **2018**, *1*, 6514–6524.

[3.1]El-Toni, A. M.; Habila, M. A.; Labis, J. P.; ALOthman, Z. A.; Alhoshan, M.; Elzatahry, A. A.; Zhang, F. *Nanoscale* **2016,** *8*, 2510–2531.

[3.2]Li, A.; Zhu, W.; Li, C.; Wang, T.; Gong, J. *Chem. Soc. Rev.* **2019**, *48*, 1874–1907.

[3.3]Cui, M. L.; Chen, Y. S.; Xie, Q. F.; Yang, D. P.; Han, M. Y. *Coord. Chem. Rev.* **2019**, *387*, 450–462.

[3.4]Shi, Q.; Zhu, C.; Du, D.; Lin, Y. *Chem. Soc. Rev.* **2019**, *48*, 3181–3192.

[3.5]Bestaoui, N.; Prouzet, E. *Chem. Mater.* **1997**, *9***,** 1036–1041.

Chapter 4: Synthesis and characterization of 3-D and 1-D hematite nanoparticles

4.1 Introduction

Uniform nanoparticles (NPs) have remarkable properties due to their chemical composition, particle size, shape and structure[4.1] These parameters determine what characteristics (optical, catalytic, electric) are exhibited.[4.1] Metal oxides are very important in our modern society due to their unique optical, catalytic, photoelectrochemical nanoscale properties. Iron oxides are valuable materials due to their relative abundance for catalysis,[4.2] photo-oxidation,[4.2] photoelectrochemical cells (PEC) and serving as pigments.[4.3,4.4]

In 1972 Fujishama and Honda demonstrated photoelectrochemical (PEC) water splitting by the electrochemical photolysis of water with TiO_2, creating an elegant and environmentally benign pathway to produce H_2.[1.22]

Cathode reaction: $2\ H_2O_{(l)} + 2\ e^- \rightarrow 2\ OH^-_{(aq)} + H_{2(g)}$

Anode reaction: $2\ OH^-_{(aq)} \rightarrow ½\ O_{2(g)} + H_2O_{(l)} + 2\ e^-$

Overall reaction: $H_2O_{(l)} \rightarrow ½\ O_{2(g)} + H_{2(g)}\ \Delta G = 237.2\ kJ\ mol^{-1}$

To achieve direct water splitting using two electrodes, the following prerequisites must be satisfied simultaneously: 1) the conduction and valence bands must straddle the water oxidation and reduction potentials, 2) the semiconductor must absorb a substantial portion of the incident visible light, 3) the photogenerated charge carriers must be highly selective for water splitting, and 4) the electrode must stand the tests of harsh environmental conditions such as water, salts, and strong sunlight.[1.22] Hematite (α-Fe_2O_3) is one of the most promising photoanode materials for photoelectrochemical (PEC) water oxidation due to its favorable bandgap of

2.1 eV.[1.23-1.25] However, despite the optimal band gap, hematite is an indirect band-gap semiconductor. Thus, the performance of the hematite photoanode for water oxidation is restricted by its poor electrical conductivity, poor charge separation, short carrier lifetimes[4.5] and transfer efficiency.[1.23] These limitations can be solved with element doping, morphology engineering and surface modification.[1.23,1.26,4.5] Semiconductor properties of hematite have been extensively characterized[4.6, 4.7] since they are important for applications that include water splitting[4.8-4.11] and removing contaminants in the environment.[4.12]

There are three crystalline polymorphs of Fe_2O_3 that have different structural and magnetic properties.[4.6, 4.13, 4.14] These three polymorphs are hematite (α-Fe_2O_3), maghemite (γ-Fe_2O_3) and ε-Fe_2O_3.[4.14] The highly crystalline α-Fe_2O_3 and γ-Fe_2O_3 occur in nature and are the most commonly used polymorphs. Akageneite (β-FeOOH),is an intermediate that is formed by heating iron salt ($FeCl_3 \cdot 6H_2O$) while ε-Fe_2O_3 is a polymorph synthesized only as nanostructures in the laboratory.[4.13]

These crystalline polymorphs can be produced as powders, thin films, composites or coated particles.[4.13] Hematite NPs have been synthesized in morphologies that include platelets, polyhedrons, pseudo cubes and peanut-like structures.[4.3] The size and shape of hematite NPs can be adjusted by carefully controlling the processing parameters such as reaction time, temperature and the use of shape selective ligands[4.3,4.15] It is known that ligands absorbed on the surface of NPs exhibit steric effects that have a great influence on the NPs self-assembly behavior.[4.15] For example, PVP was found to be widely used as a protective agent to prevent NPs from aggregation in the chemical preparation of crystals.[4.15]

In this chapter different uniform hematite NP morphologies were synthesized, and their properties were characterized for potential applications. These hematite NPs were produced by first heating iron salt ($FeCl_3 \cdot 6H_2O$). An intermediate that forms from this heating is β-FeOOH, called akageneite. This intermediate has the shape of long rods or spindles.[4.13] The akageneite NPs then transform into hematite or α-Fe_2O_3 from additional heating.[4.13] These hematite NPs size and dispersity was then improved by modifying temperature, time for growth and the utilization of shape selective ligands, such as PVP and PDDA.[4.15,4.16] This resulted in the synthesis of uniform rhombohedral hematite NPs. These uniform hematite NPs were then used as seeds to create 1-D hematite NPs. The structure of these 1-D hematite NPs was explored by modifying additives, heating times and regrowth strategies. 1-D hematite NPs with controllable size comes from the complexation of citric acid in the nucleation stage of the hematite seeds. Citric acid complexes the iron ions and extends the 3-D hematite nuclei along the C_3 axis edge creating the 1-D hematite NPs (see Figure 4.2). The quality of all particles was analyzed using EM imaging for visual representation. Dynamic light scattering (DLS) was used to determine average particle size and polydispersity (PDI). The purpose of this new hematite morphology is to be used as a photoelectrochemical cell by doping the inner structure with iridium oxide and the C_3 axis caps with platinum NPs (see Figure 4.11).

4.2 Experimental hematite synthesis protocol

Reagents

Iron (III) chloride hexahydrate (99-102%) $FeCl_3 \cdot 6H_2O$, ≥99% anhydrous citric acid (CA), very low and low molecular weight polydiallyldimethylammonium chloride (PDDA), polyvinylpyrrolidone (PVP) (M_W=40 K) was supplied by Caledon. 99.8% pure iridium (III) chloride was used to dope 1-D hematite NPs. High-purity deionized water (>18.4 M Ω cm) was produced using Millipore A10 Milli-Q.

Instrumentation

Hematite NPs were heated in a Heidolph MR 3004 Safety heat block, Accublock digital dry bath heat block and IKA C-mag HS7 heat block. Hematite NPs were centrifuged using both a Thermo scientific Legend Micro 21 centrifuge and Medifuge centrifuge. Dynamic light scattering (DLS) particle size was obtained by a Malvrin Zetasizer Nano ZS.

Procedure

Synthesis of general hematite NPs

A 20 mL vial of 8.8 mM iron (III) chloride hexahydrate was created by diluting a 1.00 x 10^{-1} M stock solution of iron (III) chloride hexahydrate. The 8.8 mM iron (III) chloride hexahydrate vial was then heated under different hydrolysis conditions in a heat block from one to twenty days. As the 8.8 mM iron (III) chloride hexahydrate vial is heated the colour changes from yellow to orange then to red. When the hematite NPs reach a size >100 nm, the hematite NPs will demonstrate a high level of turbidity. After two days the hematite NPs will precipitate. When optimal synthesis conditions are used (see Chapter 5) hematite NPs will strongly reflect a red colour and have a shiny appearance of the dispersion under bright light.

Synthesis of short 1-D C_3 axis hematite NPs

A 20 mL vial of 8.8 mM iron (III) chloride hexahydrate was created by diluting a 1.00 x 10^{-1} M solution of iron (III) chloride hexahydrate. 70 µl of 1.00 x 10^{-1} M PVP was added to this vial and heated using a multi temperature heating regime (MH) (see Table 4.1) in a heat block for nine days. After nine days another 20 mL vial of 8.8 mM iron (III) chloride hexahydrate was created by diluting a 1.00 x 10^{-1} M stock solution of iron (III) chloride hexahydrate. This new iron (III) chloride hexahydrate stock solution is added in a 1:1 molar ratio to the previously heated

hematite seeds. The regrowth system was then heated for five days. As the vial containing 8.8 mM iron (III) chloride hexahydrate is heated, the dispersion colour changes from yellow to orange then to red. When the hematite NPs reach a size >100 nm, the hematite NPs will demonstrate a high level of turbidity. After two days the hematite NPs will precipitate. These NPs will have 1-D structure. (See Table 4.1).

Synthesis of long rough 1-D C_3 axis hematite NPs

A 20 mL vial of 8.8 mM iron (III) chloride hexahydrate was created by diluting a 1.00×10^{-1} M stock solution of iron (III) chloride hexahydrate. 44 µl of 2.00×10^{-1} M citric acid was added to this vial and heated at 95ºC in a heat block for three days. After three days another 20 mL vial of 8.8 mM iron (III) chloride hexahydrate was created by diluting a 1.00×10^{-1} M stock solution of iron (III) chloride hexahydrate. This new iron (III) chloride hexahydrate stock solution is added in a 2:1 molar ratio to the previously heated hematite seeds. The regrowth system was then heated, typically for three days. As the 8.8 mM iron (III) chloride hexahydrate vial is heated the colour changes from yellow to orange then to red. When the hematite NPs reach a size >100 nm, the hematite NPs will demonstrate a high level of turbidity. After two days the hematite NPs will precipitate. These NPs will have an elongated 1-D structure. (See Table 4.1).

Synthesis of long defined 1-D C_3 axis hematite NPs

A 20 mL vial of 8.8 mM iron (III) chloride hexahydrate was created by diluting a 1.00×10^{-1} M stock solution of iron (III) chloride hexahydrate. 88 µl of 1.00×10^{-1} M PDDA was added to this vial. 352 µl 1.00×10^{-1} M of PVP was added to this vial. 44 µl of 2.00×10^{-2} M citric acid was added to this vial and then heated at 95ºC in a heat block for one day. The next day another 20 mL vial of 8.8 mM iron (III) chloride hexahydrate was created by diluting a

1.00 x 10^{-1} M stock solution of iron (III) chloride hexahydrate. This new iron (III) chloride hexahydrate stock solution is added in a 2:1 molar ratio to the previously heated hematite seeds. The regrowth system was then heated for seven days. As the 8.8 mM iron (III) chloride hexahydrate vial is heated the colour changes from yellow to orange then to red. When the hematite NPs reach a size >100 nm, the hematite NPs will demonstrate a high level of turbidity. After two days the hematite NPs will precipitate. These NPs will have an elongated 1-D structure. (See Table 4.1).

Table 4.1: Summary of abbreviations used in Chapter 4.

Terms	Description
"MH"	"MH" or multi-step heating is a lab technical term where a hematite sample is heated at specific temperature for a specific set of time. This term is used to describe a hematite sample heating at 50°C for 1 day then at 70°C the second day. Then it is heated at 95°C for a minimum of 3 days. This protocol is used for creating large rhombohedral type cubes specifically with PVP as an additive.
"MH*"	"MH*" or multi-step heating is a lab technical term where a hematite sample is heated at specific temperature for a specific set of time. This term is used to describe a hematite sample heating at 70°C the first day. Then it is heated at 95°C for a minimum of 3 days.
"2x of 1x+3x"	These symbols are to represent that this sample has been regrown but not in the typical fashion described in the procedure. Most 1-D hematite regrowths are synthesized using a 2:1 molar ratio of iron precursor to hematite seeds and heated for a minimum of 3 days at 95°C. Notation of "2x" represents that the molar ratio of iron precursor to hematite seeds is still 2:1 but it has only been heated at 95°C for 1 day. Thus for notation '1x+3x', the protocol to synthesize this sample would be a 1:1 molar ratio of iron precursor to hematite seeds heated at 95°C for 1 day, then on the next day a 3:1 molar ratio of iron precursor to hematite seeds is added to the sample and heated at 95°C for another day. For all steps the iron concentration is always fixed constant at 8.8 mM.
"R" (additives)	This symbol denotes that this sample has been regrown. The content in the brackets describe what additives were contained in the seed.
"S"	This symbol indicates that this sample is a rhombohedral hematite seed.
"CA"	This symbol is a short form notation for citric acid.
"OA"	This symbol is a short form notation for oxalic acid
"AA"	This symbol is a short form notation for aspartic acid
"Candy"	This term is used to describe the structure of the shortest 1-D hematite growth. (Figure 4.2b)
"Spear"	This term is used to describe the structure of the mid to longest 1-D hematite growth. (Figure 4.2c)

4.3 Results and discussion

Figure 4.1 displays different hematite nanostructures created by modifying reaction parameters. Figure 4.1a illustrates 3-D rhombohedral hematite NPs created with PVP. PVP was used as a shape selective ligand to produce 3-D hematite NPs with larger particle size and low polydispersity. The hematite NPs in Figure 4.1a have a size of 187 nm and a PDI of 0.044, where 3-D hematite NPs with no PVP illustrated in Figure 4.4c have a size of 154 nm and PDI of 0.151. Figure 4.1b demonstrates a seeded regrowth of hematite seeds with PVP, resulting in a short 1-D hematite structure. This growth is an extension of the C_3 axis with the formation of caps at either end (see Figure 4.3). Figure 4.1c illustrates a variation of this 1-D regrowth with the addition of $IrCl_3$ resulting in this new structure having a spikier centre. Figure 4.1d displays a 1-D regrowth with the use of citric acid (CA) instead of PVP. Modifying the amount of citric acid used in the 1-D regrowths, longer 1-D hematite NPs are created (see Figure 4.6). Figure 4.1e illustrates 1-D hematite NPs with aspartic acid (AA). This hematite structure has been regrown multiple times giving a long 1-D growth with a rough centre. Figure 4.1f demonstrates 1-D hematite NPs with PVP, PDDA and citric acid. This hematite structure has a crystalline centre resembling 3-D rhombohedral hematite NPs stacked along the C_3 axis (see Figure 4.2d).

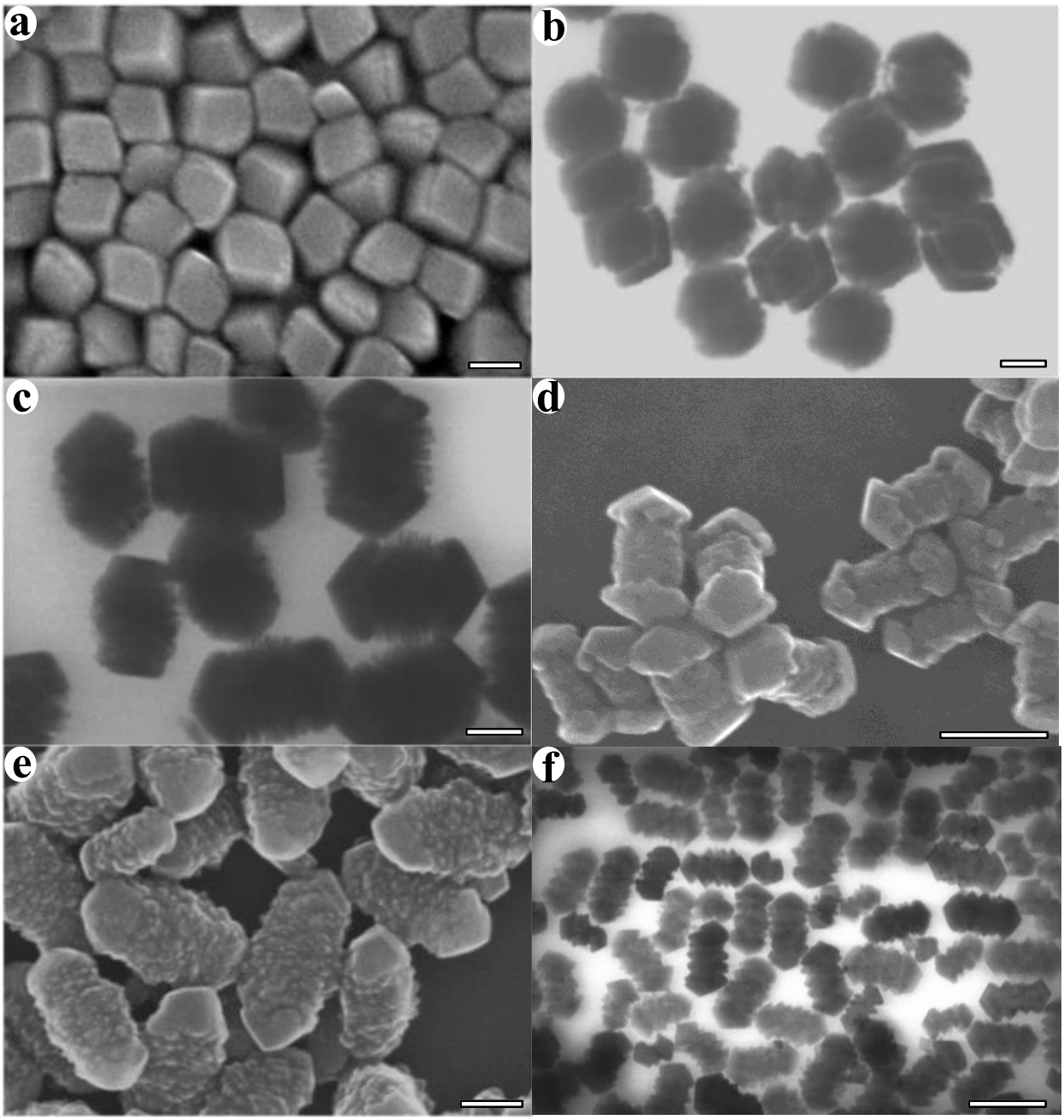

Figure 4.1. EM images of different hematite NP morphologies. a) Rhombohedral hematite (50:1 Fe:PVP). b) 1:1 R (25:1 Fe:PVP). c) 2:1 R (25:1 Fe:PVP, 200:1 Fe:$IrCl_3$). d) 2:1 R (400:1 Fe:CA). e) 6th 1:1 R (50:1 Fe:AA). f) 2x R (5:1 Fe:PVP, 20:1 Fe:PDDA and 200:1 Fe:CA). All scale bars are 100 nm. See Table 4.2 for more information.

Figure 4.2 demonstrates the diversity of hematite morphologies that can be synthesized via hydrothermal treatment of iron salt ($FeCl_3 \cdot 6H_2O$). The 60 nm rhombohedral hematite NPs were synthesized based on heating iron (III) chloride salt, transforming into akageneite and then converting into hematite. This rhombohedral morphology was then refined by adding additives, such as polyvinylpyrrolidone (PVP), polydiallyldiethlyammonium chloride (PDDA), and citric acid (CA) into the synthesis. These added reagents improve the polydispersity of the rhombohedral hematite NPs, providing well defined hematite seeds for the development of other hematite NPs (see Figure 4.2). Figure 4.2a give an example where the incorporation of PVP in the initial rhombohedral hematite synthesis resulted in larger hematite rhombohedral NPs with a great PDI of 0.044 (see Table 4.2). Figure 4.2b illustrates that by re-growing rhombohedral hematite seeds with PVP, a "bracket or candy" like morphology is formed. This growth is a 1-D extension of the rhombohedral hematite morphology along the C_3 axis. The outer ends of the structure are fitted with caps, which are a slice of a corner from the rhombohedral hematite morphology (see Figure 4.3). Figure 4.2c displays NPs with a longer 1-D "spear" like hematite morphology obtained by the regrowth of hematite seeds containing citric acid. The length of these particles can be modified via how much citric acid is present in the regrowth. This 1-D hematite morphology can have a crystalline centre with the addition of PDDA, PVP and citric acid in the regrowth synthesis. Figure 4.2d demonstrates 1-D hematite NPs with a more crystalline centre compared to the hematite NPs in Figure 4.2c.

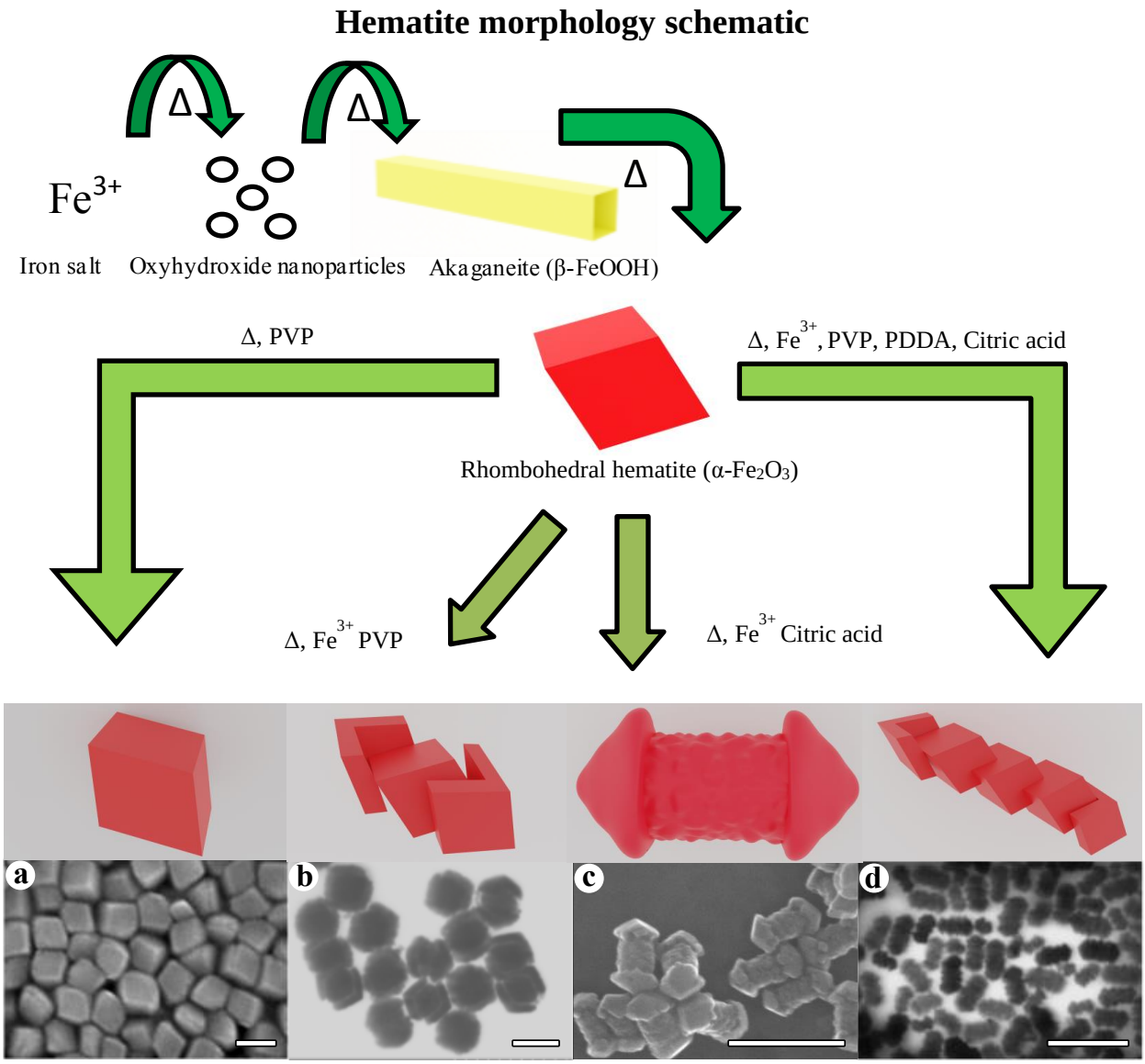

Figure 4.2. EM images of different hematite NP morphologies. a) 8.8 mM rhombohedral hematite (50:1 Fe:PVP). b) 1:1 R (25:1 Fe:PVP). c) 2:1 R (400:1 Fe:CA). d) 2x R (5:1 Fe:PVP, 20:1 Fe:PDDA and 200:1 Fe:CA). All scale bars are 200 nm. See Table 4.2 for more information

Table 4.2: Summary of synthetized amorphous iron oxyhydroxide, akageneite and hematite NPs

Figure Name	Sample Name	Description	DLS Z-avg (nm)	DLS PDI
Fig. 4.1a	PA 995	S MH (50:1 Fe:PVP 1300k) heated 6 days	187 ± 6	0.044
Fig. 4.1b	PB 33	1:1 R (25:1 Fe:PVP) heated 5 days	288 ± 9	0.211
Fig. 4.1c	PB 153	2:1 R (25:1 Fe:PVP 200:1 Fe:$IrCl_3$)	217 ± 7	0.095
Fig. 4.1d	PE 820	2:1 R (400:1 Fe:CA) heated 9 days	91 ± 3	0.070
Fig. 4.1e	PA 559	6^{th} 1:1 R (50:1 Fe:AA)	149 ± 4	0.085
Fig. 4.1f	PF 353	2X R (5:1 Fe:PVP 20:1 Fe:PDDA and 200:1 Fe:CA)	79 ± 2	0.041
Fig. 4.2a	PA 995	S MH (50:1 Fe:PVP 1300k) heated 6 days	187 ± 6	0.044
Fig. 4.2b	PB 33	1:1 R (25:1 Fe:PVP) heated 5 days	288 ± 9	0.211
Fig. 4.2c	PE 820	2:1 R (400:1 Fe:CA) heated 9 days	91 ± 3	0.070
Fig. 4.2d	PF 353	2X R (5:1 Fe:PVP 20:1 Fe:PDDA and 200:1 Fe:CA)	79 ± 2	0.041
Fig. 4.3a	PF 223	S (80:1 Fe:PDDA)	121 ± 4	0.065
Fig. 4.3b	PE 781	4:1 R (250:1 Fe:OA)	118 ± 4	0.013
Fig. 4.3c	PB 33	1:1 R (25:1 Fe:PVP)	288 ± 9	0.211
Fig. 4.4a	PA 959	Amorphous oxyhydroxide NPs with ammonia	N/A	N/A
Fig. 4.4b	PH 770	S akageneite (no heat)	108 ± 3	0.178
Fig. 4.4c	PE 657	Heated on middle oven shelf for 1 day then at 70°C for 1 day, then at 95°C for 10 days	154 ± 5	0.151
Fig. 4.4d	PA 856	S MH (5:1 Fe:PVP) heated 14 days	176 ± 5	0.030
Fig. 4.5a	PE 731	2:1 R (no additives)	178 ± 5	0.115
Fig. 4.5b	PB 33	1:1 R (25:1 Fe:PVP) heated 5 days	288 ± 9	0.211
Fig. 4.5c	PE 820	2:1 R (400:1 Fe:CA) heated 9 days	91 ± 3	0.070
Fig. 4.5d	PE 819	2:1 R (200:1 Fe:CA) heated 9 days	95 ± 3	0.084
Fig. 4.6a	PE 731	2:1 R (no additives)	178 ± 5	0.115
Fig. 4.6b	PE 952	2:1 R (800:1 Fe:CA)	92 ± 3	0.041
Fig. 4.6c	PH 147	2:1 R (600:1 Fe:CA)	91 ± 3	0.026
Fig. 4.6d	PE 820	2:1 R (400:1 Fe:CA) heated 9 days	91 ± 3	0.070
Fig. 4.6e	PE 819	2:1 R (200:1 Fe:CA) heated 9 days	95 ± 3	0.084
Fig. 4.6f	PE 818	2:1 R (100:1 Fe:CA) heated 9 days	79 ± 2	0.070
Fig. 4.7a	PE 731	2:1 R (no additives)	178 ± 5	0.115
Fig. 4.7b	PB 32	1:1 R (10:1 Fe:PVP) heated 5 days	220 ± 7	0.080
Fig. 4.7c	PB 33	1:1 R (25:1 Fe:PVP) heated 5 days	288 ± 9	0.211

Fig. 4.7d	PB 35	1:1 R (80:1 Fe:PVP) heated 5 days	382 ± 11	0.241
Fig. 4.8a	PE 731	2:1 R (no additives)	178 ± 5	0.115
Fig. 4.8b	PF 232	2:1 R (5:1 Fe:PDDA)	529 ± 16	0.354
Fig. 4.8c	PF 230	2:1 R (20:1 Fe:PDDA)	96 ± 3	0.026
Fig. 4.8d	PF 234	2:1 R (40:1 Fe:PDDA)	89 ± 3	0.048
Fig. 4.9a	PE 731	2:1 R (no additives)	178 ± 5	0.115
Fig. 4.9b	PE 799	2:1 R (333:1 Fe:OA)	92 ± 3	0.022
Fig. 4.9c	PE 754	2:1 R (250:1 Fe:OA)	99 ± 3	0.063
Fig. 4.9d	PE 752	2:1 R (20:1 Fe:OA)	130 ± 4	0.142
Fig. 4.10a	PE 731	2:1 R (no additives)	178 ± 5	0.115
Fig. 4.10b	PA 465	2:1 R (10:1 Fe:AA)	62 ± 2	0.071
Fig. 4.10c	PA 466	2:1 R (20:1 Fe:AA)	107 ± 3	0.196
Fig. 4.10d	PA 567	2:1 R (40:1 Fe:AA)	107 ± 3	0.158

Figure 4.3 presents side-by-side comparison of EM images and models of the hematite end caps obtainable for the 1-D hematite nanostructure. The initial stages of the end cap formation begin with the removal of the C_3 axis corner of the rhombohedral hematite NP (Figure 4.3a). The formation of the end caps continues in this C_3 axis corner vertex and are reformed as bigger end caps resembling the removed C_3 axis corner shown in Figure 4.3a. The different structural end caps obtained for the hematite 1-D structures are demonstrated in Figure 4.3b and Figure 4.3c. The longer 1-D hematite NPs typically exhibit the end caps illustrated in Figure 4.3b. The shorter 1-D hematite NPs normally show the end caps as shown in Figure 4.3c.

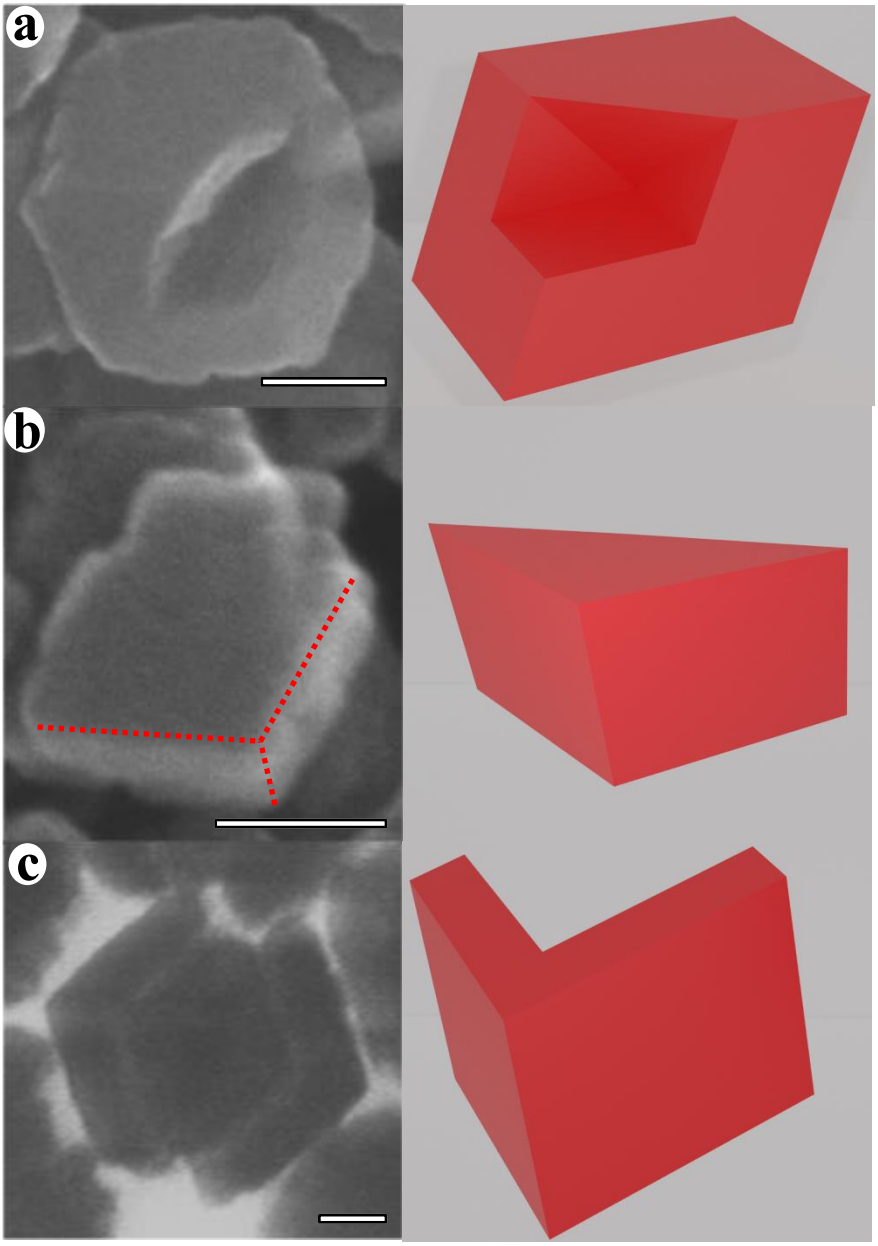

Figure 4.3. EM images showing hematite corners and caps of hematite NPs. a) S (80:1 Fe:PDDA). b) 4:1 R (250:1 Fe:OA). c) 1:1 R (25:1 Fe:PVP). All scale bars are 50 nm. See Table 4.2 for more information.

Figure 4.4 depicts EM images of the transformation stages of iron salt to hematite NPs. The initial stage starts with amorphous iron being formed from the hydrolysis of iron salt (Figure 4.4a). Upon continued heating of the amorphous iron, it is subsequently converted into akageneite shown in Figure 4.4b. The akageneite then transforms into hematite NPs with

additional heating (Figure 4.4c). However, these rhombohedral hematite NP's size and dispersity can be improved with the addition of shape selective ligands. For example, the addition of PVP into the hematite NP synthesis (Figure 4.4d) produces hematite NPs with a better PDI of 0.030. This is an improvement over the PDI of 0.151 for the NPs illustrated in Figure 4.4c (see Table 4.2). Uniform rhombohedral hematite NPs are important because they are used as seeds for the development of well defined 1-D hematite NPs.

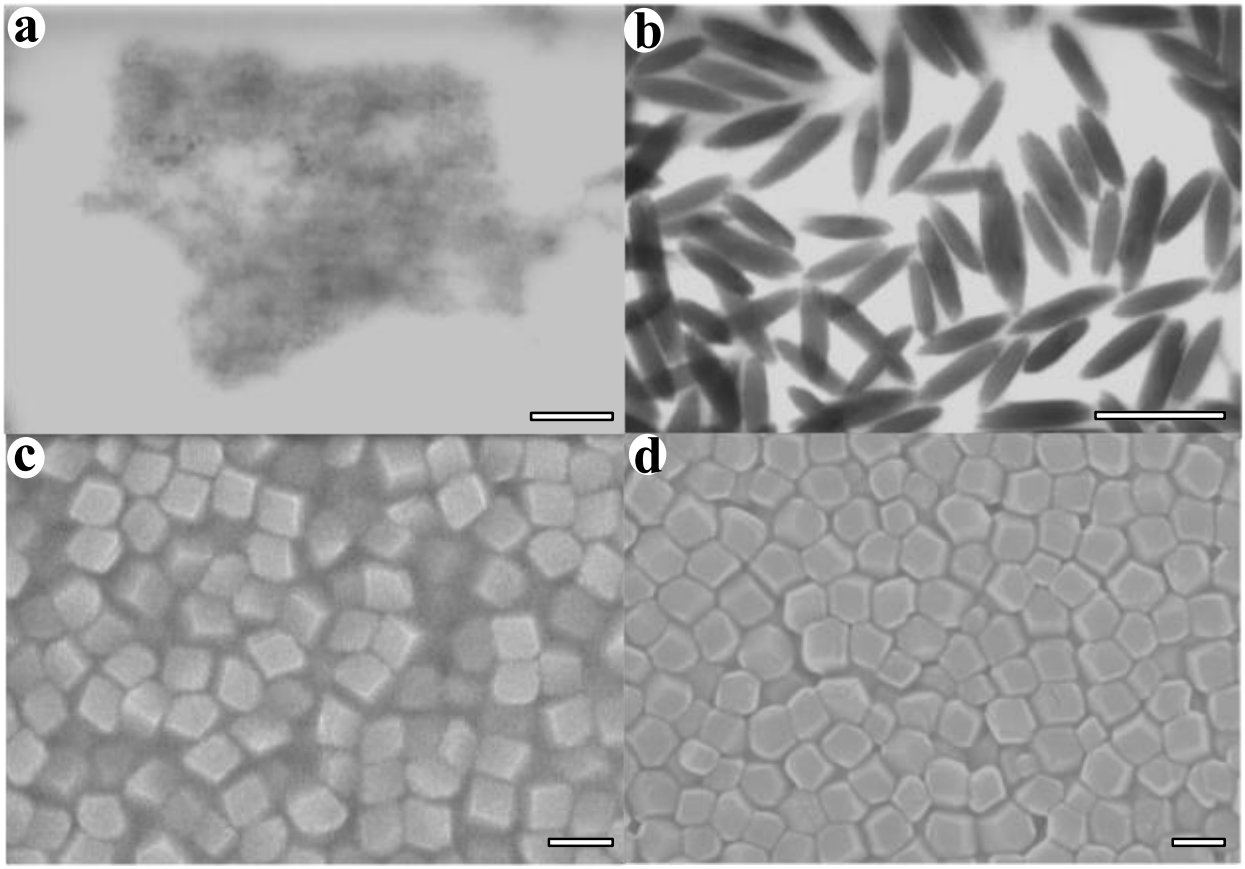

Figure 4.4. EM images showing the formation of rhombohedral hematite NPs. a) Amorphous iron hydroxide NPs. b) Akageneite (no heat). c) 8.8 mM hematite MH* (no additives). d) 8.8 mM hematite MH (80:1 Fe:PVP). All scale bars are 100 nm. See Table 4.2 for more information.

Figure 4.5 depicts the different lengths that are obtainable for the 1-D hematite morphology. Figure 4.5b shows the shortest 1-D regrowth, where these NPs have a "candy-like"

appearance. These NPs were synthesized with PVP as an additive in the rhombohedral hematite seeds. The 1-D design can be extended to longer lengths using citric acid as an additive. This is shown in Figure 4.5c and Figure 4.5d where using the ratio of 200:1 Fe:CA created longer NPs (see Table 4.2). This 1-D length control with citric acid is shown in Figure 4.6 with more detail. Regrowth strategies also contribute to the quality of the 1-D hematite NPs growth (see Table 4.1). An example of this from Table 4.1 would be PA 856 where multiple temperatures (MH) were used to create large hematite seeds (Figure 4.4d). These seeds can be subsequently regrown into 1-D hematite NPs (Figure 4.2b).

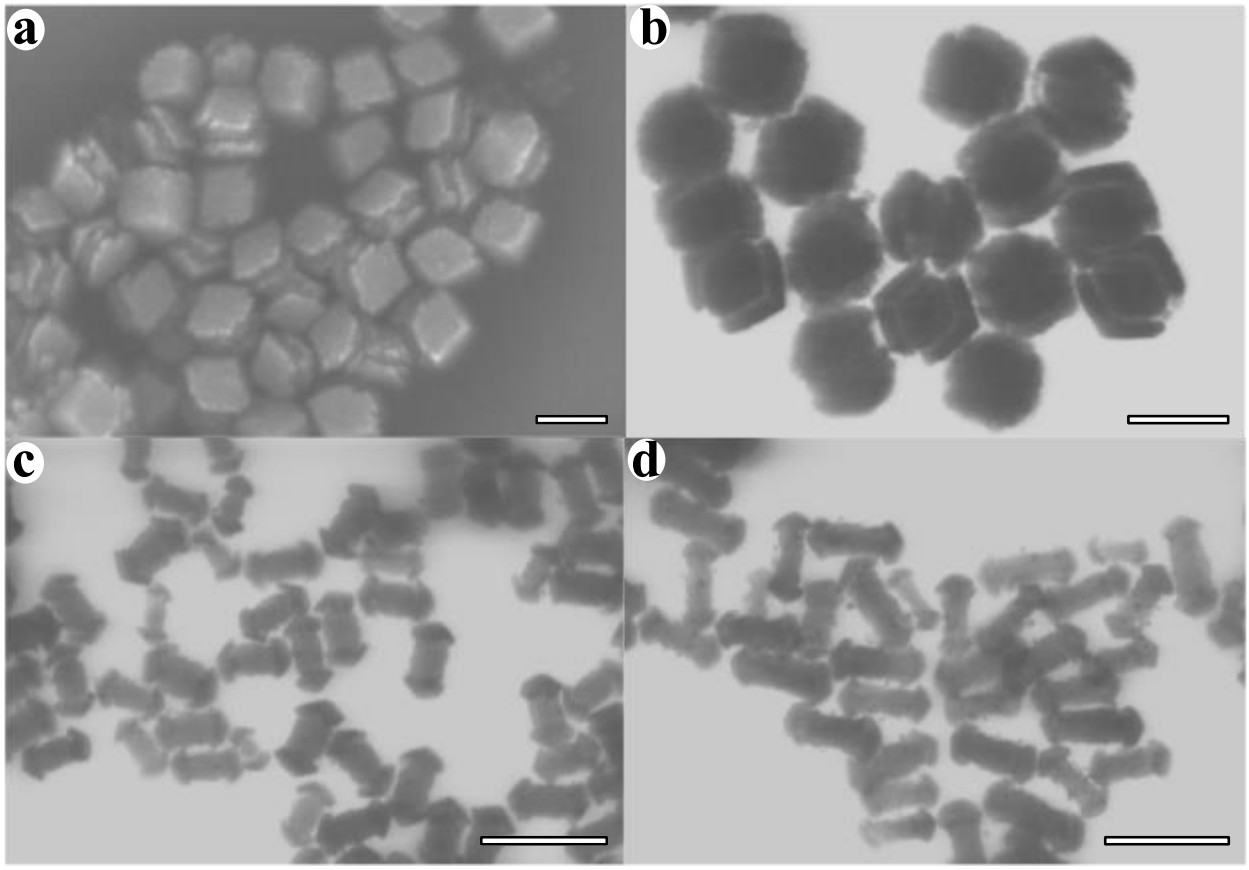

Figure 4.5. EM images showing the growth of 1-D hematite NPs. a) 2:1 R (no additives). b) 1:1 R (25:1 Fe:PVP). c) 2:1 R (400:1 Fe:CA). d) 2:1 R (200:1 Fe:CA). All scale bars are 200 nm. See Table 4.2 for more information.

Figure 4.6a illustrates 1-D hematite NPs with increasing molar ratios of iron to citric acid. Figure 4.6 shows that by increasing the molar ratio of iron to citric acid in the NP synthesis the

length of the 1-D NP structure can be extended. This trend reaches a limit at 200:1 Fe:CA producing the longest NPs in Figure 4.6e. Figure 4.6f demonstrates that increasing this amount further produces smaller NPs with a larger PDI of 0.070.

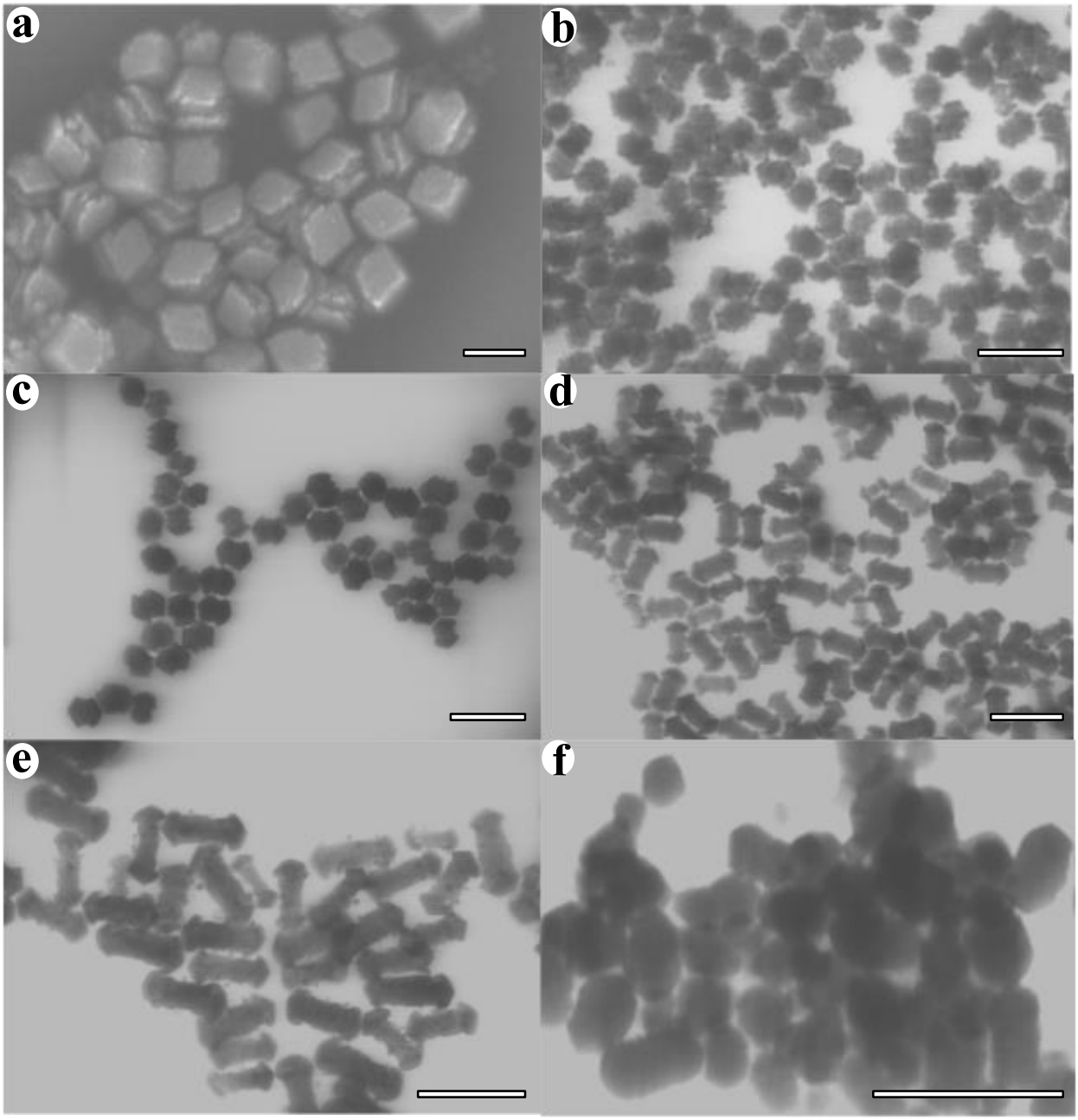

Figure 4.6. EM images of regrown 2:1 1-D hematite NPs with increasing citric acid. a) (No CA). b) (800:1 Fe:CA). c) (600:1 Fe:CA). d) (400:1 Fe:CA). e) (200:1 Fe:CA). f) (100:1 Fe:CA). All scale bars are 200 nm. See Table 4.2 for more information.

The use of PVP as an additive in the seeded regrowth creates short candy-like 1-D hematite NPs depicted in Figure 4.7. The optimal molar ratio is 10:1 Fe:PVP, resulting in an average NP size of 288 ± 9 nm and a PDI of 0.080 (Figure 4.7b). As the molar amount of PVP is decreased, the average NP size increases to 382 ± 11 but so does the NP PDI being 0.241 (Figure 4.7d).

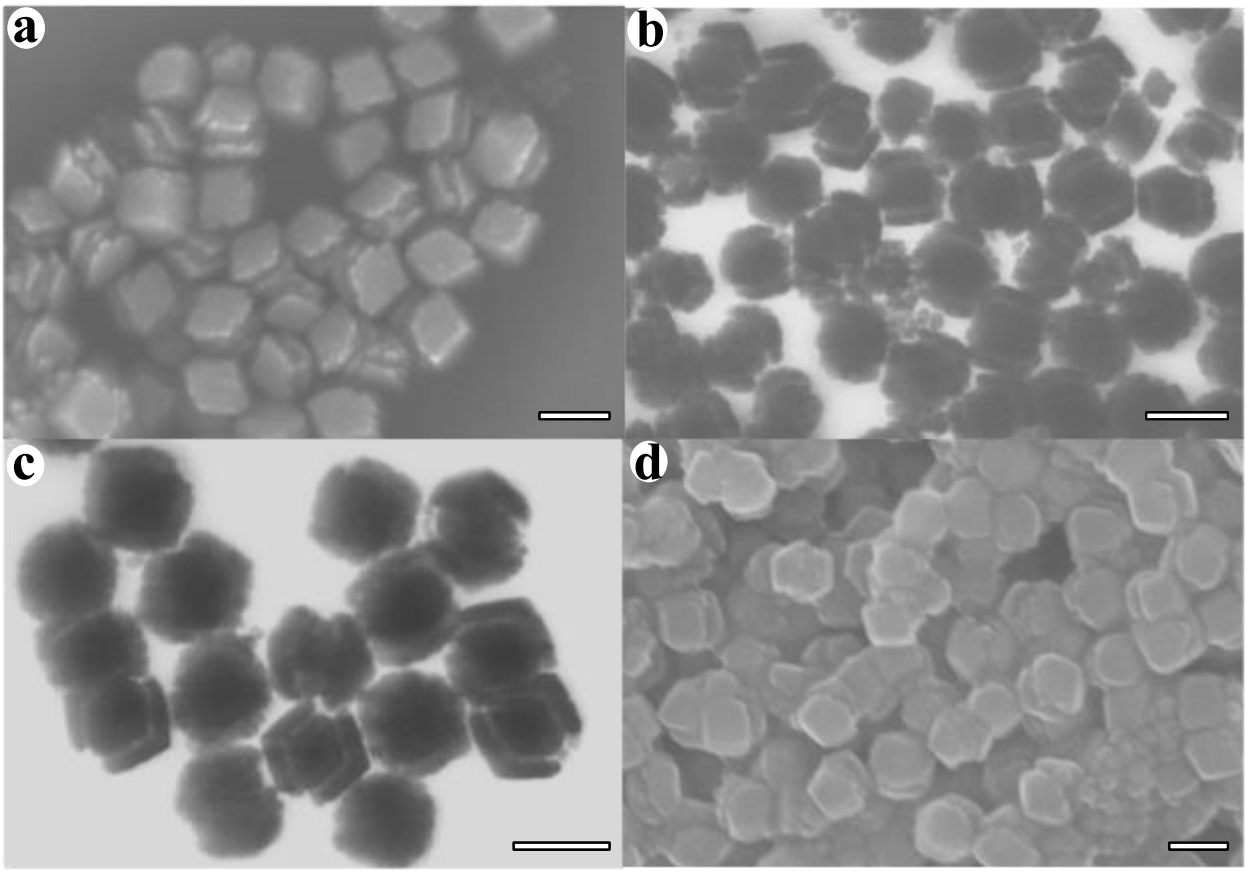

Figure 4.7. EM images of 1-D hematite NPs produced using PVP. a) 2:1 R (no additives). b) 1:1 R (10:1 Fe:PVP). c) 1:1 R (25:1 Fe:PVP). d) 1:1 R (80:1 Fe:PVP). All scale bars are 200 nm. See Table 4.2 for more information.

Figure 4.8 illustrates 1-D hematite NPs synthesised with PDDA. As the amount of PDDA is decreased from 5:1 Fe:PDDA to 40:1 Fe:PDDA the NP size increases from 529 ± 16 nm (Figure 4.8b) to 96 ± 3 nm (Figure 4.8c). The NP size of 529 ± 16 nm in Figure 4.8b is due to the aggregation of hematite NPs (PDI of 0.354). The 1-D hematite NPs made with a 20:1 Fe:PDDA molar ratio (Figure 4.8c) have a size of 96 ± 3 nm with the best PDI of 0.026. If the molar ratio

of PDDA is decreased to 40:1 Fe:PDDA the 1-D hematite NPs are slightly smaller in size (89 ± 3 nm) and are more disperse (PDI of 0.048, see Figure 4.8d).

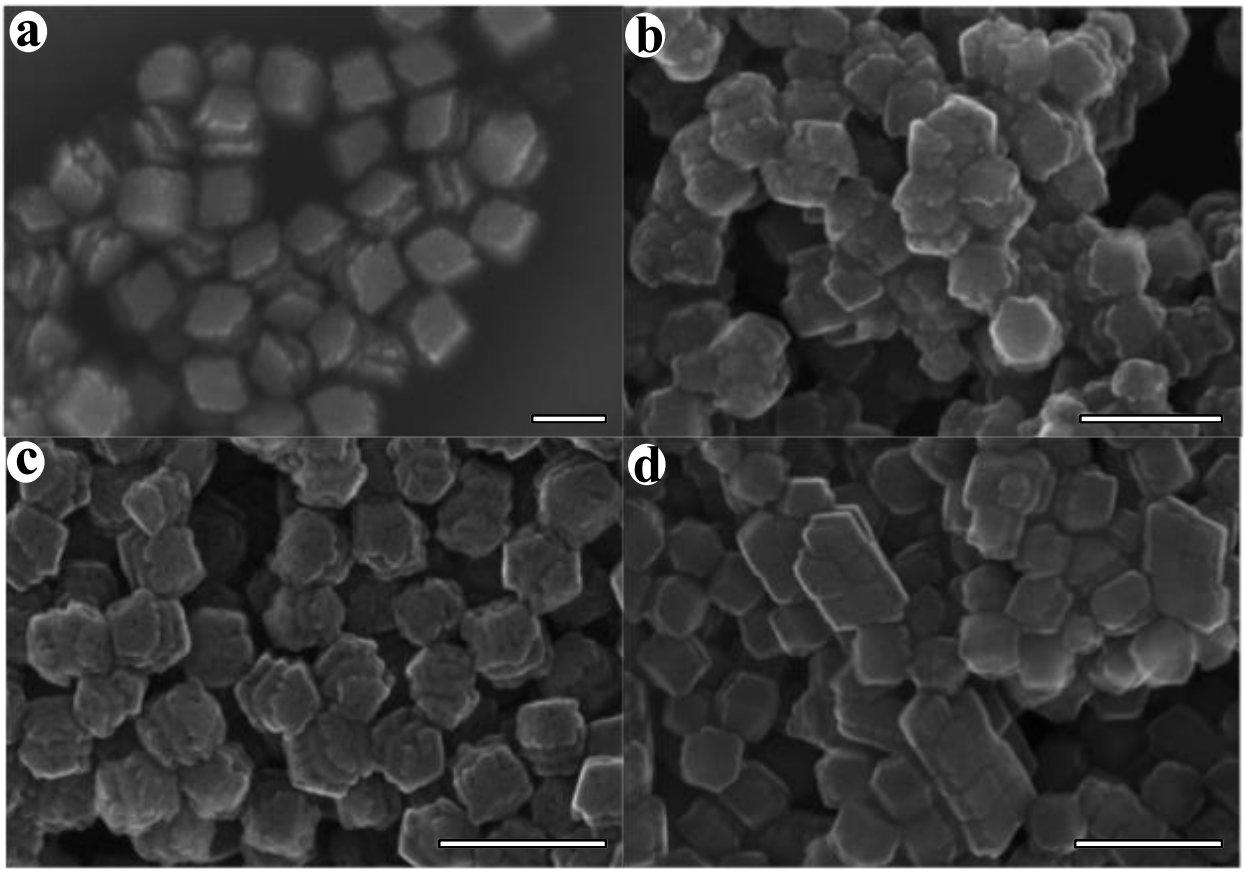

Figure 4.8. EM images showing 1-D hematite NPs made with PDDA. a) 2:1 R (no additives). b) 2:1 R (5:1 Fe:PDDA). c) 2:1 R (20:1 Fe:PDDA). d) 2:1 R (40:1 Fe:PDDA). All scale bars are 200 nm. See Table 4.2 for more information.

Figure 4.9 displays the effect of oxalic acid (OA) as an additive on the 1-D hematite NP morphology. Figure 4.9b illustrates a candy like morphology when a small amount of oxalic acid is present. Figure 4.9c and Figure 4.9d demonstrates when the amount of oxalic acid is increased the 1-D hematite morphology extends in length. This morphology resembles the longer 1-D spear like NPs with citric acid in Figure 4.6. As the amount of oxalic acid is increased from 333:1 Fe:OA to 20:1 Fe:OA the NP size increases from 92 nm to 130 nm. For the least aggregated hematite NPs, the molar ratio of 333:1 Fe:OA gave the best PDI of 0.022.

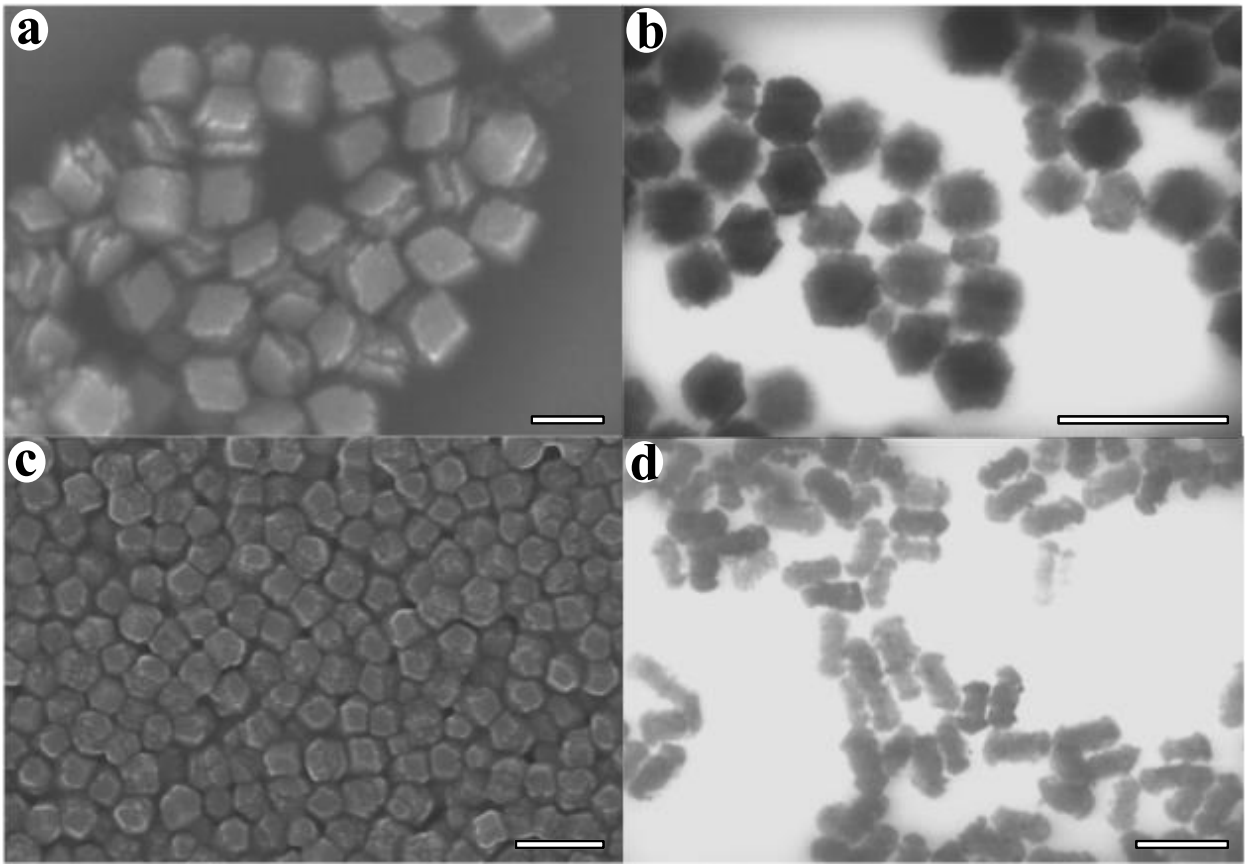

Figure 4.9. EM images showing 1-D hematite NPs made with oxalic acid (OA). a) 2:1 R (no additives). b) 2:1 R (333:1 Fe:OA). c) 2:1 R (250:1 Fe:OA). d) 2:1 R (20:1 Fe:OA). All scale bars are 200 nm. See Table 4.2 for more information.

Figure 4.10 demonstrates the effect of aspartic acid, as an additive, on the 1-D hematite NP morphology. Figure 4.10 illustrates how the 1-D hematite NPs form into a collection of spindles that resemble akageneite, when aspartic acid is used in the regrowth synthesis. As the amount of aspartic acid is decreased from 10:1 Fe:AA to 40:1 Fe:AA the hematite NP size increases from 62 nm to 107 nm. The larger hematite NPs also have a larger PDI that ranges from 0.071 to 0.196, due to the partial aggregation of the hematite NPs. The hematite NPs in Figure 4.10b have an average size of 62 nm with the best PDI of 0.071.

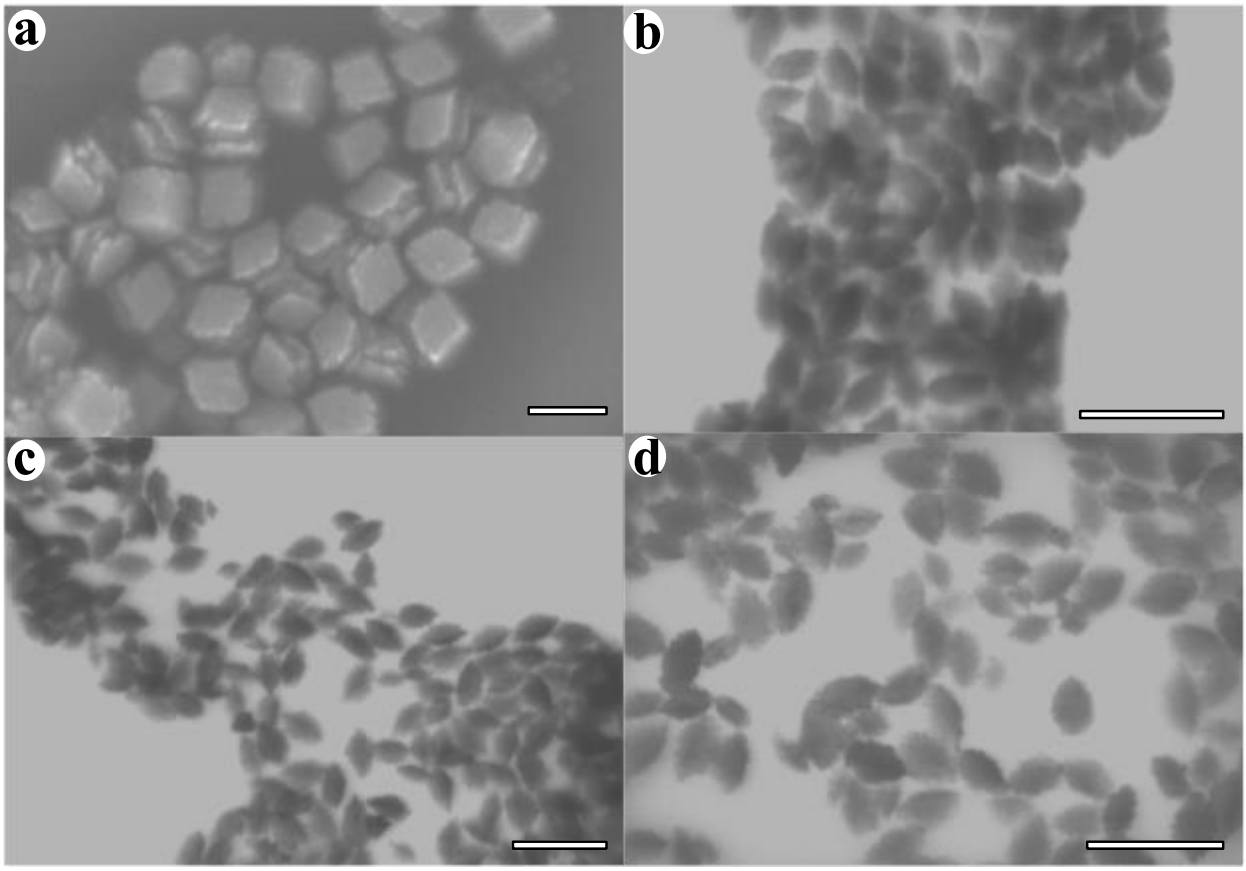

Figure 4.10. EM images showing 1-D hematite NPs made with aspartic acid (AA). a) 2:1 R (no additives). b) 2:1 R (10:1 Fe:AA). c) 2:1 R (20:1 Fe:AA). d) 2:1 R (40:1 Fe:AA). All scale bars are 200 nm. See Table 4.2 for more information.

4.4 Summary and conclusion

The goal of Chapter 4 was to investigate and improve the quality of hematite NPs. Hematite is a transition metal oxide with unique optical, catalytic and electrochemical properties that can be used for pigment and water-splitting applications. The ability to consistently produce uniform hematite NPs is the first important step in utilizing hematite's properties in real world applications.

In Chapter 4 the approach for synthesizing uniform hematite NPs was to vary reaction parameters during the NP growth. These reaction parameters included temperature, reaction time and using different additives such as PVP, PDDA and citric acid. The quality of hematite NPs was accessed using DLS and EM. This information was then used to refine next iterations of experiments thus improving the overall quality of hematite NPs.

Figure 4.1 demonstrates the different hematite nanostructures obtainable by modifying the reaction parameters discussed above. The characteristics that make each 1-D hematite nanostructure unique is their uniform length, the symmetry of the end cap morphology (see Figure 4.3) and the core or centre originating from the 1-D hematite NP seeds. Thus, Figure 4.1 illustrates that the 1-D hematite NPs can be made with varying lengths that range from 288 ± 9 nm to 91 ± 3 nm (see Figure 4.1b and Figure 4.1d), rough and crystalline NP centre's (see Figure 4.1e and Figure 4.1f) and different endcap morphologies (see Figure 4.1b and Figure 4.1d).

Figure 4.2 shows the synthetic steps for creating the different variations of the morphologies of 1-D hematite NPs. Rhombohedral hematite NPs are used as the starting seeds to create the 1-D hematite NPs. For the development of the 1-D hematite NPs specific additives that were used include citric acid, oxalic acid, PVP and PDDA. These additives help shaping the overall morphology of the 1-D hematite NPs. For example, three different types of 1-D hematite NPs can be made from the 3-D hematite seeds. These would be short 1-D hematite NPs (Figure 4.2b), long 1-D hematite NPs with a rough centre (Figure 4.2c) and long 1-D hematite NPs with a crystalline centre (Figure 4.2d). The short 1-D hematite NPs were formed with PVP as an additive, the addition resulted in rough 1-D hematite NPs, and the crystalline 1-D hematite NPs were produced using a combination of PVP, PDDA and citric acid.

These 1-D hematite NPs also have different designs of the end caps based on the NP size (Figure 4.3). The end cap formation begins with the removal of the C_3 axis corner of the rhombohedral hematite NP (Figure 4.3a). The larger end caps form along the C_3 axis corner vertex that resemble the portion removed from the rhombohedral hematite NP.

Therefore, Figure 4.2 and Figure 4.3 show the different morphologies that can be consistently obtained for the 1-D hematite NPs. This is significant because it highlights the versatility of the 1-D hematite morphology design based on the synthetic protocols developed in my work.

Figure 4.4 summarizes the main results of the synthesis of the uniform 3-D hematite NPs from amorphous iron hydroxide to rhombohedral hematite. Figure 4.4 is important because it shows each stage of the 3-D hematite NP formation. The synthesis starts with the heating of iron (III) chloride salt which transforms into oxyhydroxide NPs (see Figure 4.2 and Figure 4.4a).The subsequent heating of the oxyhydroxide NPs, transforms them into akageneite (see Figure 4.4b) which then converts into 3-D rhombohedral hematite NPs after continuous heating (see Figure 4.4c and Figure 4.4d). The synthesis of the 3-D hematite NPs is relevant because they are the seeds used in the seeded regrowth for the 1-D hematite NPs. Therefore, good quality 3-D hematite NPs are required to obtain uniform 1-D hematite NPs. Furthermore, Figure 4.4b displays akageneite as an intermediate in the formation of the 3-D hematite NPs. Akageneite has a similar 1-D profile as the 1-D C_3 axis hematite NPs suggesting that this morphology is transferred into the 1-D hematite NPs.

Figure 4.5 illustrates the four different uniform 1-D hematite morphologies that has been synthesized in this work. The first 1-D hematite morphology is demonstrated in Figure 4.5a, which is a seeded regrowth of a 3-D hematite NP without additives. The synthesis of this 1-D

hematite morphology without additives suggests that the observed C_3 axis elongation is favourable without additional help. The use of additives in the synthesis of 1-D hematite NPs helps control the length of this C_3 axis elongation. Figure 4.5b demonstrates short 1-D hematite NPs synthesized with PVP (288 $\pm$ 9 nm). Figure 4.5c and Figure 4.5d display long 1-D hematite NPs synthesized with citric acid (91 $\pm$ 3 nm for the NPs shown in Figures 4.5c,d).

Figure 4.6 illustrates the effect of citric acid with the 1-D hematite NPs. Citric acid served as a main modifying additive used to promote the 1-D growth of hematite NPs. Citric acid complexes the iron ions and extends the 3-D hematite nuclei along the C_3 axis edge creating the 1-D hematite NPs. Figure 4.6 shows that by increasing the amount of citric acid used in the 1-D hematite NPs synthesis, the 1-D hematite NPs are further elongated along the C_3 axis. Therefore, by using citric acid as an additive in the synthesis of the 1-D hematite NPs, the 1-D growth along the C_3 axis can be promoted to produce 1-D hematite NPs with different controllable lengths.

Figure 4.7 illustrates 1-D hematite NPs created from 3-D hematite seeds with PVP used as an additive. PVP serves as a shape selective ligand to produce uniform 3-D hematite NPs with larger NP size and low polydispersity. When these 3-D hematite NPs are used as seeds for the 1-D hematite NP growth, short 1-D hematite NPs are produced. This short 1-D hematite morphology is displayed in Figure 4.2b and Figure 4.7c, where the NP morphology consists of a rhombohedral hematite NP centre and hematite corner caps at the end of C_3 axis.

Figure 4.8 displays short 1-D hematite NPs synthesized using PDDA as an additive where PDDA acts as a charge stabilizer. These 1-D hematite NPs are similar in design to the 1-D hematite NPs synthesized with PVP. The difference between the 1-D hematite NPs synthesized with PDDA instead of PVP is that the hematite NPs created with PDDA are smaller in size but

have a better PDI. For example, Figure 4.8c demonstrates 1-D hematite NPs created with PDDA that have an average size of 96 ± 3 nm and a PDI of 0.026. Figure 4.7c depicts 1-D hematite NPs created with PVP that have an average size of 288 nm ± 3 and a PDI of 0.211. Therefore, PDDA can be used as additive to create short 1-D hematite NPs with smaller overall size but better PDI compared to PVP.

Figure 4.9 demonstrates the effect of oxalic acid (OA) as an additive on 1-D hematite NPs. Like citric acid, oxalic acid also produces 1-D hematite NPs along the C_3 axis. For example, Figure 4.9b depicts 1-D hematite NPs with a size of 92 ± 3 nm and a PDI of 0.022. Figure 4.9c also demonstrates 1-D hematite NPs synthesized with a size of 99 ± 3 nm and a PDI 0.063. Therefore, oxalic acid can be used as an additive to produce well-defined 1-D hematite NPs.

Figure 4.10 demonstrates the effect of aspartic acid as an additive on the 1-D hematite NP morphology. Figure 4.10b to Figure 4.10d illustrates that synthesized 1-D hematite NPs with aspartic acid have a rougher morphology than 1-D hematite NPs with no additives (see Figure 4.10a). This new morphology for the 1-D hematite NPs resembles a pseudo akageneite morphology, highlighting that this 1-D growth templates from morphological developments of precursor akageneite structures.

Figure 4.11 illustrates an idealized concept of how the 1-D hematite morphology could be applied for photochemical applications such as water splitting. The idea would be that upon the interaction with light the iridium-doped hematite centre would act as the anode, promoting the electrons to the end caps of the 1-D hematite structure. These areas would be doped with platinum NPs serving as the cathode and an intermediate to transfer electrons to proton forming hydrogen. So far in my work, only iridium oxyhydroxide has been added to 1-D hematite

morphology (see Fig. 4.11) and its location in the hematite nanocomposite has not been characterized.

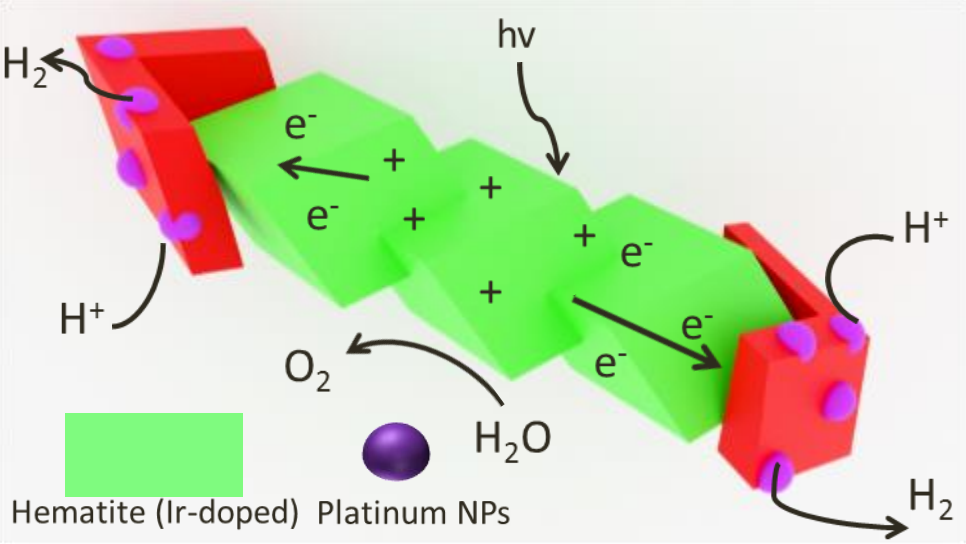

Figure 4.11. Schematic of a design of 1-D hematite NP doped with iridium oxyhydroxide and platinum NPs for water splitting.

Therefore, the most important result of Chapter 4 was the development of a unique 1-D hematite morphology with controllable lengths (see Figure 4.2 and Figure 4.11). These findings add to the existing literature by demonstrating the creation of new 1-D hematite NP morphologies that could be utilized in photoelectrochemical applications.

The research described in this chapter demonstrates that new 1-D hematite morphologies were synthesized with controlled size and dispersity. This was accomplished by synthesizing uniform rhombohedral hematite NPs using different heating regimes and additives. These rhombohedral hematite NPs were then used as hematite seeds to form the new 1-D hematite morphologies. This includes the "candy and spear" like 1-D hematite regrown NPs, grown along the C_3 axis. The 1-D hematite morphology were synthesized using a variety of additives and

heating regimes. The resulting 1-D hematite NPs can be made with unique structural centres at controllable lengths depending on the additives used. Citric acid has the most effect on controlling the length of the hematite NPs. The 1-D hematite morphology called "spears" length can be controlled by modifying the amount of citric acid used in seed synthesis. This 1-D morphology was doped with $IrCl_3$ with the intent to create a photochemical cell.[1.23,1.26,4.17] The idea is that upon interaction with light, a single 1-D hematite NP would act as an anode and cathode. This photochemical cell could be then used for water splitting applications.[1.23,1.26,4.17]

Therefore Chapter 4 discussed the synthesis of uniform 3-D and 1-D hematite NP morphologies using a variety of additives. The unique 1-D hematite NPs can be used as a photoelectrochemical cell (PEC) in water splitting applications.

Acknowledgments

Thanks to Jason Mercer with general Blender help and the construction of the hematite 1-D NP representation in Figure 4.2c.

4.5 References

[4.1]Goia, D. V.; Matijević. *New J. Chem.* **1998**, *22*, 1203–1215.

[4.2]Sivula, K. *The Journal of Physical Chemistry Letters* **2013**, *4*, 1624–1633.

[4.3]Wang, J.; White, W. B.; Adair, J. H. *J. Am. Ceram. Soc.* **2005**, *88*, 3449–3454.

[4.4]Shindo, D.; Park, G.-S.; Waseda, Y.; Sugimoto, T. *Journal of Colloid and Interface Science* **1994**, *168*, 478–484.

[4.5]Wheeler, D.; Wang, G.; Ling, Y.; Zhang, J. Z. *Energy & Environmental Science* **2012,** *5*, 6682-6702.

[4.6]Matijević, E. *Colloid J.* **2007**, *69*, 29–38.

[4.7]Yablonovitch, E. *Phys. Rev. Lett.* **1987**, *58*, 2059–2062.

[4.8]Kim, J.; Jang, J. *Journal of Materials Chemistry A: Materials for Energy and Sustainability* **2014**, *2*, 17249-17252.

[4.9]Wang, L.; Lee, C.Y.; Kirchgeorg, R., Liu, N.; Lee, K.; Kment, S.; Schmuki, P. *Research on Chemical Intermediates* **2015**, *41*, 9333-9341.

[4.10]Riha, S. C.; Klahr, B. M.; Tyo, E. C.; Seifert, S.; Vajda, S.; Pellin, M. J.; Hamann, T. W.; Martinson, A. B. F. *ACS Nano* **2013**, *7*, 2396–2405.

[4.11]Dotan, H.; Kfir, O.; Sharlin, E.; Blank, O.; Gross, M.; Dumchin, I.; Ankonina, G.; Rothschild, A. *Nat. Mater.* **2013**, *12*, 158–164.

[4.12]Wang, S.; Gao, B.; Zimmerman, A. R.; Li, Y.; Ma, L.; Harris, W. G.; Migliaccio, K.W. *Bioresour. Technol.* **2015**, *175*, 391-395.

[4.13]MacHala, L.; Tuček, J.; Zbořil, R. *Chemistry of Materials* **2011**, *23*, 3255–3272.

[4.14]Jubb, A. M.; Allen, H. C. *ACS Appl. Mater. Interfaces.* **2010**, *2*, 2804–2812.

[4.15]Yang, Y.; Ma, H.; Zhuang, J.; Wang, X. *Inorg. Chem.* **2011**, *50*, 10143–10151.

[4.16]Zhang, T.; Dong, W.; Keeter-Brewer, M.; Konar, S.; Njabon, R. N.; Tian, Z. R. *J. Am. Chem. Soc.* **2006**, *128*, 10960–10968.

[4.17]Yu, S.; Hong Ng, V. M.; Wang, F.; Xiao, Z.; Li, C.; Kong, L. B.; Que, W.; Zhou, K. *J. Mater. Chem. A* **2018**, *6*, 9332–9367.

Chapter 5: The synthesis and characterization of pigments based on hematite and other iron oxide nanoparticles

5.1 Introduction

Throughout human history colours have provided critical functions in both recognition and communication from the animate and inanimate worlds.[5.1] Some examples of inanimate objects of colour would include photonic crystals and inorganic pigments. Photonic crystals are materials that interact with electromagnetic radiation through a periodic spatial modulation in their refraction.[5.2] This interaction allows the photonic crystals to selectively absorb light in any part of the visible or invisible spectrum.[5.3] Specifically, photonic crystals produce colours due to their periodicity in their structure where their length is proportional to the visible wavelengths.[5.1] Photonic crystals have promising applications including the use in sunscreens, paints, security devices and sensors.[5.4]

Inorganic pigments are known in a natural or synthetic form where the synthetic form has some advantages over natural pigments.[5.5] Examples of these natural pigments would be red ochre, yellow ochre and venetian red. Synthetic inorganic pigments are produced industrially with enhanced and improved properties such as colour uniformity.[5.5] This results in increased chemical and physical stability of the powder coating allowing for better application control.[5.5,5.6] Among these synthetic pigments iron oxide is the most commonly used due to its excellent tinting strength and weather resistance.[1.17,4.3,5.5] The colour for iron oxides is the result of oxygen-to-metal charge transfer, superposed crystal-field bands and inter-valence charge transfer occurring between neighboring iron (II) atoms and iron (III) atoms.[5.7]

Iron oxide displays of colour have been used historically for the decoration of Japanese ceramics called akae.[5.8-5.10] The specific polymorph of iron oxide used in akae is called hematite. Hematite is used in red pigment development for its tunable colour.[5.8] The colour of the pigment depends on hematite particles size, the dispersion of hematite particles and the thickness of the glass layer where the red colour of the hematite particles is the most vibrant when the particles are small and well dispersed.[5.8] Current iron oxide pigments used in industry are the synthetic Pigment Red 101 and the natural Pigment Red 102.[1.17] Additional colours of iron oxide pigments that have been synthesized using citrus pectin are IOP-II_{300} yellow, IOP-II_{600} (red) , IOP-II_{1000} (purple); while iron (III) sulfate produced IOP-III_{300} (yellow), IOP-III_{600} (red) and IOP-III_{1000} (violet).[1.17] These different colours of synthetic hematite pigments are obtained via calcination at temperatures of 300^{o}C, 600^{o}C and 1000^{o}C.[1.18]

In Chapter 4 the synthesis of hematite pigments and films by using the well-defined hematite NPs was discussed. These hematite films display a full range of colours when observed via the transmission and reflection of light. A full spectrum of colours is obtained due to the structural order of the hematite NPs in the film. This structural order is achieved by the ability to control the size of hematite NPs that comprise/constitute the film. The size of the hematite NPs that can be synthesized ranges from 50 nm to 500 nm where the hematite films upon the interaction of light have a wavelength range from 465 nm to 650 nm. Colourful hematite films are obtained by further changing the hematite NP morphology or ordering arrangements. For example, a unique reflective red film is obtained by the aggregation of smaller hematite NPs into larger hematite aggregates (see Figure 5.1 and Figure 5.2). Changing the morphology from 3-D to 1-D hematite growths creates a multi-coloured pigment films.

5.2 Synthesis of hematite thin films

Reagents

Premade hematite NPs as described in Chapter 4 and high-purity deionized water (>18.4 M Ω cm), produced using Millipore A10 Milli-Q. Hematite NPs were deposited on a microscope slide to dry by evaporation while covered with a Petri dish.

Procedure

500 μL of desired hematite sample is centrifuged three times. After each centrifugation supernatant is removed and pellet is re-dispersed with high-purity deionized water. After the third centrifugation, the supernatant is removed leaving the condensed hematite pellet. 100 μL of high-purity deionized water is then added to the pellet which is re-dispersed. Then ca. 20 μL of this hematite dispersion is deposited on a glass slide and left to dry, forming an approximate area of 10 cm^2.

Instrumentation

UV-vis spectra were recorded using an Ocean Optics QE65000 fiber-optic UV-vis spectrometer. Electron microscopy (EM) imaging was performed with a Hitachi S-5200 using a copper grid with a formvar/carbon film (FCF-200 Electron Microscopy Science). Hematite NPs were heated in a Heidolph MR 3004 Safety heat block, Accublock digital dry bath heat block and IKA C-mag HS7 heat block. Hematite NPs were centrifuged using both a Thermo scientific Legend Micro 21 centrifuge and Medifuge centrifuge.

5.3 Results

The full colour palette obtainable from synthesized hematite films is displayed in Figure 5.1. These hematite films were synthesized by using well-defined, uniform hematite NPs of varying sizes and morphologies. The colours displayed by these hematite films are a combination

of reflection and transmission of light on the surface of the film. The size of the hematite NPs is an important factor in determining the colour that the film exhibits. Hematite films with sizes of hematite NPs from 130 nm to 300 nm are shown in Figure 5.1a to Figure 5.1d. This change in hematite NP size corresponds with the change in colour in the hematite films, i.e. yellow to red. The arrangement of the hematite NPs also determines what colour is observed when the films are exposed to light. For example, a unique shiny red colour is obtained via the reflection of light (see Figure 5.1e). This unique colour comes from the aggregation of smaller hematite NPs into large assemblies (see Figure 5.3a). Hematite films that exhibit green to blue colours upon light reflection are shown in Figure 5.1f to Figure 5.1h. A hematite film prepared with 1-D hematite NPs instead of 3-D hematite NPs is illustrated in Figure 5.1l. This hematite film exhibits a multitude of colours upon the reflection of light.

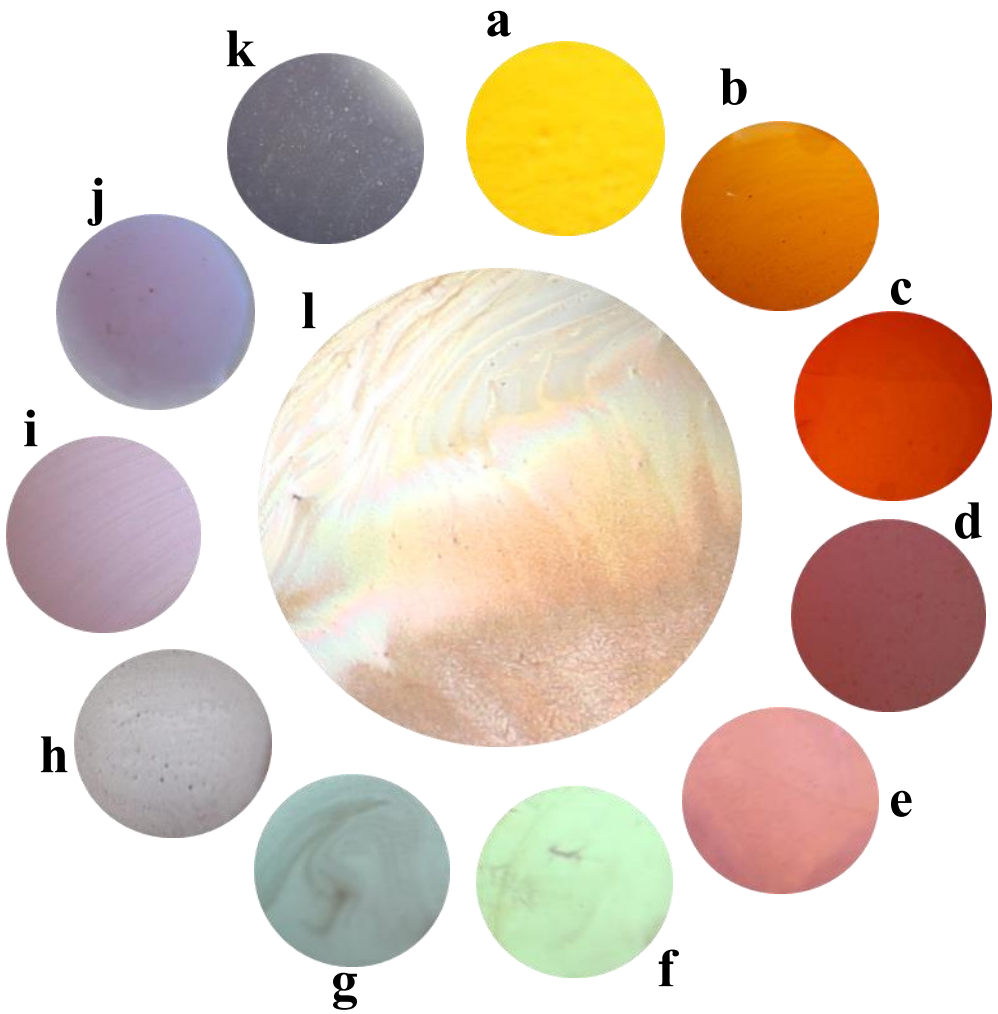

Figure 5.1. Optical photographs of hematite films. All colours from the hematite films are obtained from reflection and transmission of light. a) Transmission of yellow colour. b) Transmission of orange colour. c) Transmission of red colour. d) Transmission of dark red colour. e) Reflection of shiny red colour. f) Reflection of green colour. g) Reflection of teal colour. h) Reflection of blue colour. i) Transmission of purple colour. j) Reflection of dark purple colour. k) Reflection of dark blue. l) Reflection of multiple colours. See Table 5.1 for more information.

Table 5.1: Summary of the prepared thin hematite films

Figure Names	Sample	Description	DLS Z-avg (nm)
Fig. 5.1a	PF 121	S (20 mM HCl, 5:1 Fe:PVP)	132 ± 4
Fig. 5.1b	PA 995	S MH (50:1 Fe:PVP 1300k)	187 ± 6
Fig. 5.1c	PF 522	S MH (100:1 Fe:PVP, 35:1 Fe:PDDA)	143 ± 4
Fig. 5.1d	PF 496	S (40 mM HCl, 0.5% OA)	322 ± 32
Fig. 5.1e	PF 515	S MH (50:1 Fe:PVP, 35:1 Fe:PDDA)	178 ± 5
Fig. 5.1f	PA 842	S MH (100:1 Fe:PVP)	296 ± 9
Fig. 5.1g	PA 995	S MH (50:1 Fe:PVP 1300k)	187 ± 6
Fig. 5.1h	PF 529	S (50:1 Fe:PVP, 35:1 Fe:PDDA, 40 mM HCl, 100% aluminum nitrate)	373 ± 37
Fig. 5.1i	PA 842	S MH (100:1 Fe:PVP)	296 ± 9
Fig. 5.1j	PF 529	S (50:1 Fe:PVP, 35:1 Fe:PDDA, 40 mM HCl, 100% aluminum nitrate)	373 ± 37
Fig. 5.1k	PE 721	2.5 mM iron chloride @ 95 degrees for 6 days.	46 ± 1
Fig. 5.1l	PF 451	2:1 R (50:1 Fe:PVP, 30:1 Fe:PDDA)	109 ± 3
Fig. 5.2a	PF 121	S (20 mM HCl, 5:1 Fe:PVP)	132 ± 4
Fig. 5.2b	PA 995	S MH (50:1 Fe:PVP 1300k)	187 ± 6

Fig. 5.2c	PF 522	S MH (100:1 Fe:PVP, 35:1 Fe:PDDA)	143 ± 4
Fig. 5.2d	PF 496	S (40 mM HCl, 0.5% OA)	322 ± 32
Fig. 5.3a	PF 515	S MH (50:1 Fe:PVP, 35:1 Fe:PDDA)	178 ± 5
Fig. 5.3b	PA 842	S MH (100:1 Fe:PVP)	296 ± 9
Fig. 5.3c	PA 995	S MH (50:1 Fe:PVP 1300k)	187 ± 6
Fig. 5.3d	PF 529	S (50:1 Fe:PVP, 35:1 Fe:PDDA, 40 mM HCl, 100% aluminum nitrate)	373 ± 37
Fig. 5.4a	PA 842	S MH (100:1 Fe:PVP)	296 ± 9
Fig. 5.4b	PF 529	S (50:1 Fe:PVP, 35:1 Fe:PDDA, 40 mM HCl, 100% aluminum nitrate)	373 ± 37
Fig. 5.4c	PE 721	2.5 mM iron chloride @ 95 degrees for 6 days.	46 ± 1
Fig. 5.4d	PF 451	2:1 R (50:1 Fe:PVP, 30:1 Fe:PDDA)	Length 109 ± 3 Width 80 ± 2
Fig. 5.5a	PA 995	S MH (50:1 Fe:PVP 1300k)	187 ± 6
Fig. 5.5b	PA 842	S MH (100:1 Fe:PVP)	296 ± 9
Fig. 5.5c	PF 496	S (40 mM HCl, 0.5% OA)	322 ± 32
Fig. 5.5d	PA 842	S MH (100:1 Fe:PVP)	296 ± 9
Fig. 5.5e	PF 535	S (40 mM HCl, 0.1% OA)	324 ± 10

Fig. 5.6a	PE 721	2.5 mM iron chloride @ 95 degrees for 6 days.	46 ± 1
Fig. 5.6b	PF 451	2:1 R (50:1 Fe:PVP, 30:1 Fe:PDDA)	109 ± 3
Fig. 5.6c	PF 522	S MH (100:1 Fe:PVP, 35:1 Fe:PDDA)	143 ± 4
Fig. 5.6d	PF 526	S (50:1 Fe:PVP, 35:1 Fe:PDDA, 100% aluminum nitrate)	147 ± 4
Fig. 5.6e	PF 537	S (40 mM HCl, 0.5% oxalic acid)	320 ± 10

EM images of the hematite NPs used for creating the films (Figure 5.1) are demonstrated in Figure 5.2. The change in the hematite NP size varies the colour obtained from the hematite films ranges from yellow to dark red. The unique dark red film displayed in Figure 5.1d is the result of the hematite NPs aggregation (Figure 5.2d). The aggregate hematite NP size obtained via DLS is 322 ± 32 nm.

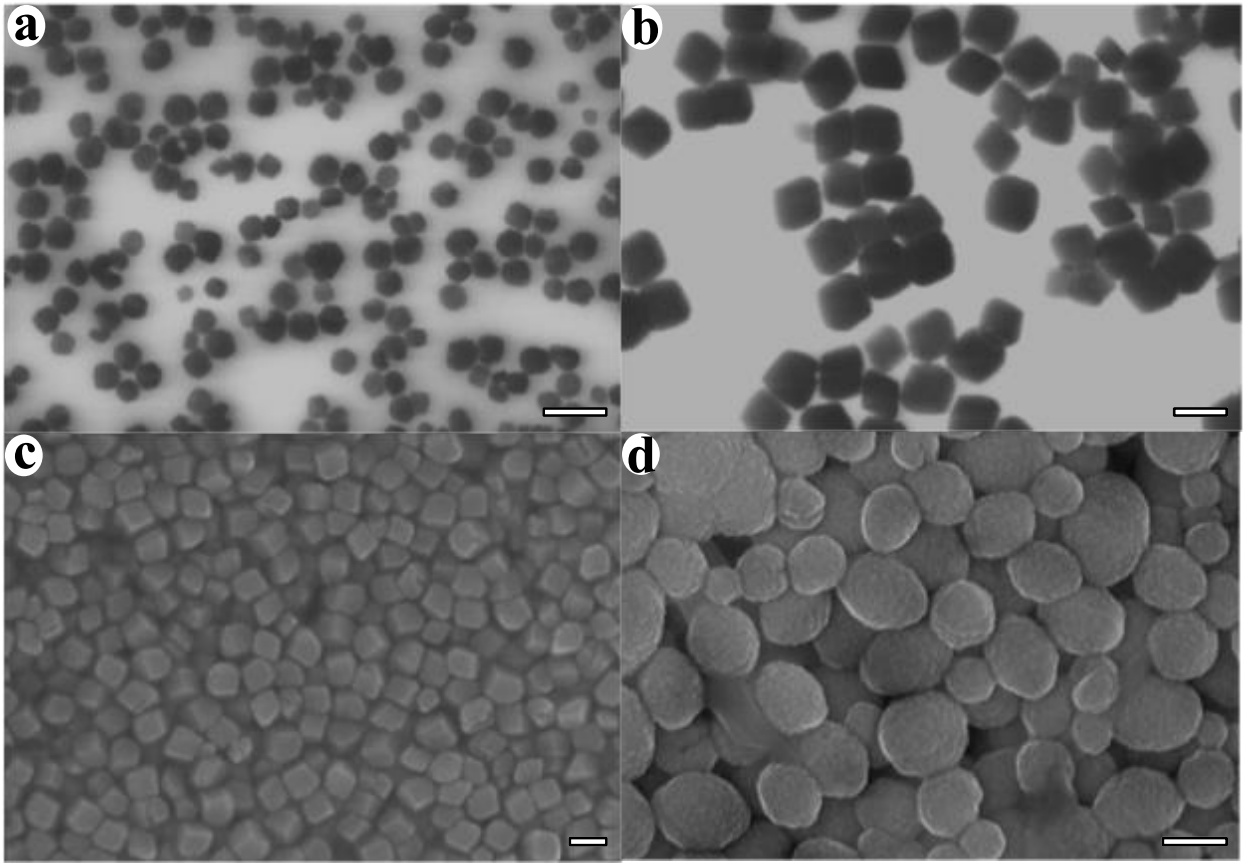

Figure 5.2. SEM images of hematite NPs present from the films shown in Figure 5.1. a) Yellow film from Figure 5.1a. b) Orange film from Figure 5.1b. c) Red film from Figure 5.1c. d) Dark red film from Figure 5.1d. All scale bars are 200 nm. See Table 5.1 for more information.

EM images of hematite NPs that were used to create the hematite films exhibiting colours from red to purple are demonstrated in Figure 5.3. For the green film the hematite NPs aggregate together, resulting in an aggregate NP size of 178 ± 5 nm (Figure 5.3a). For the blue/purple film the hematite NPs aggregate together, resulting in an aggregate NP size of 373 ± 37 nm (see Figure 5.3d).

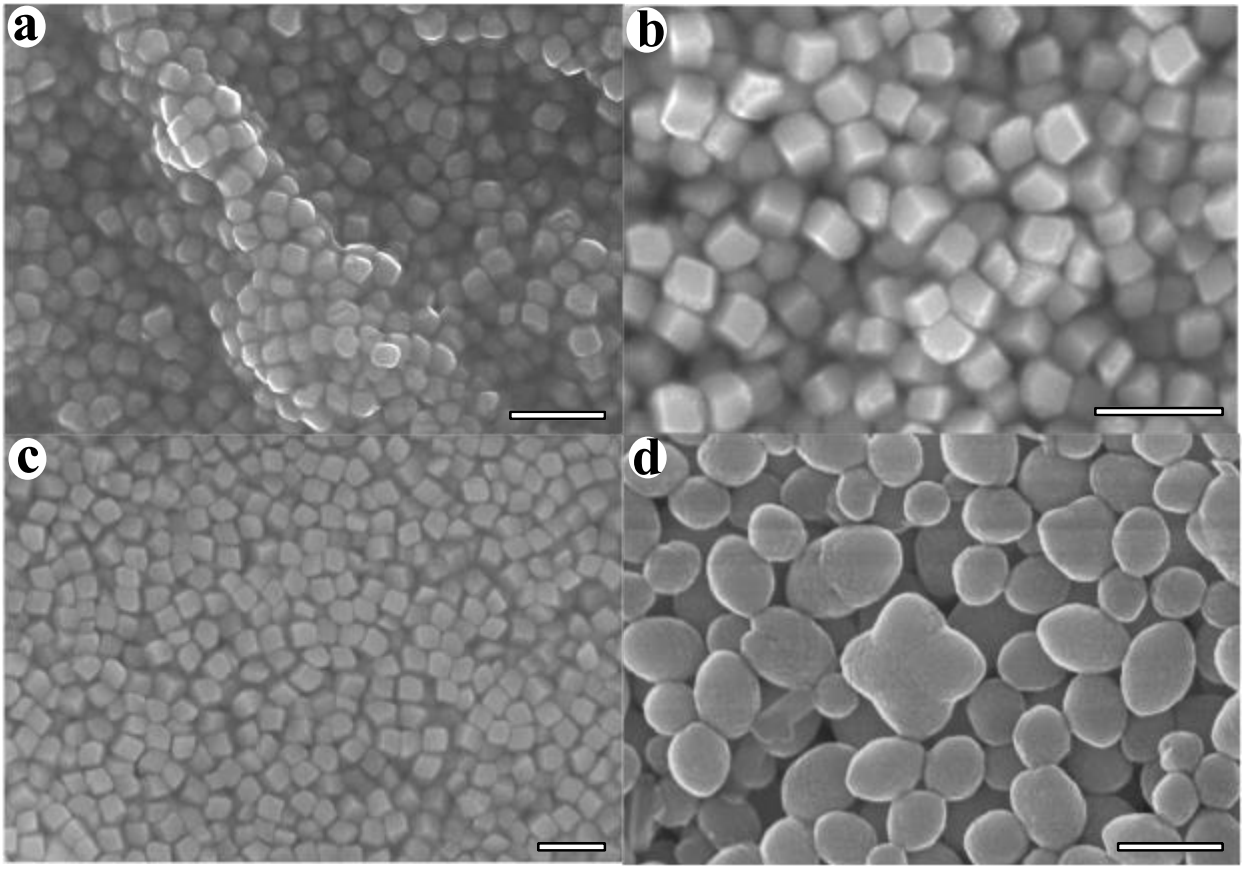

Figure 5.3. EM images hematite NPs present from the films shown in Figure 5.1. a) Shiny red film from Figure 5.1e. b) Green film from Figure 5.1f. c) Teal film from Figure 5.1g. d) Blue/purple film from Figure 5.1h. All scale bars are 500 nm. See Table 5.1 for more information.

SEM images of the hematite NPs used to create the dark purple and blue hematite films colours are illustrated in Figure 5.4. The multi-colored hematite film, shown in Figure 5.1l, was created using 1-D hematite NPs displayed in Figure 5.4d. The 1-D hematite NPs that created this film have a size of 109 $\pm$ 3 nm in length and 80 $\pm$ 2 nm in width.

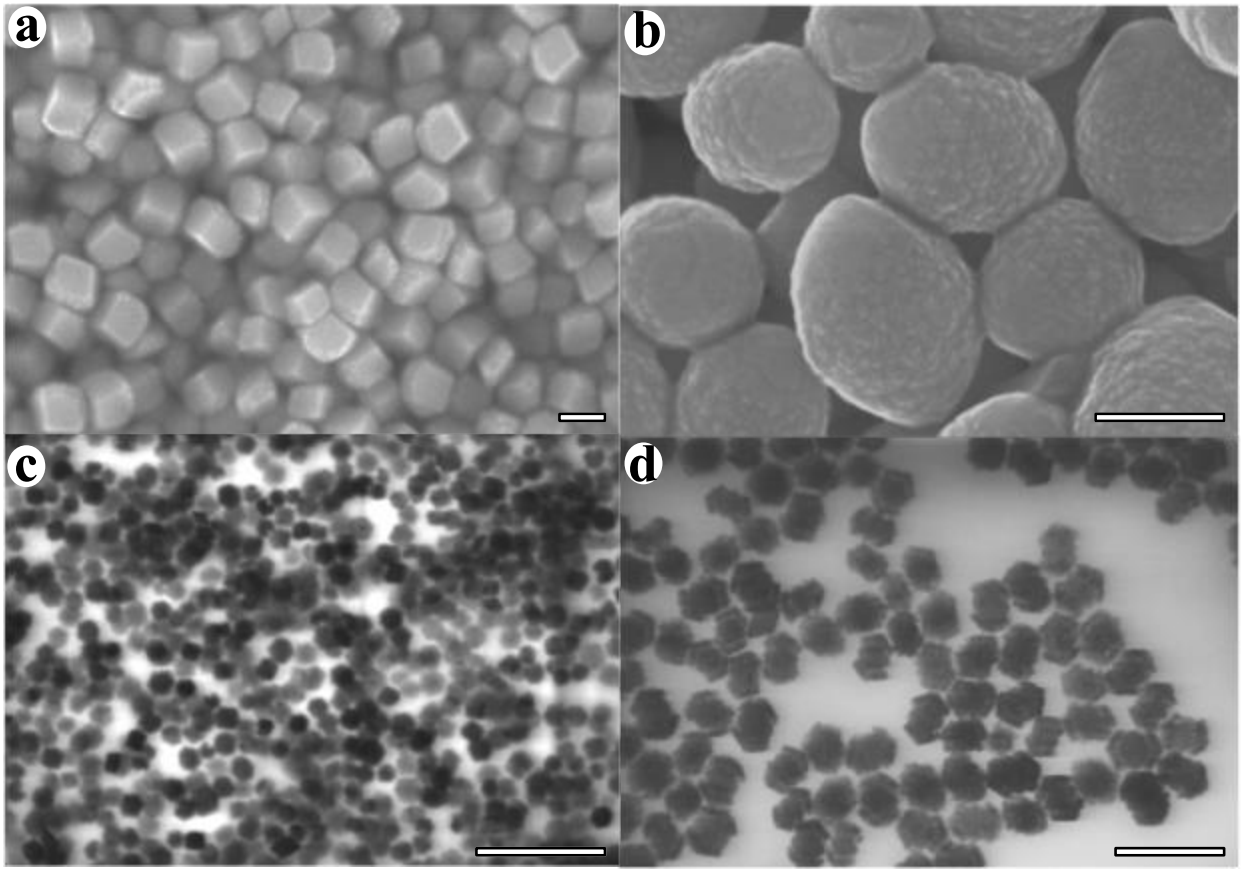

Figure 5.4. SEM images hematite NPs present from the films shown in Figure 5.1. a) Purple film from Figure 5.1i. b) Dark purple film from Figure 5.1j. c) Dark blue film from Figure 5.1k. d) Rainbow film from Figure 5.1l. All scale bars are 200 nm. See Table 5.1 for more information.

The spectral range for the hematite films obtained via the transmission and reflection of light is exhibited in Figure 5.5. Figure 5.5a, Figure 5.5c and Figure 5.5e exhibit optical photos of the transmission of light through the hematite thin films. Figure 5.5b and Figure 5.5d illustrate optical photos of the reflection of light on the hematite thin films. The spectral range of the hematite films ranged from 465 nm to 810 nm is illustrated in Figure 5.5. The UV-vis spectra of the hematite films measured show the diverse colours obtained from the interaction with light. These colours are teal, green, red, purple and blue.

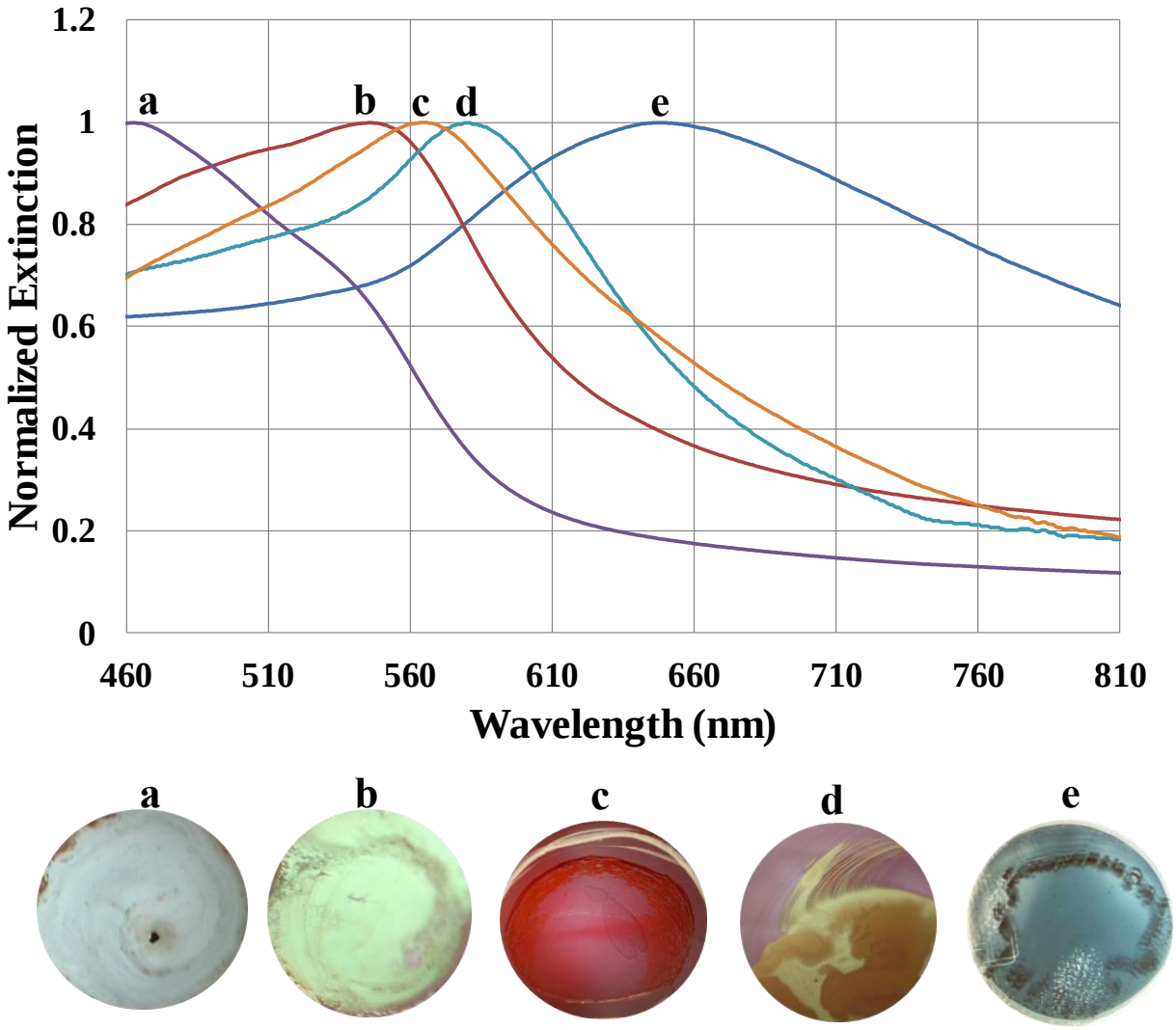

Figure 5.5. UV-vis spectra of the transmission and reflection of unique hematite films. a) Teal film with the maxima of 465 nm. b) Green film with the maxima of 545 nm. c) Red/purple film with the maxima of 565 nm. d) Purple film with the maxima of 580 nm. e) Blue film with the maxima of 650 nm. See Table 5.1 for more information.

The spectral range and optical photographs of hematite films of increasing NP size is demonstrated in Figure 5.6. The hematite NP size increases from 50 nm to 300 nm with the resulting films displayed from Figure 5.6a to Figure 5.6e. As the hematite NP size increases, the optical photos of the hematite films show a change in colour from yellow (Figure 5.6a) to red (Figure 5.6c) to reddish blue (Figure 5.6e).

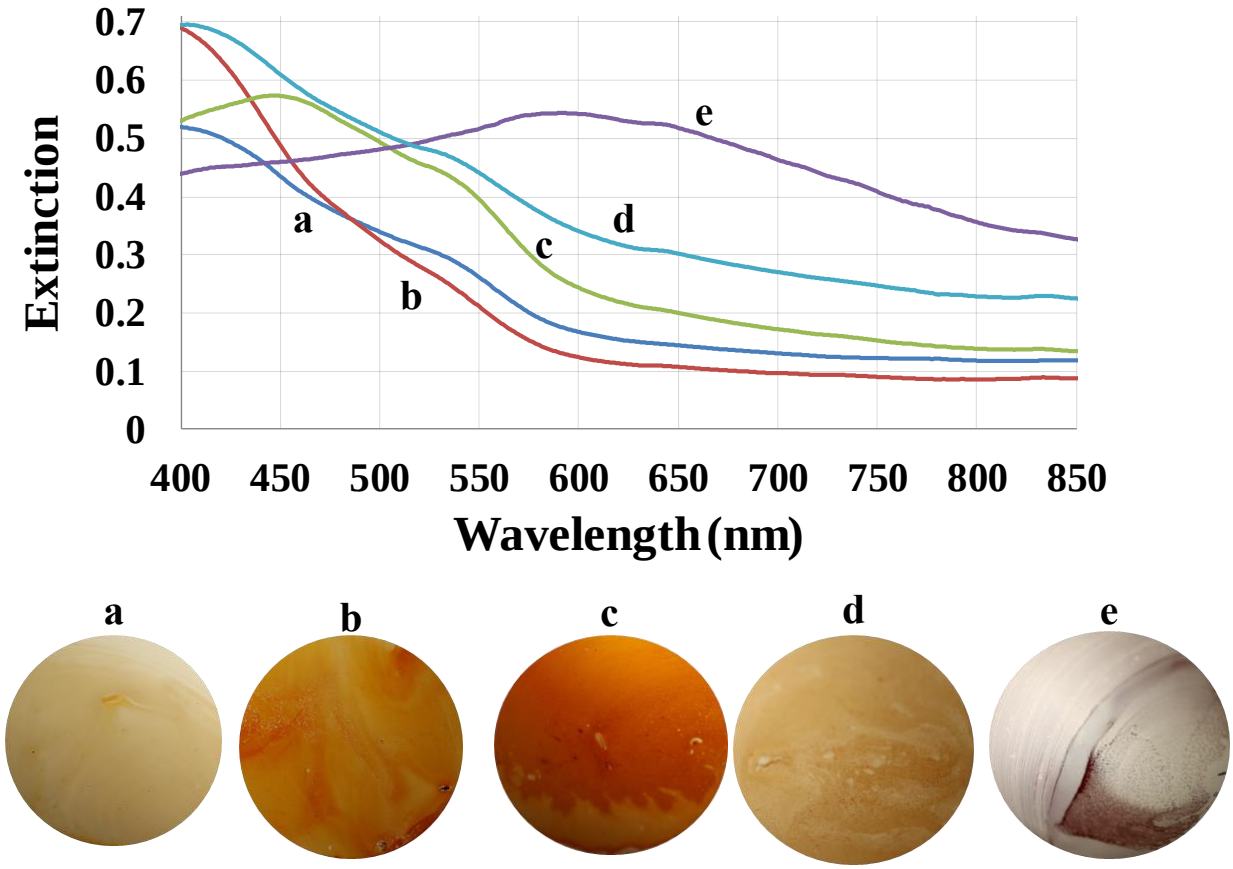

Figure 5.6. UV-vis spectra displaying the transmission and reflection of hematite films with increasing size. a) 50 nm. b) 100 nm. c) 150 nm. d) 200 nm. e) 300 nm. See Table 5.1 for more information.

5.4 Discussion

The goal of Chapter 5 was to investigate the optical properties of the 3-D hematite NPs when arranged into thin films. In Chapter 5, 3-D hematite NPs of various morphologies were created into thin films, where structural colours were investigated both in transmission and reflection. These hematite thin films are significant because they could be used in the preparation of chemically stable colourful pigments.

Figure 5.1 illustrates a colour wheel of hematite thin films created using uniform 3-D hematite NPs of different sizes. These hematite NPs were then spread into thin films, where via

the transmission and reflection of light produced the colours shown in Figure 5.1. The colours obtained span the visible spectrum. Figure 5.1a to Figure 5.1d demonstrate hematite films that through the transmission of light, yellow to red colours are displayed. The size of the hematite NPs used to create these films range from 132 ± 4 nm to 322 ± 32 nm (see Table 5.1). Figure 5.1e to Figure 5.1h illustrates hematite films that through the reflection of light, red to blue colours are produced. The size of the hematite NPs used to create these films range from 178 ± 5 nm to 373 ± 37 nm (see Table 5.1). Figure 5.1i to Figure 5.1l shows hematite films that through the refection and transmission of light purple to a multi coloured film are demonstrated. The size of the hematite NPs used to create these films range from 296 ± 9 nm to 109 ± 3 nm (see Table 5.1). Figure 5.1l represents a hematite thin film created from 1-D hematite NPs.

Figure 5.2 shows EM images of the hematite NPs used for creating the yellow to dark red hematite thin films demonstrated in Figure 5.1a to Figure 5.1d. This change in colour originates from the structural order of the hematite NPs in the film. This structural order is achieved by the ability to control the size of hematite NPs that comprise/constitute the film. The uniformity of the hematite NPs in size and shape creates well dispersed layers of hematite NPs in the hematite thin films. Through the interaction of light on these well dispersed layers the hematite film's structural colour is produced, which is dependent on the size, shape and arrangement of the hematite NPs used.

The change in hematite NP morphology by aggregation is demonstrated in Figure 5.3. Figure 5.3 displays EM images of hematite NPs used to create the hematite films exhibiting colours ranging from red to purple. The collection of smaller hematite NPs into larger hematite groups affects the colour by changing the overall NP size. When the average size of the hematite NPs used to create a thin film is increased, the structural order of the bigger hematite NPs is

different than typical hematite NPs. Figure 5.3a and Figure 5.3d depict this change in hematite NP size. The hematite NPs demonstrated in Figure 5.3a have a size of 178 ± 5 nm where the hematite NPs illustrated in Figure 5.3d have a size of 373 ± 37 nm. Thus, from the change of hematite NP size in these films, the resulting colours from change from "shiny" red to a bluish purple. These colours were observed via the reflection of light upon large hematite NPs.

Figure 5.4 illustrates hematite NPs used to produce thin films with colours from purple to dark blue. These colours were observed via the transmission and reflection of light upon large aggregated hematite NPs. The hematite NPs in Figure 5.4a have an average size of 296 ± 9 nm, resulting in a purple film. The hematite NPs in Figure 5.4b have an average size of 373 ± 37 nm, resulting in a dark purple film. Figure 5.4d shows 1-D hematite NPs that were used to create the multi- colored thin film in Figure 5.1l. The 1-D hematite NPs in Figure 5.4d produce a variety of colours in Figure 5.1l due to a different hematite morphology and dispersion when a thin film is created.

Figure 5.5 shows the spectral range for the hematite films obtained via the transmission and reflection of light. Figure 5.5 is important because it shows that the hematite films can be created to span a spectral range of 465 nm to 650 nm. This large array of colours demonstrated in these thin hematite films are due to structural colours created upon uniform hematite NPs arrangement. Thus, Figure 5.5 is also further evidence that the 3-D hematite NPs synthesized for the preparation of the hematite thin films are relatively uniform in size and morphology.

Figure 5.6 shows the spectral range and optical photographs of hematite films of increasing hematite NP size. Figure 5.6 is important because it relates the hematite NP size to the resulting wavelength/colour displayed by the hematite thin film. Figure 5.6e shows a broad

response across the visible region, highlighting that the larger hematite NPs of ca. 300 nm in diameter can produce the largest range of colours when arranged into thin films.

Therefore, by using a variety of hematite NPs to create hematite thin films a rainbow of structural colours was obtained. Future directions for these films would be to incorporate them in the decoration of pottery and improve chemical stability of the hematite NPs.

5.5 Conclusion

Therefore, in Chapter 5 uniform hematite NPs of various sizes and morphologies were crafted into thin films. When these hematite thin films are exposed to the transmission and reflection of light colours with wavelength from 465 nm to 810 nm are observed. These unique colours come from the aggregation of smaller hematite NPs into large assemblies. These hematite NPs can then be used to create different colours of pigments to decorate porcelain and paint.

5.6 References

[5.1]Aguirre, C. I.; Reguera, E.; Stein, A. *Adv. Funct. Mater.* **2010**, *20*, 2565–2578.

[5.2]Arsenault, A. C.; Míguez, H.; Kitaev, V.; Ozin, G. A.; Manners, I. *Adv. Mater.* **2003**, *15*, 503–507.

[5.3]Russell, F.; Bichowsky, V. *J. Am. Chem. Soc.* **1918**, *40*, 500–508.

[5.4]Von Freymann, G.; Kitaev, V.; Lotsch, B. V.; Ozin, G. A. *Chem. Soc. Rev.* **2013**, *42*, 2528–2554.

[5.5]Stein, A.; Wilson, B. E.; Rudisill, S. G. *Chem. Soc. Rev.* **2013**, *42*, 2763–2803.

[5.6]Rodrigues da Costa, A.; Sc, D.; Chapoulie, R.; Rud, F. Flávio Sandro Lays Cassino. *Metallurgy and Materials* **2011**, *64*, 187–191.

[5.7]Hashimoto, H.; Nakanishi, M.; Asaoka, H.; Maeda, T.; Kusano, Y.; Fujii, T.; Takada, J. *ACS Appl. Mater. Interfaces*. **2014**, *6*, 20282–20289.

[5.8]Schwertmann, U.; Cornell, R. M. *Iron Oxides in the Laboratory: Preparation and Characterization.* Second, Completely Revised and Extended ed.; Wiley-Vch: Weinheim, **2000**.

[5.9]Hashimoto, H.; Higuchi, K.; Inada, H.; Okazaki, Y.; Takaishi, T.; Asoh, H. *ACS Omega* **2016**, *1*, 9–13.

[5.10]Hashimoto, H.; Inada, H.; Okazaki, Y.; Takaishi, T.; Fujii, T.; Takada, J. *ACS Appl.Mater. Interfaces*. **2016**, *8*, 10918–10928.

Final Summary

This master thesis presents the synthesis and characterization of several different nanoscale systems useful for optical, catalytic and photoelectrochemical applications. The nanoscale systems investigated include AgDeNPs, IrO_{2-x} core shells, 1-D hematite NPs and hematite thin films.

In Chapter 2 the synthesis of uniform high-quality AgDeNPs, AgPRNPs and silver platelets was discussed. These AgDeNPs were synthesized with increasing sizes, with their LSPR peaks varying from 415 nm to 559 nm. The ability to synthesis AgDeNPs with the exact tunable LSPR peak maxima is significant because it allows to target specific desired systems when used in biological sensing applications.

In Chapter 3, the synthesis of uniform IrO_{2-x} core shells and their self-assembly into uniform thin films was discussed. These IrO_{2-x} core-shells redshift the LSPR of the AgDeNP core, from 471 nm to 541 nm proportionally to the amount of IrO_{2-x} deposited. The AgDeNPs can also be gold plated, which can then be encapsulated into IrO_{2-x}Au@AgDeNPs. The process for creating these IrO_{2-x} core shells was also investigated for iron and manganese oxides.[1.29]

In Chapter 4, uniform 3-D and 1-D hematite NPs were synthesized with controllable lengths via the use of additives, temperature and time. These 3-D hematite NPs are used as starting seeds to create the 1-D hematite NPs via seeded regrowth The 1-D hematite NPs are grown along C_3 axis of the rhombohedral hematite morphology, where the centre component, length and cap thickness can be changed depending on reaction parameters. Hematite is an indirect band-gap semiconductor and thus the main 1-D hematite NP needs modifications to be used in potential water-splitting applications. Therefore, future work to solve this limitation,

would involve doping the centre component of the hematite with iridium and the end hematite caps with platinum NPs.

In Chapter 5 colourful hematite thin films were created by using uniform hematite NPs of various sizes. The resulting hematite thin films produced a full spectrum of structural colours when observed via the transmission and reflection of light. The creation of hematite thin films from size-controlled hematite NPs is important because it shows that hematite NPs can be tuned to display a specific colour. This specificity is useful in the preparation of chemically stable colourful pigments that historically have been used to decorate pottery. Therefore, the ability to control the size of the hematite NPs enables the creation of hematite thin films that exhibit structural colour across the visible spectrum.